Study of Charges Present in Silicon Nitride Thin Films and Their Effect on Silicon Solar Cell Efficiencies

by

Vivek Sharma

A Dissertation Presented in Partial Fulfillment
of the Requirements for the Degree
Doctor of Philosophy

Approved August 2013 by the
Graduate Supervisory Committee:

Stuart Bowden, Chair
Dieter Schroder
Christiana Honsberg
Ronald Roedel
Terry Alford

ARIZONA STATE UNIVERSITY

December 2013

ABSTRACT

As crystalline silicon solar cells continue to get thinner, the recombination of carriers at the surfaces of the cell plays an ever-important role in controlling the cell efficiency. One tool to minimize surface recombination is field effect passivation from the charges present in the thin films applied on the cell surfaces.

The focus of this work is to understand the properties of charges present in the SiN_x films and then to develop a mechanism to manipulate the polarity of charges to either negative or positive based on the end-application. Specific silicon-nitrogen dangling bonds ($\cdot Si\equiv N$), known as K center defects, are the primary charge trapping defects present in the SiN_x films. A custom built corona charging tool was used to externally inject positive or negative charges in the SiN_x film. Detailed Capacitance-Voltage (C-V) measurements taken on corona charged SiN_x samples confirmed the presence of a net positive or negative charge density, as high as +/- 8 x 10^{12} cm^{-2}, present in the SiN_x film. High-energy (~ 4.9 eV) UV radiation was used to control and neutralize the charges in the SiN_x films. Electron-Spin-Resonance (ESR) technique was used to detect and quantify the density of neutral K^0 defects that are paramagnetically active. The density of the neutral K^0 defects increased after UV treatment and decreased after high temperature annealing and charging treatments. Etch-back C-V measurements on SiN_x films showed that the K centers are spread throughout the bulk of the SiN_x film and not just near the SiN_x-Si interface. It was also shown that the negative injected charges in the SiN_x film were stable and present even after 1 year under indoor room-temperature conditions.

Lastly, a stack of SiO_2/SiN_x dielectric layers applicable to standard commercial solar cells was developed using a low temperature (< 400 °C) PECVD process. Excellent surface passivation on FZ and CZ Si substrates for both n- and p-type samples was achieved by manipulating and controlling the charge in SiN_x films.

Dedicated to

my Grandparents,

and to Dr. Dieter Schroder

ACKNOWLEDGMENTS

"Life is pretty simple: You do some stuff. Most fails. Some works. You do more of what works. If it works big, others quickly copy it. Then you do something else. The trick is the doing something else" – Thomas J. Peters, Chicago Tribune, 1994

This quote by Tom Peters fits well with my experiences as I now look back over the past four years that I have spent at the Solar Power Lab as a PhD student. Working on multiple different projects, I have learnt that the key to success is to '*always keep doing something*'. There are many professors, colleagues, co-workers and friends who have selflessly helped me with my PhD work and have taught me many invaluable lessons of life, and therefore, I will be forever grateful to all of them.

First of all, I would like to thank Dr. Christiana Honsberg and Dr. Stuart Bowden for accepting me as PhD student under their supervision and for being the most amazing advisors that one can ever wish for. Dr. Bowden gave me absolute freedom to work on the projects of my own choice and made sure there were enough resources available to me to finish those projects. Over the years, I have considered Dr. Bowden more as a friend than an advisor and this cordial relation between us helped me sailing through my PhD easily. I have learnt hard work and persistence from Dr. Honsberg, whereas, Dr. Bowden taught me how to keep smiling even when things are not working your way. I will sorely miss knocking on their office doors without any prior appointment multiple times a day and I feel blessed to have them as my advisors.

I also feel extremely lucky to have spent few years under the supervision of Dr. Dieter Schroder. It was my first ever class at ASU that I took under Dr. Schroder. I was so influenced by his knowledge on solid-state electronics principles, his lucid and plain worded style of presentation that I changed my academic direction to solid-state physics instead of circuits dreaming to be his graduate student one day. My dream came true few years later when Dr. Schroder generously agreed to be my PhD co-advisor. I am thankful to Dr. Schroder to teach me how be humble and possess knowledge at the same time. Dr. Schroder enlightened me with his unfathomable knowledge on semi- conductor physics, MOS devices and specifically capacitance-voltage measurements. I will always regret the fact that he was not there when I finished my PhD.

I would also like to thank Dr. Ronald Roedel for accepting me as a PhD student initially under him and providing me the first exposure to solar cell physics. Many thanks to Dr. Terry Alford for agreeing to be on my PhD committee and advising on various material characterization techniques for silicon nitride films.

I am also deeply humbled and grateful to have worked with Bill Dauksher (Process Lab Manager) and Dr. Clarence Tracy (Senior Research Scientist) at Solar Power Lab over the past four years. I am thankful to Bill for being my teacher and guide for various cleanroom protocols and for all the knowledge and experience that I have gained in running and maintaining PECVD equipment, process optimization and critical thinking for solar cell processing. I would like to acknowledge the role and impact of Dr. Tracy on my PhD work. I am grateful to him for spending endless hours while discussing complex capacitance-voltage curves of silicon nitride on silicon, charge polarity and movement, band diagrams and many other solar cell related problems. I am sure I would never have understood them without Dr. Tracy's deep understanding and logical insight on the subject matter.

I am also happy to have spent some of the wonderful times with all my friends and colleagues at the Solar Power Lab. I am thankful to all of my fellow lab-mates who have helped me in countless number of experiments and for keeping the lab atmosphere so lively and jovial. I really enjoyed working together with my friends at SPL and wish them good luck for all their future endeavors.

I would also like to acknowledge the support and help from our administrative staff of Susan Edgington, Michele Nobles and Rebecca Davis. I am thankful to all of them for taking care of all the administrative work despite being overworked just to make sure that I can spend more time on my research.

I am also thankful to many other people who have always helped me with my experiments and characterization work, particularly, Barry O'Brien (Flexible Display Center, ASU), Diana Convey, Marco Flores and the entire staff at the LeRoy Eyring Center of Solid State Science (LE-CSSS) and at the Center for Solid State Electronics Research (CSSER) both at ASU.

Finally, I would like to thank all my friends, colleagues, acquaintances and my family members for all their support and understanding and for making these PhD years in the journey of my life so wonderful and enjoyable.

TABLE OF CONTENTS

Page

CHAPTER

CHAPTER Page

LIST OF TABLES

LIST OF FIGURES

Figure Page

Figure Page

Figure Page

Figure Page

Figure Page

Figure Page

Figure Page

Chapter 1

INTRODUCTION

1.1 Climate change

> "We did not inherit this world from our parents..
>
> we are borrowing it from our children"
>
> - Author unknown

Over the past decade, several scholarly articles and scientific research reports have been published bringing our attention to the evidences of global warming and warning us about the imminent climate change. Average global temperatures that are being measured currently are higher than anytime over the past 4000 year period [1] and the trend is believed to continue in the near to mid-term future. Another report recently published in Science magazine [2] states that the higher temperatures recorded in the past 100 years have been at unprecedented levels over the entire past Holocene. The authors of the report reconstructed global and local temperature anomalies for the past 11,300 years when recent ice age ended for northern hemisphere and noted that the global mean temperatures rose naturally till about 7550 to 3550 BC followed by a cooling trend, bringing down the global temperatures during 1450 to 1850 AD. However, since 1850 AD, the average global temperatures have increased at an unnatural and exponential rate leading to an average rise of 0.6 °C in recorded global temperatures. A study paper published by Hansen et al [3] reports of temperature anomalies recorded during the 30 year period from 1980 to 2010 and noticed that seasonal mean temperature anomalies have significantly increased in the past three decades. An example of these temperature anomalies is the recent extreme summer time temperatures recorded over parts of US, Europe and Russia. The author categorically states that such temperature anomalies are direct results of global warming. Fig. 1.1 shows how the temperature anomalies have increased since 1880 when temperature records were kept for the first time.

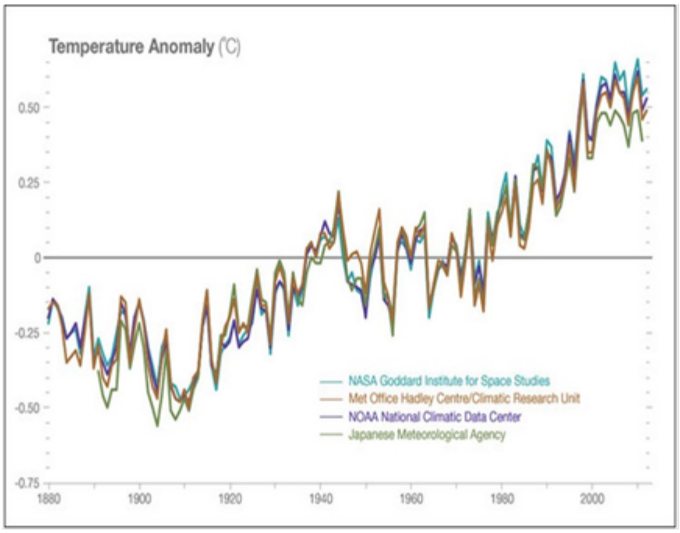

Fig. 1.1: Recorded temperature anomalies (1880-2012) [4]

Primarily, human activities are the major contributing factors leading to the climate change. Since the advent of industrial age, large amounts of greenhouse gases (GHGs) e.g. CO_2, CH_4, N_2O, chlorofluorocarbons (CFCs), SF_6 are continuously being released in the atmosphere due to burning of fossil fuels (coal, petroleum products) for transportation, electricity generation, industrial processes and other activities. The net effect of GHG is measured and reported in terms of equivalent amount of CO_2 and it is reported that since 1990, global early emissions have gone up by approximately 6 billion tons of CO_2 equivalent. As shown in Fig. 1.2, the current level of CO_2 is reported at 398 ppm, which is 35% higher than any previous CO_2 levels ever measured in the past 400,000 years. These GHGs trap the heat being reflected off the earth's surface and do not allow the heat to dissipate in the space, thereby, increasing the average global surface temperature (Fig. 1.1).

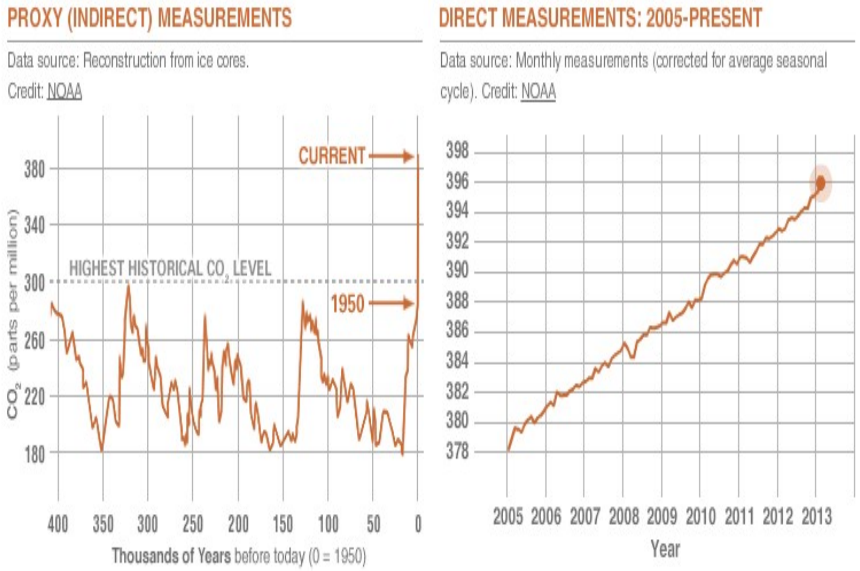

Fig. 1.2: Rise in CO_2 concentration over the years [4]

Rise in the average global temperature will have a significant negative impact on weather and water cycles leading to extreme events of prolonged droughts in some geographic locations and unusually heavy rainfalls and flooding in other locations. Scientists have already started noticing effects of global warming on polar ice mass. Increasing temperatures in northern latitudes have started melting large glaciers and snow particularly at Arctic and Greenland. Fig. 1.3 shows receding area of ice cover in the Arctic region from approximately 8 million square kilometers in 1980 to 3.61 million square kilometers in 2012, indicating a decrease of 55% in total ice cover area. This melting ice will lead to a significant rise in mean sea levels by up to 7-23 inches that will be catastrophic to many coastal cities around the world. Scientists also believe that climate change will also be responsible for stronger and much powerful hurricanes and storms. Certain species are feared to get extinct due to change in local climate leading to an irreversible impact on the food chain and natural ecosystem.

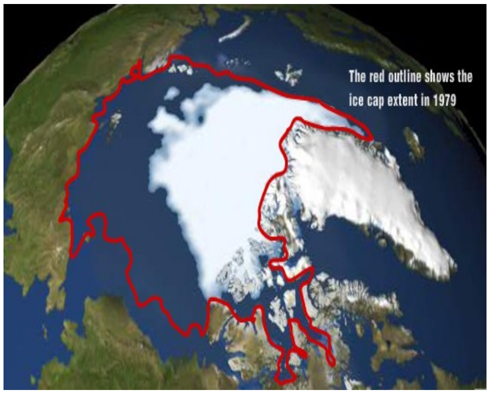

Fig. 1.3: Decreasing area of Arctic ice cover [4]

1.2 Role of renewable energy

To mitigate the impact of climate change, we need to act swiftly and collectively to cut down on our emission levels by setting up proper economic, social and political policy framework in place. A general set goal is to stabilize the GHG emissions to at 450-500 ppm of equivalent CO_2 to avoid catastrophic effects on our ecosystem and this requires reduction in the current emission levels by approximately 50-85% by the year 2050 [5]. Excessive use of fossil fuels (coal, diesel, natural gas) for energy generation has already added significant levels CO_2 in the atmosphere and reducing the emissions will require more renewable energy based power plants in place to generate clean, emission free electricity. Government policies, subsidies, favorable market conditions, declining prices for renewable energy systems (e.g. solar modules), technology improvement and general public awareness will increase the overall percentage of renewable energy sources in the total energy generation market. The cumulative global installed capacity for renewable energy sources has increased by 72% from 748 GW to 1285 GW during

2000 – 2011 [6]. Renewable energy accounted for 22% of all global electricity generation at 4309 TWh (Fig. 1.4) and out of all renewable energy resources, wind and solar were the fastest growing energy generation technologies. While wind generation grew by a factor of 13, solar PV generation grew by a factor of more than 51 between 2000 and 2011. Similarly, the US has installed 146 GW of renewable energy capacity during 2000-2011 at a compounded annual growth rate (CAGR) of 4.2%. However, solar generation, both flat plate PV and concentrated solar power (CSP) still represent a very small fraction in overall electricity generation. In 2011, the net electricity generated in the US from all the sources was 411.7 million kWh, out of which, renewables (biomass, hydro, wind, solar) accounted for 12.8% at 526 million kWh and solar represented just 0.2% of the total generation at 1.05 million kWh (Fig. 1.5).

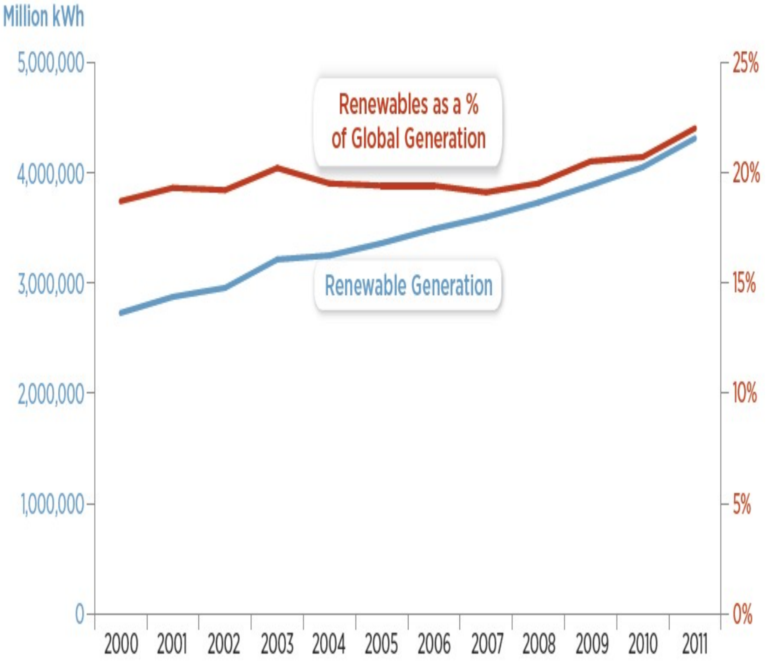

Fig. 1.4: World renewable electricity generation [6]

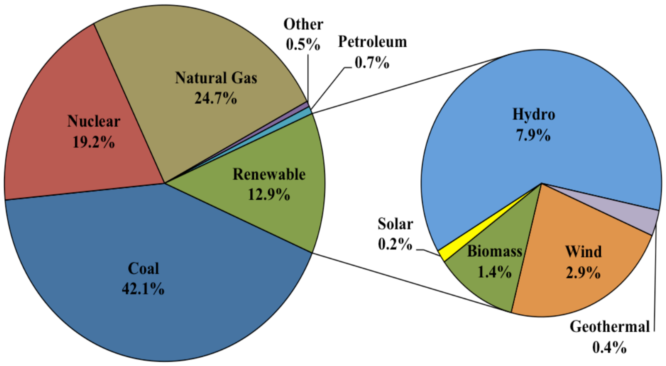

Fig. 1.5: US total electricity generation in 2011 [6]

The US photovoltaic (PV) market installed 742 MW of new PV systems (crystalline silicon (c-Si) technology systems only) in the 2nd quarter of 2012, thereby, posting a strong 116 % rise in installed PV capacity compared to the same quarter in 2011 [7]. It is predicted that by the end of 2012, 3.2 GW of new PV installations will be added to the current capacity of 5.2 GW, up by 71% from 2011 [7]. The key driver to the continued growth is drastic reduction in PV installed system prices over the past 1 year. Year on year average installed prices have decreased by 33% to the current price of \$3.5/W. The key driver behind reduced system costs is the oversupply of cheap PV modules currently available at \$0.87/W, a 44% drop in prices over the past year [7, 8] (Fig. 1.6). This continued reduction in PV system costs is the driving force behind the steep increase in PV installations. Despite of reduced profit margins and saturation of some key market sectors, the growth in PV installations is predicted to increase in near future (Fig. 1.7). It is expected that the PV market will slow down a little from the current explosive growth but will continue to increase at a modest rate of 25-30% per year.

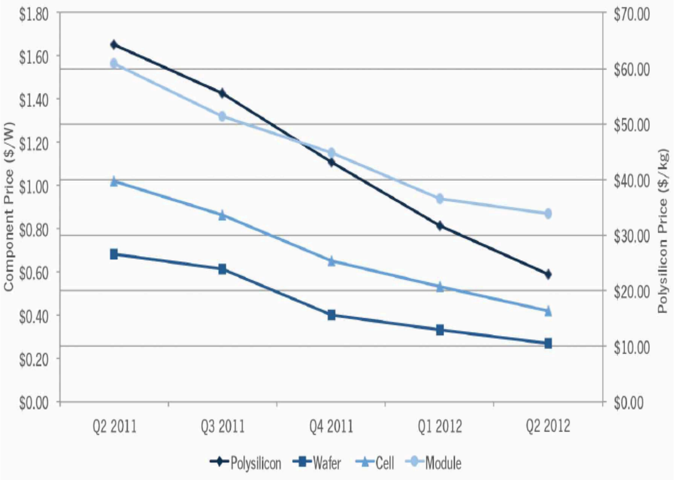

Fig. 1.6: PV component price trend [7]

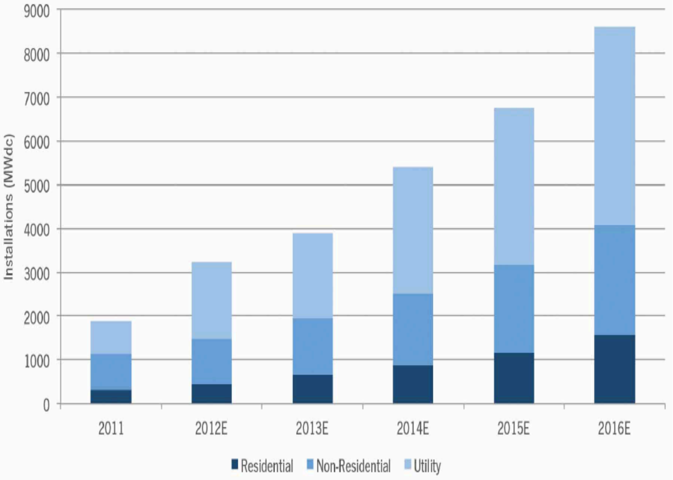

Fig. 1.7: US solar market outlook 2012-2016 [7]

Crystalline silicon (c-Si) solar cells (mono and multi-crystalline) continue to dominate the PV technology market with a market share of 85% [9]. The current conversion efficiencies of c-Si cells are approaching 20% [10] and that of modules is about 16% [11]. Although, the thin film technology (e.g. CdTe) continue to make progress in cell efficiencies (~ 13%), their market share however, still has to gain a lot of ground (Fig. 1.8).

1.3 Crystalline silicon solar cells

Most of the industry standard c-Si solar cells are of dimensions ~ 15.6 cm x 15.6 cm and approximately 180 μm thick, consisting of n^+ emitter on a p-doped base. The base region (180 μm) is boron-doped p-type (1-5 Ω.cm) and the emitter (~ 1 μm) is heavily doped n-type (50-150 Ω/☐) silicon. When photons of energy greater than the band- gap (E_G) of silicon (1.12 eV) enter through the top emitter region, they create electron and hole pairs throughout the silicon material depending on their energy. The light generated carriers thus created diffuse towards the p-n junction, get swept across due to built in electric field to become majority carriers and get collected by the external circuit (Fig. 1.9).

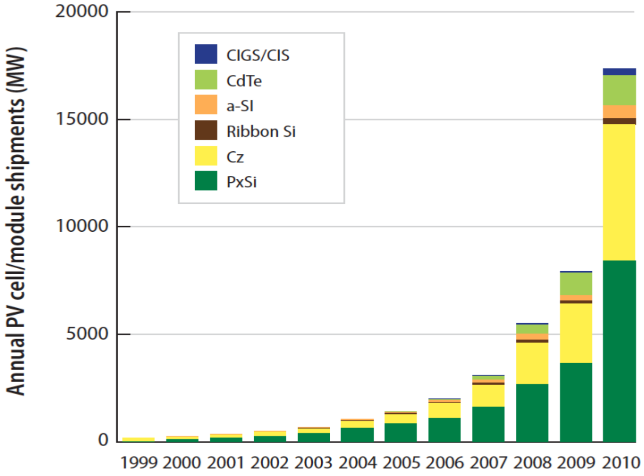

Fig. 1.8: Global annual PV cell and module shipments by PV technology [9]

Over the years, screen printed p-type silicon solar cells with heavily doped n^+ emitter have been manufactured with an average efficiency of approximately 16-17 % [13 - 15] (Fig. 1.10). Laboratory cells have been able to achieve record efficiencies up to 25% [16] using some advanced concepts (photolithography, laser ablation, selective emitter, local rear diffusions etc.). However, these advanced processing steps are generally cost extensive and sometime show limited gain in efficiency. The industry tends to slowly adapt to these advanced technological processes once they become cost effective and reliable.

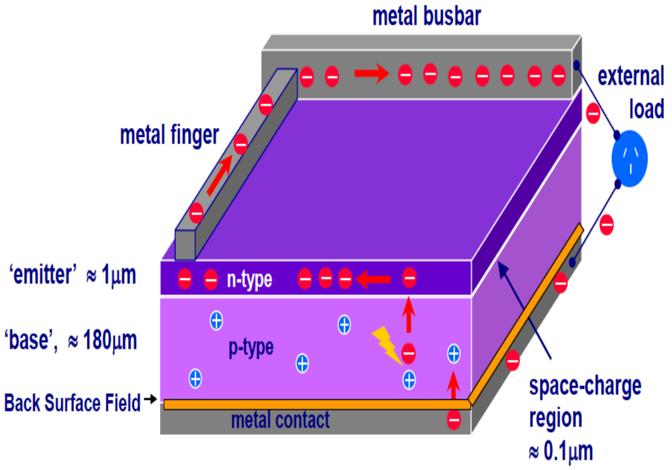

Fig. 1.9: Schematic of silicon solar cell [12]

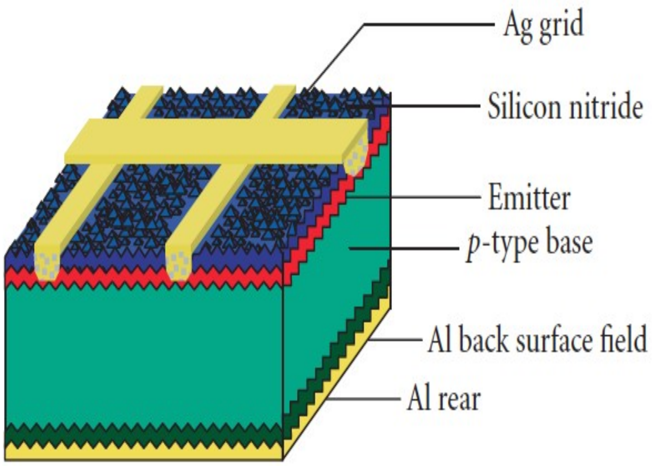

Fig. 1.10: Industrial p-type c-Si cell [15]

The SEMI International Technology Roadmap for Photovoltaics (ITRPV) report released in 2012 [17] predicts an overall picture of the emerging new technologies and trends in c-Si industry to achieve higher cell efficiencies from the current levels. The ITRPV report predicts that:

- The silicon wafer thickness will continue to reduce from the current 180 μm to 120 μm by the year 2020. As the wafer thickness reduces, passivation of cell surfaces will become a critical step to further enhance cell efficiencies.
- Migration to lightly doped emitters (from 80 Ω/☐ to 160 Ω/☐) to improve the blue response in the cell. In this case, the fixed charges present in the passivating film can easily change the surface conditions for lightly doped emitters.
- N-type wafers with p^+ emitters - the industry is currently looking forward to n-type wafers as they are free from presence of light induced efficiency degradation compared to p-type wafers originating from Boron-Oxygen complexes. It is predicted that by the year 2020, n-type wafers will occupy 65% of the mono silicon market segment.

1.4 Motivation for this work

The aim of this work is to understand the charges present in the hydrogenated amorphous silicon nitride (SiN_x) anti-reflection films and to study their effect on the passivation of c-Si solar cells. It is well known that the SiN_x film when applied on the n^+ emitter surfaces of p-type cells, the positive fixed charges present in the film decrease the surface recombination through field effect passivation by creating an accumulation layer in the heavily doped n-type emitter. These same positive charges can create a depletion or an inversion region when applied to p-type doped surfaces of the cells based on the doping concentration. For the case of p-doped surfaces, these positive charges try to create an inversion region of minority electrons, whereas, the p-type doping reduces the minority carrier concentration. As the emitter doping increases, the effect of positive dielectric charges in creating an inversion layer decreases further. Eventually, instead of an inversion layer, a depletion region is created at the surface that leads to a higher surface recombination due to presence of both type of carriers. Further for p-doped regions, the presence of an inversion layer adjacent to metal contact regions (such as rear p-type surfaces of n^+-p cell) will cause parasitic shunting thereby, degrading the cell performance. Hydrogenated aluminum oxide (Al_2O_3) films are being extensively studied and used lately as an alternative to SiN_x films as a passivation layer for p^+ emitters on n-type cells or for rear surfaces of p-type cells as the negative fixed charges present in the Al_2O_3 film create a hole accumulation layer for the p-type surfaces. However, processes and tools needed to deposit Al_2O_3 films on a high volume industrial scale are not available yet, making it difficult to find a solution for films carrying negative charges to be applied on p-type surfaces. This work utilizes an important property of the defects present in the SiN_x films that allows the films to carry either positive or negative charges. This primary charge trapping defect of the SiN_x film, known as K^o center, allows the net charge of the film to be easily manipulated and inverted from positive to negative, thereby, making the SiN_x films useful for passivating both p or n-type surfaces. It is therefore, required to understand the origin of charges present in SiN_x films and to further investigate their electrical and material properties for solar cell applications. It is important to look at the bigger picture where, SiN_x films consisting of varying magnitude of either positive or negative charge can be used to passivate either type of p- or n-doped Si substrates with varying doping concentrations. The current surface passivation techniques will need to be optimized for future cell architectures like lightly doped emitters, thinner substrates and n-type cells with p-type emitters where the magnitude and polarity of charges will control the cell efficiency. Cell surfaces will play a larger role for these future cell designs and therefore will require charge assisted surface passivation techniques. In this work, standard SiN_x films deposited using Plasma Enhance Chemical Vapor Deposition (PECVD) tool are characterized using various electrical, material and optical characterization techniques. Capacitance-voltage (C-V) measurement were used quantify the amount and polarity of charge present in the films. Various experiments have been carried out on test structures where different polarity of charges were injected in the SiN_x films using a corona discharge tool and the basic charge properties were determined and analyzed. Electron Spin Resonance (ESR) measurements were used to detect and understand the properties of primary charge trapping center present in the SiN_x films (K^o defect). Location of charges in the SiN_x film, effect of corona charging on film properties and long term stability of charges have been described to further enhance the knowledge on the charges present in the SiN_x films. The effect of externally injected charges in the SiN_x films on minority carrier lifetime of standard, solar grade, p- or n-doped CZ silicon substrates has also been studied in this work.

Chapter 2

RECOMBINATION AND SURFACE PASSIVATION

2.1 Recombination basics

Excess electron hole pairs that are generated in the semiconductor due to external excitation (such as incident light) cease to exist due to recombination processes. These recombination processes take place both n the bulk and at the surfaces of the semiconductor substrate and the useful light generated excess electron-hole pairs can be lost due to recombination processes before being collected by the external circuit. During recombination the excited electrons present in the conduction band fall back to the valence band and recombine with the hole and the excess carrier concentration in the semiconductor eventually reaches its stable equilibrium level. Due to increased re-combination, the light generated current (J_{SC}) drops and so does open circuit voltage (V_{OC}) as given by Eq. 2.1. Higher rate of recombination increases the magnitude of saturation current (J_o) by several orders and thus, reduces the overall cell efficiency through the following Eq. 2.2:

$$V_{OC} = \frac{kT}{q} \ln(\frac{J_{SC}}{J_o} + 1) \qquad 2.1$$

$$Efficiency\,(\eta) = \frac{J_{SC}.V_{OC}.FF}{Power_{IN}} \qquad 2.2$$

The recombination lifetime τ can be defined as the average time for which the light generated carriers survive before recombining. It is a function of excess carrier density Δn and net recombination rate U given by Eq. 2.3.

$$\tau = \frac{\Delta n}{U} \qquad 2.3$$

A higher lifetime of minority carriers will relate to a higher probability of light generated carriers to contribute to J_{SC} and therefore would lead to higher efficiency. The net recombination rate in turn depends on different recombination process occurring in the bulk of the semiconductor and also at the surfaces.

The recombination mechanisms [18] occurring in the wafer are:

- Shockley Read Hall (SRH) recombination via defects in the band gap
- Radiative recombination, and
- Auger recombination
- Surface recombination – a manifestation of SRH recombination

SRH recombination: During SRH recombination, the electron hole pairs recombine through defects or impurity traps present in the band-gap of the semiconductor through a two-step process (Fig. 2.1 - a). The energy released following the SRH recombination is in the form of lattice vibrations or phonons. The SRH recombination is therefore, dependent upon the density of traps (N_T), their energy levels (E_T) within the band-gap, the capture cross-sections of electrons (σ_n) and holes (σ_p). The SRH recombination rate U_{SRH} is given by Eq. 2.4.

$$U_{SRH} = \frac{np - n_i^2}{\tau_p(n + n_1) + \tau_n(p + p_1)} \qquad 2.4$$

where, $n = n_o + \Delta n$ and $p = p_o + \Delta p$ (n_o, p_o are the equilibrium carrier concentration and Δn, Δp are the excess carrier concentration), τ_p and τ_n are the capture time constants given by Eq. 2.5 and n_1, p_1 are the trap electron and hole concentrations given by Eq. 2.6

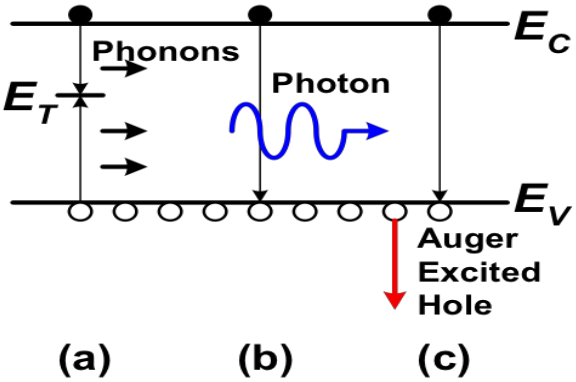

Fig. 2.1: Recombination mechanisms in semiconductors [19]

$$\tau_p = \frac{1}{\sigma_p N_T v_{th}} \quad and \quad \tau_n = \frac{1}{\sigma_n N_T v_{th}} \qquad 2.5$$

$$n_1 = n_i \exp(\frac{E_T - E_i}{kT}) \quad and \quad p_1 = n_i \exp(-\frac{E_T - E_i}{kT}) \qquad 2.6$$

Therefore, using the relation between lifetime τ and recombination rate U given in Eq. 2.3, the SRH lifetime is given as:

$$\tau_{SRH} = \frac{\tau_p(n+n_1)+\tau_n(p+p_1)}{(p_0+n_0+\Delta n)} \qquad 2.7$$

Radiative recombination: During this recombination process, band to band recombination of the electron hole pairs takes place releasing the excess energy in form of photons (Fig. 2.1 - b). Radiative recombination processes directly opposite of generation process taking place during light excitation and during recombination, excess electrons from the conduction band fall to the valence band and recombine with holes. The radiative lifetime τ_{rad} is given as:

$$\tau_{rad} = \frac{1}{B(p_o + n_o + \Delta n)} \qquad 2.8$$

where, B is the radiative recombination coefficient. For silicon, B = 4.73 x 10^{-15} cm^3/s at 300 K. The radiative recombination process is more pronounced in direct band-gap semiconductors like GaAs and in case of silicon the radiative recombination rate is extremely small for silicon being an indirect band-gap semiconductor.

Auger recombination: In case of Auger recombination, the excess energy released following the recombination of electron hole pairs is in turn absorbed by a third carrier that is either an electron or a hole (Fig. 2.1 -c) making this recombination mechanism a three particle process. The Auger lifetime is given as:

$$\tau_{Auger} = \frac{1}{C_p(p_o^2 + 2p_o\Delta n + \Delta n^2) + C_n(n_o^2 + 2n_o\Delta n + \Delta n^2)} \qquad 2.9$$

where, C_p = Auger recombination coefficient for holes = 1 x 10^{-31} cm^6/s and C_n = Auger recombination coefficient for electrons = 2.8 x 10^{-31} cm^6/s. It can be seen from the Eq. 2.9 that the Auger lifetime has an inverse dependence on n^2. This implies that for heavily doped substrates or under high injection conditions, Auger lifetime will be the limiting factor.

Surface recombination: The surfaces are abrupt terminations of the crystal lattice and consist of broken dangling bonds that act as active recombination sites. These defects at the surface are distributed throughout the band-gap and therefore, the recombination due to defects at the surfaces act as a manifestation of SRH recombination occurring in the bulk. The surface recombination rate U_S is given by Eq. 2.10:

$$U_S = \int_{E_V}^{E_C} \frac{(n_s p_s - n_i^2) v_{th} D_{it}(E_T)}{\frac{(n_s + n_1)}{\sigma_p(E_T)} + \frac{(p_s + p_1)}{\sigma_n(E_T)}} dE_T \qquad 2.10$$

where, D_{it} is the interface defect density as a function of trap energy E_T. n_S, p_S are the electron and hole concentration at the surface respectively and n_i is the intrinsic carrier concentration (for Si, ni = 1 x 10^{10} cm^{-3} at 300 K) [20]. Assuming the surface recombination velocity (SRV) can be defined as the velocity with which the minority carriers rush towards the surfaces and recombine due to surface defects. The surface recombination velocity S is given by:

$$S = \frac{U_S}{\Delta n_s} \qquad 2.11$$

where, U_S is the surface recombination rate and Δn_S is the excess carrier density at the surface. When electrical charges (Q_f) are present on the wafer surface due to oxidation or application of an insulating film, the energy bands bend at the surface (accumulation, inversion or depletion). The electrical field due to the band bending strongly effects the surface concentrations of electrons and holes, also known as field effect passivation. Therefore, at the surface, $\Delta n_s \neq \Delta p_s$ and the effective surface recombination velocity S_{eff} is given by Eq. 2.12:

$$S_{eff} = \frac{U}{\Delta n(x = d)} \tag{2.12}$$

where, x = d denotes a virtual surface at the edge of the space charge region in the wafer. Therefore, a well-passivated surface means low surface defects and low SRVs. The surface recombination velocity strongly depends on the injection level at the surface (Δn_S), fixed charge density (Q_f) present in an insulating film on the surface, substrate doping concentration (N_A or N_D), defect energy levels and on the defect capture cross sections for electrons and holes [20].

The effective carrier lifetime τ_{eff} is inversely proportional to the net effective recombination rate. A particular recombination process may dominate over other recombination processes and limit the effective lifetime. For example, lifetime in multi-crystalline silicon is limited by SRH recombination due to presence of large number for defects due to grain boundaries. Similarly, for heavily doped regions such as emitters, Auger recombination is dominating. The effective lifetime τ_{eff} dependent upon all the recombination mechanisms, is given by Eq. 2.13:

$$\frac{1}{\tau_{eff}} = \frac{1}{\tau_{SRH}} + \frac{1}{\tau_{rad}} + \frac{1}{\tau_{Auger}} + \frac{1}{\tau_{Surface}} + \frac{1}{\tau_{emitter}} \tag{2.13}$$

2.2 Surface passivation techniques

Surface passivation techniques typically combine the following two concepts:

- Reduction in the surface state densities (D_{it}) - Chemical Passivation
- Reduction in the electron or hole concentration at the surface - Field Effect Passivation

2.2.1 Chemical passivation

The defect states at the surface or interface (D_{it}) can be reduced either by thermal oxidation at very high temperature (900 - 1100°C) or by hydrogen passivation of dangling bonds. The thermal oxidation technique gives very low surface state densities of 10^9 cm^{-2} eV^{-1} and S_{eff} of less than 10 cm/s for high resistivity (> 100 Ω.cm) p- or n-type wafers. However, requirement of extremely high temperatures for oxidation are detrimental to solar cell parameters. Another common way to reduce the surface state density is to grow thin hydrogenated films (SiN_x, a-Si, Al_2O_3) films at low temperatures (~400 °C) by various Chemical Vapor Deposition (CVD) methods. The hydrogen present in these films is released during annealing step and passivates the dangling bonds at the surfaces, thereby, reducing the interface state density D_{it}.

2.2.2 Field effect passivation

To minimize surface recombination, an internal electric field just below the cell surface is created by either a high-low junction or by depositing a charge carrying film to reduce the concentration of either type of charge carrier at the surface. As previously explained by Eq. 2.10, both type of carriers n_S and p_S are required for surface recombination to take place. Creating an internal electric field below the surface reduces the concentration of one type of carrier, thereby, effectively reducing the surface recombination. Generally, two techniques are employed for this purpose:

- Diffusion process: Either creating a p-n junction or a high-low junction ($p^+ p$ or $n^+ n$)
- Deposition of an insulating film (SiN_x, SiO_2, Al_2O_3) that is able to create field effect passivation due to large positive or negative fixed charges contained in the film.

A high temperature diffusion process creates a p-n junction or a high-low junction ($p^+ p$ or $n^+ n$ if the doping profile polarity is same as the bulk polarity). As the doping concentration in a p-n junction increases towards the surface, the resulting electric field effectively keeps the minority carriers away from the surfaces and pushes them towards the junction. Similarly, a high low junction known as back surface field (BSF) is widely used in p-type c-Si wafers (p^+p region created by Aluminum or Boron diffusion) to keep minority electrons away from the rear surface of the cell. The deposition of an insulating film on top also provides excellent field effect passivation due to the fixed charges Q_f in the film. SiO_2 as well as SiN_x films carry positive fixed charges while on the other hand; Al_2O_3 films carry negative fixed charges. These films effectively shield minority carriers (holes or electrons) from the surfaces and minimize surface recombination through field effect passivation [21].

To further illustrate the role of charge in controlling the surface recombination, band diagrams are shown in Fig. 2.2, for a p-type Silicon substrate deposited with a film containing negative or positive charges. As seen in Fig. 2.2 (a), presence of large negative charge ($\sim -1 \times 10^{13}$ cm^{-2}) on the p-type Si causes the bands at the surface to bend upwards creating an accumulation layer of holes. In this case, the minority electrons are expelled away from the surfaces. Left with just one type of carrier at the surface (p_S in this case) drastically reduces the surface recombination. Similarly, when large positive charge ($\sim +1 \times 10^{13}$ cm^{-2}) is present at the p-type Silicon surface, the bands now are pulled downwards and the surface is inverted (Fig. 2.2 (b)) with a large number of minority electrons (n_S). The majority holes are pushed away from the front surface and therefore, do not participate in the surface recombination process. On the other hand, if an intermediate amount of negative charge ($\sim -5 \times 10^{11}$ cm^{-2}) is now present in the film, it creates a depletion region under the surface (Fig. 2.2 (c)). The small magnitude of charge is unable to create a strong inversion layer of electrons and now both types of carriers (electrons and holes) can interact with surface defects D_{it}. This depletion region created by small magnitude to charge, therefore, increases the surface recombination. To reiterate, in order to minimize surface recombination through field effect passsivation, it is required to apply correct polarity and amount of charge to create a strong accumulation or inversion layer underneath the surface.

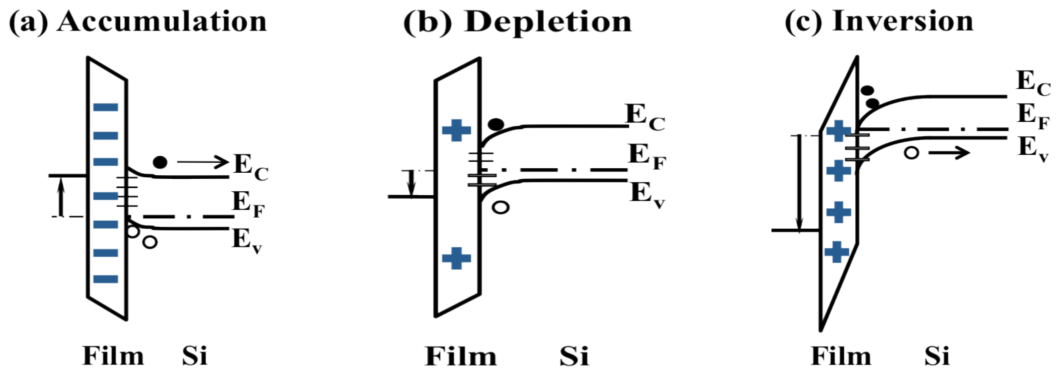

Fig. 2.2: Band diagram illustrating (a) accumulation, (b) depletion and (c) inversion of p-type silicon due fixed charge in dielectric film

2.3 PC1D simulation for effect of charge on cell efficiency

To further understand the effect of magnitude and polarity of charge on cell efficiency, a typical industry standard solar cell was modeled using PC1D software [22]. The cell parameters selected for the simulation are listed in Table 2.1. Other material properties relevant for silicon e.g. carrier mobilities, intrinsic concentration, band gap, refractive index were selected from default PC1D files.

For this purpose, varying magnitude of charge was applied to both the front and rear of a standard n^+-p cell. Positive as well as negative charge was applied to the front n^+ surface with three different emitter doping profiles to illustrate the effect of charge with emitter doping concentration on cell efficiencies. Negative charge was applied to the rear p-type base surface of the cell to simulate the effect of negative charge to minimize surface recombination in the absence of a back surface field.

TABLE 2.1: Cell parameters for PC1D simulation

Parameter	Value
Thickness	180 μm
Cell area	1 cm^2
p-type base doping	Boron, 5 x 10^{15} cm^{-3}
Bulk lifetime	500 μs
Front and rear surface recombination velocity	1 x 10^4 cm/s
Front surface	Textured
Spectrum	AM 1.5 G
Cell temperature	25 °C
Light intensity	0.1 W/cm^2
Front n^+ emitter doping	1 x 10^{18} to 1 x 10^{20} cm^{-3}
Front positive charge	+1 x 10^{10} to 1 x 10^{13} cm^{-2}
Front negative charge	-1 x 10^{10} to -1 x 10^{13} cm^{-2}
Rear negative charge	-1 x 10^{10} to -1 x 10^{13} cm^{-2}

2.3.1 Effect of positive charge applied at the front n^+ emitter surface

Fig. 2.3 shows the PC1D device schematic used for simulating the effect of positive charge on front n^+ emitter surface and Fig. 2.4 shows the effect of varying amount of positive charge from 1 x 10^{10} cm^{-2} to 1 x 10^{13} cm^{-2} applied on three different emitter doping profiles.

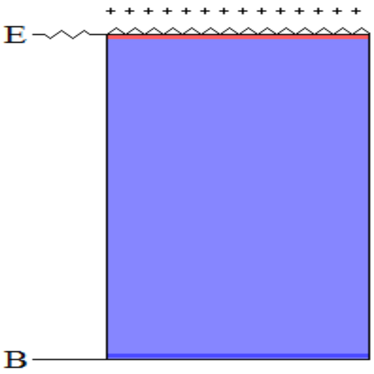

Fig. 2.3: PC1D device schematic - positive charge applied at the front n+ emitter surface

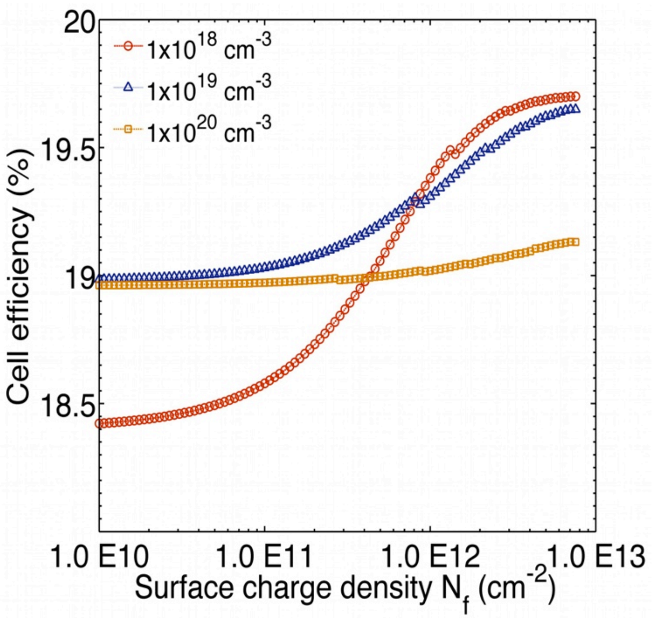

Fig. 2.4: PC1D simulation showing the effect of positive charge applied on front n+ surfaces on cell efficiency for different emitter doping (N_D) levels

It can be seen that increasing magnitude of positive charge applied on an n+ emitter increases the cell efficiency. It is also interesting to note that the lightly doped emitter (1 x 10^{18} cm^{-3}) shows the highest gain in cell efficiency from 18.4% to 19.7% for increasing positive charge. On the other hand, heavily doped emitter (1 x 10^{20} cm^{-3}) shows a marginal gain in cell efficiency from 18.9% to 19.2%. This difference can be attributed to the fact that for a lightly doped emitter, the concentration of minority carriers (holes in this case) is greater at the surface compared to a heavily doped emitter as per the relation given in Eqs. 2.14 and 2.15.

$$n \approx N_D \qquad 2.14$$

$$p \approx \frac{n_i^2}{N_D} \qquad 2.15$$

A lower amount of positive charge (1×10^{10} cm^{-2}) on a lightly doped emitter is not sufficient to keep the minority holes away from the surfaces. Progressively increasing the amount of charge to 1×10^{13} cm^{-2} effectively bends the surfaces in accumulation (Fig. 2.5) thereby, minimizing the surface recombination and increasing the cell efficiency. Moreover, for heavily doped emitters, Auger recombination further limits the cell efficiency. However, for future cell architectures with lightly doped emitters (~1×10^{19} cm^{-3}, 80-160 Ω/□), the cell efficiencies can increase from 18.9% to 19.6% by increasing the magnitude of applied positive charge.

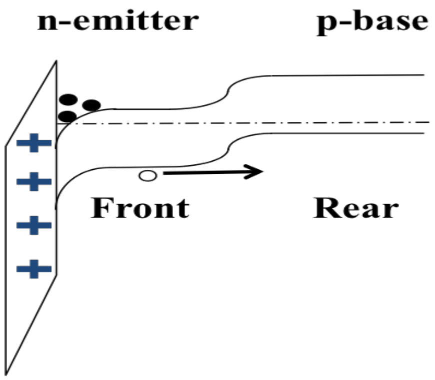

Fig. 2.5: Band-diagram showing the effect of positive charge applied on front n$^+$ surface of a cell

2.3.2 Effect of negative charge applied at the front n⁺ emitter surface

When negative charge in increasing magnitude from -1 x 10^{10} cm^{-2} to -1 x 10^{13} cm^{-2} was applied to the front n⁺ emitter surface, cell efficiencies drastically dropped as seen in Fig. 2.6. PC1D software, being a 1 dimensional solver, faced some convergence issues during part of this simulation run; however, the drop in cell efficiencies can be understood from the band diagram shown in Fig. 2.7. In this case, when negative charge is applied to the n⁺ emitter surface at the front, the bands bend up giving rise to depletion condition underneath the surface, allowing the minority carrier holes to reach the surface and participate in surface recombination through interface defects. While the surface of lightly doped emitter (1 x 10^{18} cm^{-3}) can easily be depleted with intermediate amount of charge (-1 x 10^{11} cm^{-2}), approximately -1 x 10^{12} cm^{-2} charge is required to deplete the surfaces of a heavily doped emitter (1 x 10^{20} cm^{-3}).

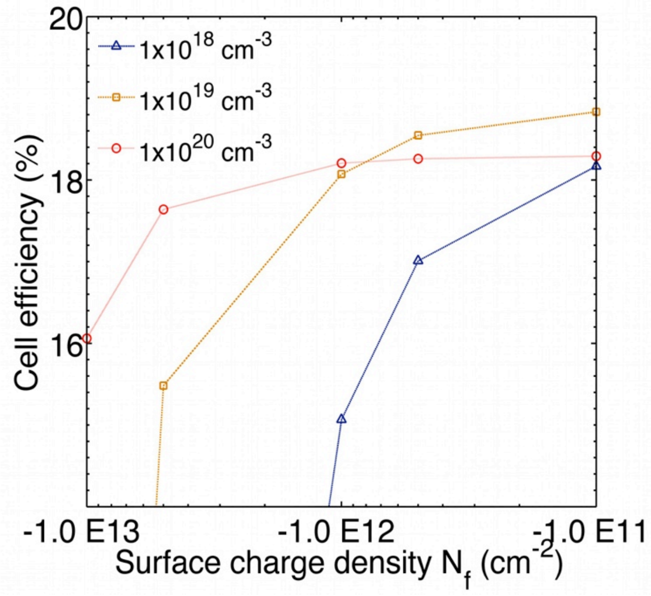

Fig. 2.6: PC1D simulation showing the effect of negative charge applied on front n⁺ surfaces on cell efficiency for different emitter doping (N_D) levels

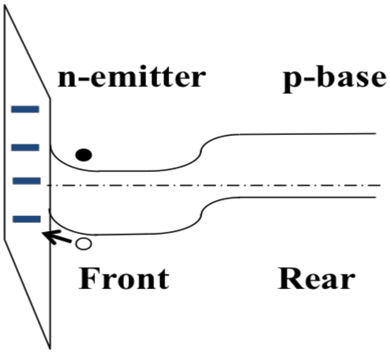

Fig. 2.7: Band-diagram showing the effect of negative charge applied on front n^+ surface of a cell

2.3.3 Effect of negative charge applied at the rear p-type base surface

As the last simulation run, when negative charge was applied to the rear p-type surface of the cell (Fig. 2.8), the cell efficiency increased with increasing magnitude of negative charge.

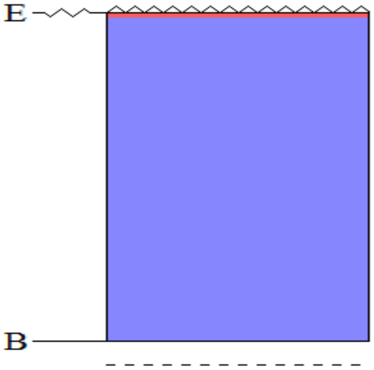

Fig. 2.8: PC1D device schematic - negative charge applied at the rear p-type base surface

With no back surface field (BSF) present and a high rear SRV at 1 x 10^4 cm/s, the rear surface of the cell became a major active recombination site. With no rear surface charge applied, the rear surface recombination was the limiting factor for cell performance and the simulated cell efficiency was only 16% (Fig. 2.9).

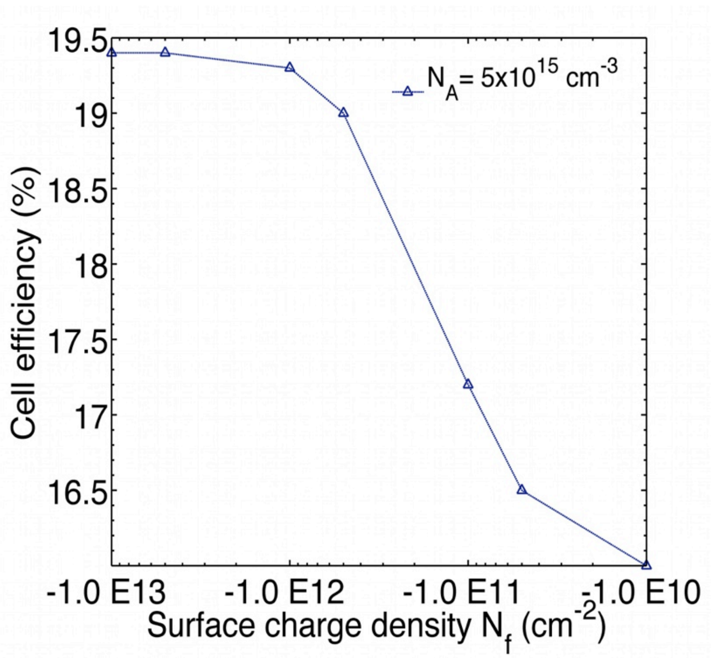

Fig. 2.9: PC1D simulation showing the effect of negative charge applied on rear p-type base (N_A = 5 x 10^{15} cm^{-3}) surface on cell efficiency

As shown by the band diagram in Fig. 2.10, increasing the amount of negative charge from -1 x 10^{10} cm^{-2} to -1 x 10^{13} cm^{-2} at the rear p-type surface of the cell effectively creates an accumulation layer of majority holes at the surface. This accumulation layer keeps the minority electrons away, thereby, reducing the surface recombination and increasing the cell efficiency from 16% for -1 x 10^{10} cm^{-2} charge to 19.6% for -1 x 10^{13} cm^{-2} charge. Similar effects were seen for n-type cells with p^+ emitters.

Therefore, it can be concluded that the correct amount as well as polarity of charge is required to achieve higher cell efficiencies. Specifically, charge assisted field effect passivation will be the key to enhance cell efficiencies for lightly doped emitters and thinner cells. Fig. 2.11 shows the band-diagram for an n^+-p cell with correct polarity of charge applied at the front and rear surfaces that minimizes surface recombination and improves cell efficiency.

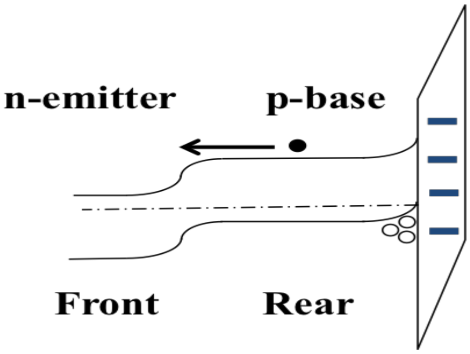

Fig. 2.10: Band-diagram showing the effect of negative charge applied on rear p-type base surface of a cell

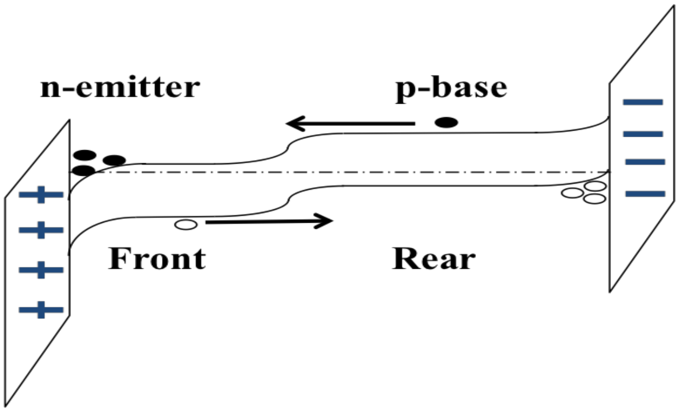

Fig. 2.11: Band-diagram of an n^+-p cell with correct polarity of front and rear surface charges

Chapter 3

FIELD EFFECT PASSIVATION USING DIELECTRIC FILMS

3.1 Aluminum oxide (Al_2O_3) film with fixed negative charges

As the PV industry is replacing full back Al BSF with rear passivation schemes, dielectric films are being applied to the rear of the solar cells to reduce the rear surface recombination in absence of an Al-BSF, to increase the rear internal reflection and to reduce the wafer bow for thinner substrates (~ 180 μm or less) [23-29]. Silicon nitride films (SiN_x), traditionally used as a front passivating film on n^+ emitter surfaces, can not be used at the rear p-type surface due to presence of fixed positive charges in it. These fixed positive charges induce inversion region underneath the surface that leads to parasitic shunting [30] and subsequent drop in cell efficiencies (Fig.2.6). Al_2O_3 films, on the other hand, carry negative fixed charge (Q_f = -3 x 10^{12} cm^{-2}) [31] and therefore, have emerged as a viable solution for passivating rear p-type surfaces or front p^+ emitter surfaces of n-type cells.

Hezel and Jaegar [31] first reported the role of Al_2O_3 films for surface passivation in 1989, where they reported a negative fixed charge of -3 x 10^{12} cm^{-2} in the Al_2O_3 films. However, over the next few years, the PV industry did not pay attention to the excellent surface passivation properties of Al_2O_3 films until 2006 when Agostinelli [32] reported S_{eff} < 50 cm/s on 2 Ω.cm p-type Si deposited with Al_2O_3 film. Over the next few years, several results reported excellent passivation (S_{eff} < 10 cm/s on both p-type and n-type CZ Si) achieved by thin (~ 10 nm) Al_2O_3 films carrying negative fixed charge deposited using Atomic Layer Deposition (ALD) technique [33-40]. Fig. 3.1 shows how S_{eff} varies as a function of corona charge density injected into both SiN_x and Al_2O_3 films [41]. Under flat-band conditions, the surface recombination velocity is large due to availability of both types of carriers. Also, under flat-band condition, injected corona charge (Q_c) is equal and opposite in magnitude to fixed charge (Q_f) in the dielectric films. Therefore, as seen in the Fig. 3.1, while SiN_x film contains approximately +2 x 10^{12} of fixed positive charges per cm^{-2}, Al_2O_3 film carries -1.3 x 10^{13} fixed negative charges per cm^{-2}. These negative fixed charges present in the Al_2O_3 film create a strong accumulation layer at the rear p-type surface of the solar cell and minimize rear surface recombination. As a result, excellent cell efficiencies greater than 20% have been reported where Al_2O_3 films are applied as a rear surface passivating dielectric film to passivated emitter and rear cell (PERC) p-type c-Si solar cells, as well as, a front passivating film for p^+ emitters on n-type cells [42 - 47]. Excellent review articles on properties, prospects and application of Al_2O_3 films have recently been written by Schmidt [48], Rahman [49] and Dingemans [50].

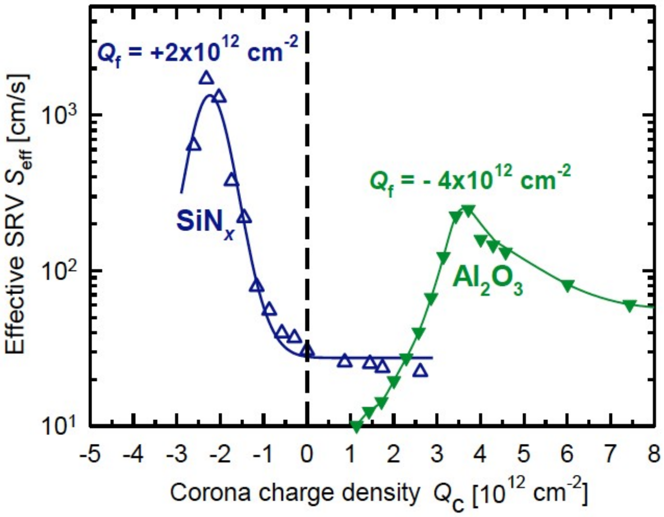

Fig. 3.1: Effective SRV (S_{eff}) as a function of injected corona charge density (Q_c) in SiN_x and Al_2O_3 films giving a measure of fixed charge (Q_f) in the films [41]

The origin of negative fixed charge in Al_2O_3 film is still under discussion. Al vacancies and O interstitials are known to be negatively charged and possibly the reason for high fixed negative charge in the film [51-54]. Even though, ultra-thin (10 nm) Al_2O_3 film can provide good passivation, there are some issues with Al_2O_3 film that need to be addressed before it can be integrated as a standard industry wide process. Most common deposition process used to deposit Al_2O_3 films is thermal ALD process. The deposition process is a self-limiting reaction consisting of two half reactions that requires purging the reactor chamber with an inert gas after every dose of pre-cursor gases. This requirement severely limits the deposition rate of ALD process ~1-2 Å per cycle, that makes this technique unsuitable for high volume manufacturing. New deposition techniques like PECVD, APCVD, sputtering are currently being developed for the deposition of Al_2O_3 films. Currently, the Al_2O_3 film is deposited by Atomic Layer Deposition (ALD) technique. Further, Al_2O_3 film with refractive index of 1.65 is not suitable to act as a stand-alone anti-reflection film. Even though, the Al_2O_3 film provides excellent rear side passivation for p-type cells, a SiN_x capping layer is still required to prevent processing damages to the Al_2O_3 film and to increase the rear side reflection for the IR spectrum of the incident light [55-58]. Moreover, as of now, there are no metallic pastes available for Al_2O_3 film that can easily penetrate during firing step to form a proper ohmic contact with the underlying silicon at the rear side. This limitation adds an extra step of laser firing to make rear contacts that significantly increases the final product cost.

All the above mentioned issues with the application of Al_2O_3 films indicate that significant amount of research is still required to make Al_2O_3 films suitable for large scale industrial production and puts the focus back on SiN_x films that have been used in the PV industry in the past and raises a question that can SiN_x films carry negative charge instead of as-deposited positive charge. Determining a solution to this problem is the primary motivation for this PhD work. Prior to understanding how negative charge can be injected in the SiN_x films, a review of important properties of SiN_x films is given in the following section.

3.2 Silicon nitride (a-SiN_x:H) films with fixed positive charges

Optimized hydrogenated amorphous silicon nitride (a-SiN_x-H, SiN_x in short) films have been used for the past three decades as passivating films for crystalline silicon solar cells. Along with passivating the surface and bulk defects, the SiN_x films are also used as anti-reflection coating and show excellent thermal and UV stability making the SiN_x films versatile and industry favorite. SiN_x film consists of fixed positive charges, originating from dangling silicon nitride bonds, known as K centers that reduce surface recombination through field-effect passivation. The large positive fixed charge density Qf = 3 - 7 x 10^{12} cm^{-2} in SiN_x film effectively passivates highly doped n-type c-Si or n^+ emitters by shielding the minority holes away from the surface. However, the same positive Q_f attracts minority electrons towards the surface in lightly or moderately doped p-type wafers or p type emitters, thereby, inverting the p-doped surfaces.

SiN_x:H films provide excellent surface passivation due to presence of fixed positive charges (field effect passivation) and due to large percentage of atomic hydrogen (chemical passivation). Lauinger et al. reported record low S_{eff} value of 4 cm/s on remote-plasma SiN_x coated 1.5 Ω.cm FZ p-Si samples (Fig. 3.2) [59], whereas, Kerr and Cuevas reported SRV of 1 cm/s on high resistivity n- and p-type Si substrates passivated with silicon nitride film [60]. Similarly, several other researchers have reported excellent surface and bulk passivation obtained from PECVD deposited SiN_x films [61-72].

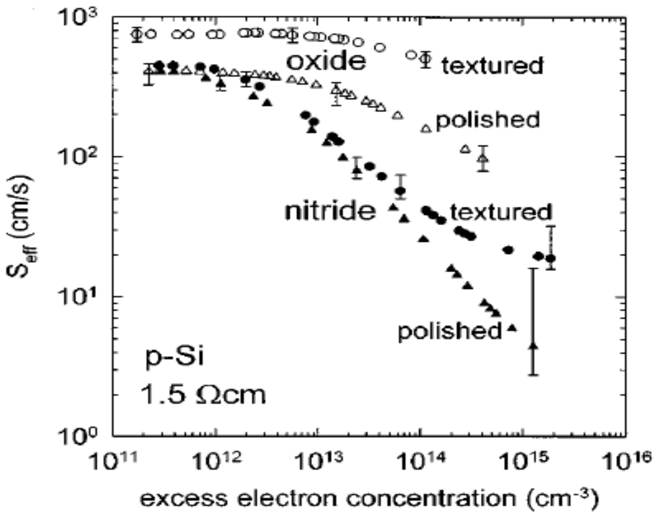

Fig. 3.2: Measured S_{eff} as a function of excess carrier density Δn for polished and textured 1.5 Ω.cm FZ p-Si wafers passivated by remote plasma SiN_x and thermally grown SiO_2 [59]

SiN_x properties primarily depend on the deposition parameters like NH_3/SiH_4 gas flow ratio, plasma pressure and deposition temperature. The N/Si ratio (x) determines the band-gap and refractive index of the film. Increasing the Si content in the SiN_x film moves the conduction band and the valence band towards mid-gap, thereby, reducing the band-gap. As Si concentration increases, the films change from stoichiometric silicon nitride (bandgap ~ 5.3 eV) to amorphous silicon (~ 1.8 eV) [73-79]. SiN_x anti-reflective coating works by creating a destructive interference of incoming photons and reflected photons from the Air/SiN_x/Si interface. The required refractive index (n) for bare wafers (Air/SiN_x/Si) is 2.0 and for the case of encapsulated cells (Air/glass-EVA/SiN_x/Si), n is 2.3. However, higher refractive index also increases the light absorption in the ARC layer itself. Layers with higher absorption coefficient (α) absorb more incoming light rather than transmitting it and these absorbed photons do not contribute to useful current in the cell. Therefore, a trade-off between refractive index (n) and extinction coefficient (k) is made by varying the ratio of NH_3/SiH_4 gas flows so than an optimum refractive index of 2.08 and thickness of 78 nm is achieved.

3.3 Origin of charges in SiN_x films: K centers

The properties of the defects or traps present in the SiN_x films were first investigated during the extensive research on Metal Nitride Semiconductor (MNS) structures and Metal Nitride Oxide Semiconductor (MNOS) memories in 1970s. For both the MNS and MNOS structures, hysteresis behavior was reported that indicated the presence of traps at the nitride-silicon or nitride-oxide interface and possibly in the nitride bulk [86-89]. These traps in MNOS memories charged or discharged based on the applied gate bias, oxide thickness and also on the conductivity of the nitride films to give a distinct hysteresis behavior. As seen in Fig. 3.3, for a positive applied voltage at the gate metal, the electrons in the conduction band of the silicon substrate can tunnel (FN tunneling) through the thin oxide layer (~ 50 Å) into the nitride layer. The electrons get trapped by the defects present at the nitride-oxide interface and also in the bulk of the nitride film. The conduction of electrons in the nitride bulk is believed to be due to Poole - Frenkel (PF) tunneling mechanism through the hopping of electrons on the defect levels. However, different conduction behavior is observed for different thicknesses of the oxide layer. In order to determine the location (centroid) of the charge, several studies were done using chemical etch-back and capacitance-voltage (CV) techniques on MNOS devices with both thin as well as thick oxide layers [90-92]. Kapoor and co-workers [93, 94] demonstrated that the traps were distributed throughout the bulk of the nitride film and not just at the nitride-oxide interface, whereas, Robertson worked extensively to determine the gap states and electronic structure of silicon nitride films [95-97].

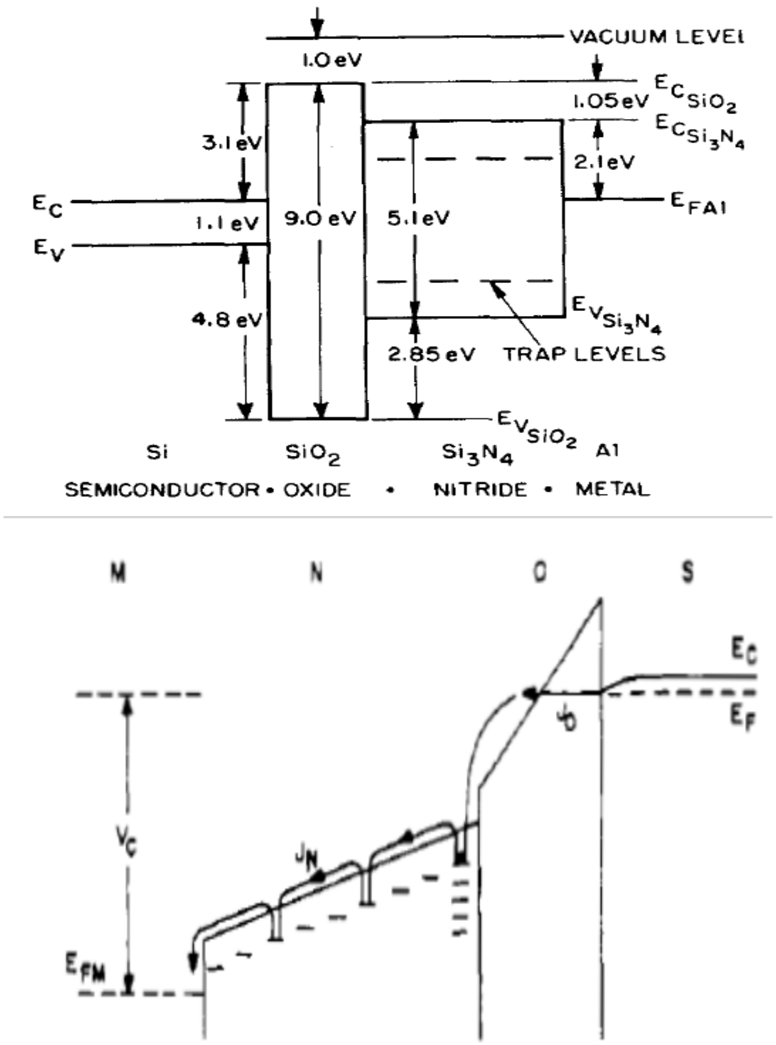

Fig. 3.3: Band diagram of MNOS structure [86, 93]

Later in 1981, Yokoyama and co-workers published the first ever results from Electron Spin Resonance (ESR) measurement taken on plasma-deposited silicon nitride films [98]. ESR signal arises due to the presence of paramagnetic defects present in the sample. Yokoyama and co-workers assigned the presence of ESR signal to silicon dangling bonds present in the SiN_x films. It was well established by this time that electrical behavior of SiN_x films were dominated by deep trapping centers that played a critical role in non-volatile MNOS memories. However, there was no experimental evidence available that connected a specific defect in the SiN_x film with the charge trapping behavior. Krick and co-workers identified this trapping center in the SiN_x film to be a $\cdot Si\equiv N$ dangling bond, known as K Center [99-102]. This defect is paramagnetic when neutral (K^0) but diamagnetic when either positively charged K^+ (no spin) or negatively charged K^- (two spins). ESR along with Capacitance-Voltage (C-V) measurement technique was used to detect and quantify the K center defect density. The researchers also found that illuminating the SiN_x film with high energy UV (~ 4.9 eV) increased the paramagnetic signal. UV light was found to annihilate all the charges present in the film (K^+ or K^-) and convert them to neutral paramagnetic K^0 centers. It was suggested that the sub-band gap absorption of UV light simply changes the spin and in turn, the charge of the K center through a process known as photobleaching. No chemical or structural change in the SiN_x film was determined after UV illumination [100-109].

K center defects act as amphoteric traps (Fig. 3.4) that can trap either an electron or a hole according to the Eqs. 3.1 and 3.2.

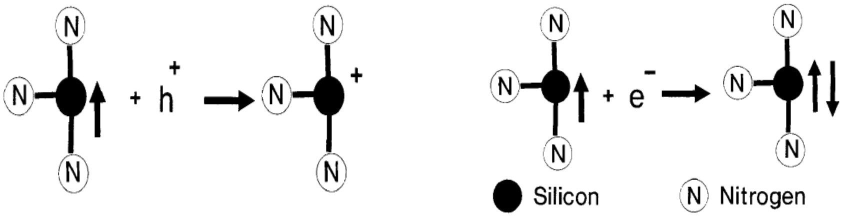

Fig. 3.4: K center - amphoteric defect [126]

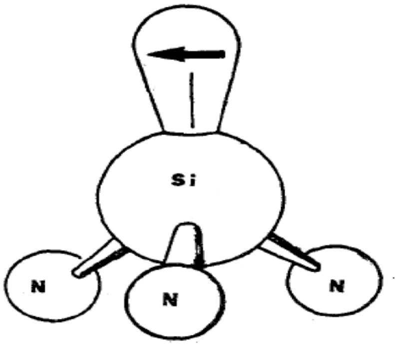

Fig. 3.5: Si atom bonded with three nitrogen atoms - K center [119]

$$K^{o}(\uparrow)+e^{-}\rightarrow K^{-}(\uparrow\downarrow) \qquad 3.1$$

$$K^{o}(\uparrow)-e^{-}\rightarrow K^{+}() \qquad 3.2$$

Lenahan and others further enhanced the understanding of K center defects, the primary trapping defects present in the SiN_x films, by utilizing Electron Nuclear Double-Resonance (ENDOR) to distinguish between silicon and nitrogen dangling bonds and to determine the structure of the defect [111-120]. They determined with certainty that the silicon dangling bond with three nitrogen atoms (·Si≡N) is the primary defect responsible for charge trapping and the electronic wave function is strongly localized on the central Si atom (70%) and weakly localized on the N atom (1-3% on each). This unpaired spin, present on the silicon atom bonded with three nitrogen atoms (Fig. 3.5), gives the paramagnetic signal detected by ESR technique. It was also determined that due to strong negative electron-electron correlation energy, K^- defect state with two spins is energetically more stable than the neutral K^o defect with single spin of electron, making the K^o defect metastable in nature [121-128]. Comparing the binding energies of an electron in K^- (↑↓) defect with a neutral K^o (↑) defect, and assuming E_1 to be the binding energy of the electron in K^- (↑↓) defect, we get,

$$K^{-}(\uparrow\downarrow)+E_{1}-e^{-}\rightarrow K^{0}(\uparrow) \tag{3.3}$$

Similarly, if E_2 is the binding energy of electron in K^0 () defect then,

$$K^{0}(\uparrow)+E_{2}-e^{-}\rightarrow K^{+}() \tag{3.4}$$

In this case, it was found that $E_1 > E_2$, thereby, requiring more energy to take an electron from K^{-} (↑↓) defect compared to a neutral K^0 (↑) defect.

3.4 Role of SiN_x positive charges in silicon solar cell performance

Hezel and co-workers pioneered the work in bringing the SiN_x films from the semiconductor industry to the PV industry. Early integration of PECVD deposited SiN_x films for silicon solar cell application was carried during the development of Metal-Insulator-Semiconductor Inversion-Layer (MIS-IL) solar cells (Fig. 3.6), where, SiN_x films were first used as a front dielectric layer. Presence of very high positive charge density (Q_f = 5 x 10^{12} / cm^2) in the SiN_x films deposited at the front surface created a strong, conductive inversion layer emitter on p-type Si substrate (Fig. 3.7) [129, 130]. Other advantages of using the SiN_x film were: 1) PECVD being low temperature process compared to thermal oxide process, 2) long term stability of fixed positive charges in SiN_x films, 3) low interface defect density D_{it} (~ 4 x 10^{10} cm^{-2} eV^{-1}), 4) excellent anti-reflection properties, and 5) excellent passivation of surface as well as bulk defects. Application of negative voltage pulse to the SiN_x film or Cesium contamination led to increased magnitude of positive charges up-to 1.4 x 10^{13} cm^{-2} in the SiN_x film that further strengthened the inversion layer [131, 132]. As a result of these properties, MIS-IL cells were reported to achieve total area efficiencies up-to 14.4% on mono-Si cells and 12.3% on multi-crystalline silicon cells [130].

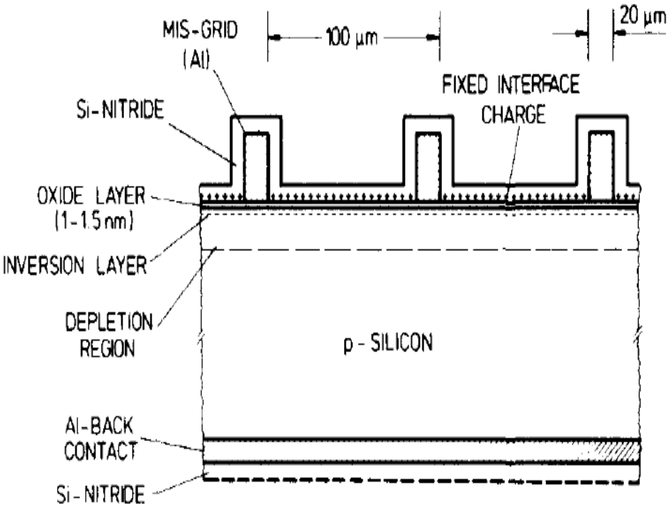

Fig. 3.6: Schematic of MIS-IL solar cell [129]

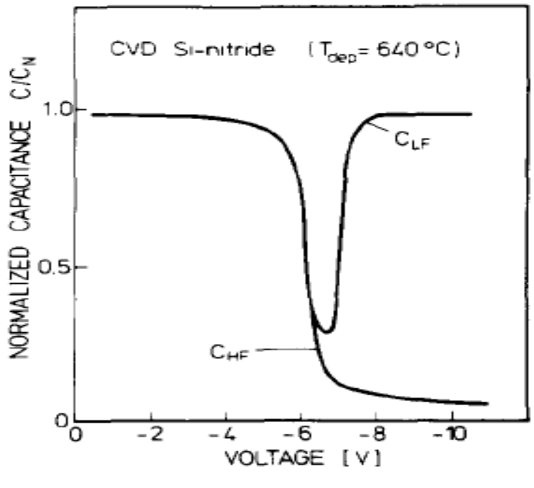

Fig. 3.7: High frequency (C_{HF}) and quasi-static (C_{LF}) C-V curves of Al/70 nm SiN_x/ultra-thin SiO_xN_y/Si showing the presence of high fixed positive charge ($Q_f = 3 \times 10^{12}/ cm^2$) [131]

Later, Aberle [20, 65] proposed that the measured positive charge in the SiNx film consists of a constant contribution from an ultra-thin silicon oxynitride (SiO_xN_y) interfacial film along with the K^+ centers present in the SiN_x film (Fig. 3.8).

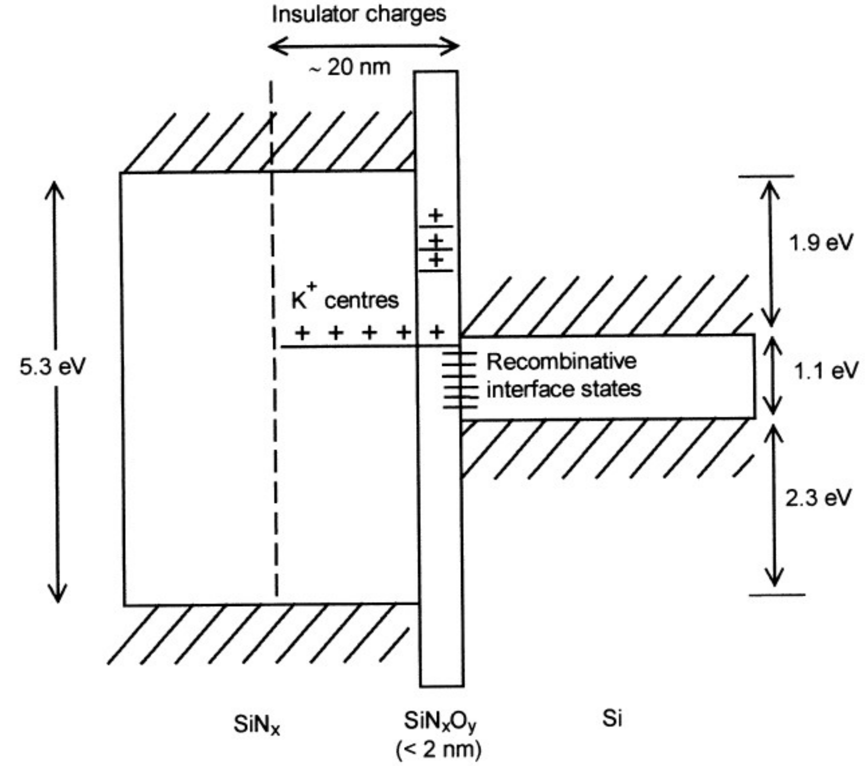

Fig. 3.8: Energy band diagram of the Si-SiN_x interface showing the distribution of positive insulator charge ($+Q_f$) up-to 20 nm in the SiN_x film [65]

The thin SiO_xN_y interfacial film grows on the silicon substrates during the time elapsed between cleaning the substrate and deposition of silicon nitride in the PECVD tool. According to Aberle, these positive charges are located only up-to ~20 nm from the interface within the SiN_x film. This model for charge distribution was based on similar work carried by Elminger and Kunst [133], where the authors measured the conductance of silicon wafer coated with SiN_x film on both sides. They found that the measured conductance of the wafer increased as the thickness of the SiN_x film increased up-to a thickness of 20 nm, where after, a constant conductance was measured. However, as it will be shown later in the results section (Ch. 5) using C-V etch-back technique and Electron Spin Resonance (ESR) measurements, it was found in this work that the charge trapping K centers are distributed throughout the bulk of SiN_x film and not just up-to 20 nm from the interface.

Further, Schmidt and Aberle [63] also proposed the magnitude of positive charge density ($+Q_f$) under illumination should be atleast one order of magnitude lower (~ 1 x 10^{11} cm^{-2}) compared to the value measured in dark by C-V measurements in order to satisfy extended SRH surface recombination model (Fig. 3.9). However, Dauwe [134, 135] later proved that this assumption of decrease in the value of $+Q_f$ under illumination does not hold true by considering space charge region recombination and further stating that under low level injection conditions or under strong inversion conditions at the surfaces, the difference between the conduction band edge (E_C) and the electron quasi fermi level (Φ_n) is independent of illumination levels.

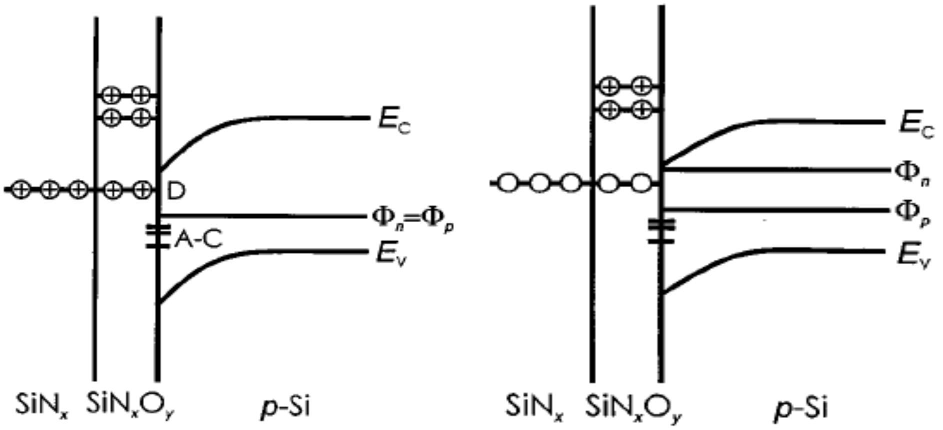

Fig. 3.9: Band diagram and energetic positions of different defect states at Si-SiN_x interface in the dark (left) and under illumination (right) [63]

Cai and co-authors [76] utilized neural network modeling to understand the properties of positive charge density and bonded hydrogen content in SiN_x films. It was reported that the positive charge density increased with increase in deposition temperature and the surface recombination velocity decreased with increase in the magnitude of positive charge density in the film. Mäckel and Lüdemann [136] proposed a model for the formation of K^+ defects in the SiN_x films, where they suggested that the N-H bonds act as pre-cursors for the K^+ defects. Using FTIR measurements, they showed that as N/Si ratio in the SiN_x film increased, the N-H bond density increased too leading to an increasing in K^+ defect density in the film. A.J.M van Erven et al. [137] studied the effect of Si/N ratio in the SiN_x films on C-V characteristics. They reported that the N-rich SiN_x films (refractive index $n = 1.92$) show a small hysteresis during the C-V measurements whereas; Si-rich SiN_x films ($n = 2.32$) show a much larger hysteresis loop. This hysteresis during C-V measurements is caused by charge injection from the silicon substrate with applied bias and is higher for Si-rich films due to increase in silicon dangling bonds in the film. Similar results were reported by De Wolf and co-authors [138]. Recently, researchers at the Australian National University (ANU) led by Klaus Weber investigated the properties of charge injected into the SiN_x films from the underlying Si substrate using corona charging concept. Some important aspects of charges e.g. thermal stability, effect of deposition conditions, location of charge are addressed in their published results [139-142].

The work reported in this dissertation further enhances the fundamental knowledge on properties of charge present in SiN_x films that will allow the application of SiN_x to both n and p-doped wafers for charge assisted passivation. It was determined from this work that the as-deposited PECVD deposited standard SiN_x film carries neutral K^0 defect that can be converted to either positive or negative charge. Further, this neutral K^0 defect is spread throughout the bulk of the SiN_x film implying that the injected charge will be present in the bulk of the SiN_x film and not just at the interface. The source of as-deposited positive charge (~ 2-5 x 10^{11} cm^{-2}) present in non-treated SiN_x films is due to large number of interface defect charge (N_{it}) located at the Si-SiO_xN_y-SiN_x interface and few K^+ defect centers. Further details about the experiments and results are reported in chapter 5.

Chapter 4

SiNx FILM OPTIMIZATION, CHARACTERIZATION TECHNIQUES AND TEST STRUCTURES

4.1 Optimization of SiN_x deposition process

An optimized process for depositing SiN_x films was required so that the results from the current work can be easily compared with standard industrial process. A detailed Design of Experiment (DOE) method was used to achieve optimized output parameters of the SiN_x films e.g. refractive index n = 2.0-2.1, film thickness = 75-80 nm, high minority carrier lifetime, good uniformity of deposition and stability of the SiN_x films after high temperature firing step. The DOE approach allowed creating experiments with varying levels of process controlling inputs e.g. power, pressure, temperature, etc. and therefore, helped determine which inputs had the highest influence on the desired output responses. A Response Surface Methodology (RSM) was used to create a model that relates the input parameters with the desired outputs. The RSM approach is a sequential procedure where, the results from the first set of experiments are often away from the desired optimum results. The output responses from the first experiment can be easily modeled with simple first order function of input variables and plotted on contour plots. The goal is to then proceed with a second follow-up experiment, typically fitted with a curved surface, along a path of steepest ascent (direction of improvement in output responses) towards optimum region that allows optimizing the input parameters efficiently. For this work, SiN_x films were deposited using Applied Materials P5000 PECVD tool at the Solar Power Lab (SPL). The deposition temperature was fixed at 350 °C and three input parameters were the RF power, pressure, gas flow ratio (% of SiH_4 in NH_3). A central composite design was used for the three input parameters with varying levels that gave a total of 20 different run conditions: 6 axial points, 8 fractional factorial points and 6 center axial points for repeatability as seen in Table 4.1.

TABLE 4.1: SiN_x deposition run conditions

Sample	Pattern	Comment	Power	Pressure	Gas ratio (SiH_4 in NH_3)
			(W)	(Torr)	(sccm)
1	-00	Axial	49	3.0	49.95
2	0+0	Axial	175	4.7	49.95
3	000	Center-Ax	175	3.0	49.95
4	-++	FF	100	4.0	78.3
5	+--	FF	250	2.0	21.6
6	--+	FF	100	2.0	78.3
7	000	Center-Ax	175	3.0	49.95
8	++-	FF	250	4.0	21.6
9	-+-	FF	100	4.0	21.6
10	+-+	FF	250	2.0	78.3
11	000	Center-Ax	175	3.0	49.95
12	---	FF	100	2.0	21.6
13	00-	Axial	175	3.0	2.27
14	00+	Axial	175	3.0	97.6
15	+00	Axial	301	3.0	49.95
16	000	Center-Ax	175	3.0	49.95
17	0-0	Axial	175	1.3	49.95
18	000	Center-Ax	175	3.0	49.95
19	+++	FF	250	4.0	78.3
20	000	Center-Ax	175	3.0	49.95

Detailed characterization of all the run samples was done to measure output responses, primarily using techniques such as Variable Angle Spectroscopic Ellipsometry (VASE) for thickness and refractive index measurements and Photoconductance for minority carrier lifetime measurements. The response data was analyzed using statistical software JMP to achieve the final optimized deposition condition for the SiN_x films. One of the most important and useful interactive tool in JMP is the Prediction Profile tool that allows changing one input variable at a time and looking its effect on the predicted response (Fig. 4.1). Since, a target value for refractive index and film thickness was required, the Prediction Profile tool allowed tweaking the input parameters to achieve higher desirability on output responses. The film parameters obtained using optimized deposition conditions are listed in Table 4.2.

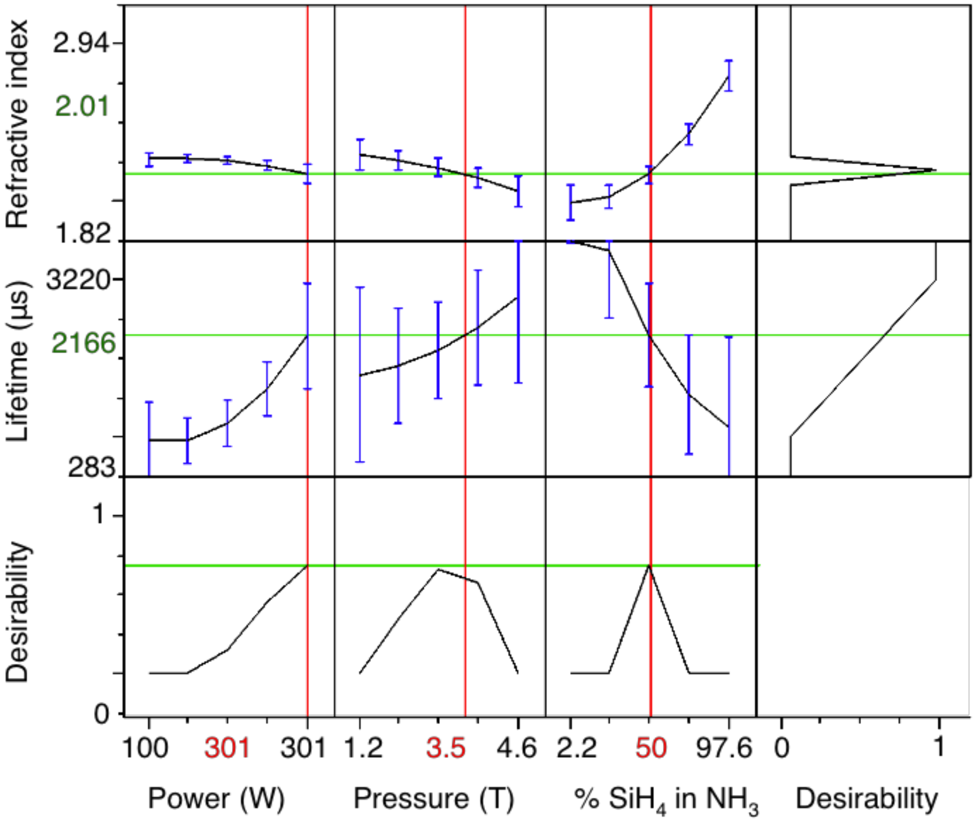

Fig. 4.1: JMP Prediction Profile tool output to optimize SiN_x deposition parameters

TABLE 4.2: Optimized parameters of SiN_x film

Thickness	Refractive index (n)	Absorption coefficient (α)	Lifetime	SRV	Thickness non-uniformity
(nm)	(@ 630 nm)		(μs)	(cm/s)	(%)
80	2.01	0	1257	18.9	3

4.2 Characterization techniques used in this work

4.2.1 Capacitance voltage

The primary aim of this work was to understand the charges present in the SiN_x film. Capacitance-voltage (C-V) technique was extensively used to characterize the nitride film and quantify the magnitude, sign and distribution of the charge. C-V measurements were taken according to the ASTM standard F 1153-88 [143], to determine the amount of fixed charges present in the samples through flat band voltage (V_{FB}). An excellent book covering the background theory on MOS capacitors is written by Nicollian and Brews [144].

C-V measurements are used to quantify different types of charges present in the oxide, e.g. interface trapped charge (N_{it}), fixed oxide charge (N_f), oxide trapped charge (N_{ot}), and mobile oxide charge (N_m). In this work, the measured charge was assumed to be the sum of interface trapped charge and fixed charge present in the silicon nitride or thermally grown oxide films. In order to explain the basics of C-V measurements, a MOS-Capacitor (MOS-C) on a p-type substrate is used as an example (Fig. 4.2). Here, t_{ox} is the thickness of the oxide film, W is the depletion region width and V_G is the applied gate voltage. Capacitance C is the change in charge (dQ) due to a change of voltage (dV). In case of MOS-C, applying a varying voltage at the metal gate (dV_G), changes the charge on the gate (dQ_G), that in turn is reflected and balanced by an equal and opposite change in semiconductor charge given by Eq. 4.1:

$$C = \frac{dQ_G}{dV_G} = \frac{dQ_s + dQ_{it}}{dV_{ox} + d\phi_s} \qquad 4.1$$

where, Q_S is the semiconductor charge, Q_{it} the interface charge, V_{ox} being the voltage drop across the oxide, and Φ_S is the surface potential. Q_S is the sum of hole charge density (Q_p), electron charge density (Q_n) and space charge region bulk charge density (Q_b).

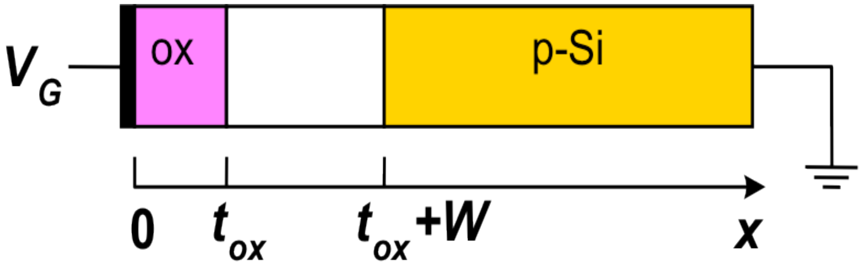

Fig. 4.2: Schematic of a MOS-Capacitor [18]

Therefore, Eq. 4.1 now becomes,

$$C = -\frac{1}{\dfrac{dV_{ox}}{dQ_s + dQ_{it}} + \dfrac{d\phi_s}{dQ_p + dQ_n + dQ_b + dQ_{it}}} \qquad 4.2$$

and can then be written as Eq. 4.3 and represented by Fig. 4.3.

$$C = \frac{1}{\frac{1}{C_{ox}} + \frac{1}{C_p + C_n + C_b + C_{it}}} \tag{4.3}$$

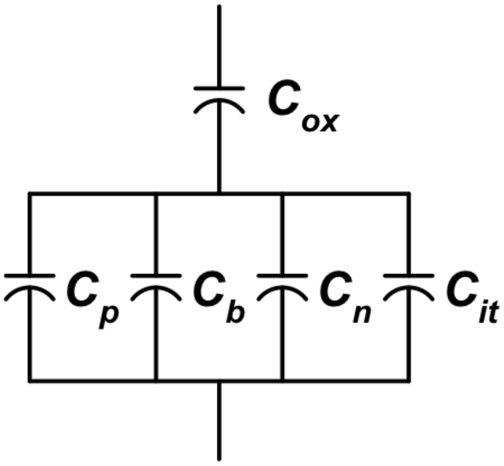

Fig. 4.3: Equivalent MOS-C circuit [18]

When negative gate voltage is applied on p-substrate, the surface gets accumulated with majority holes, capacitance C_p dominates over other semiconductor capacitances. The C-V meter sees this large C_p capacitance in series with a small C_{ox} capacitance and therefore, gives C_{ox} as the measured capacitance. When the gate voltage is moved towards zero and further in the positive direction, the surface becomes depleted and the bulk capacitance C_b of the space charge region in parallel to the interface capacitance C_{it} now comes in the picture. The measured capacitance is therefore, C_{ox} in series with a parallel connection of C_b and C_{it}. As the gate voltage is further increased in the positive direction, the surface starts getting inverted. However, this inversion capacitance depends on the frequency of the small signal ac gate voltage. If low frequency ac gate voltage is used, the minority electrons are able to follow the periodic changes in the gate voltage and create an inversion region, C_n increases, and low frequency C-V curve is measured (Fig. 4.4). On the other hand, if high frequency ac gate voltage (10 kHz - 1 MHz) is applied, the minority carriers (electrons in this case) are unable to follow the ac gate voltage and therefore, the applied gate signal is balanced by increased space charge bulk capacitance C_b and high frequency C-V curve is measured as shown in Fig. 4.4.

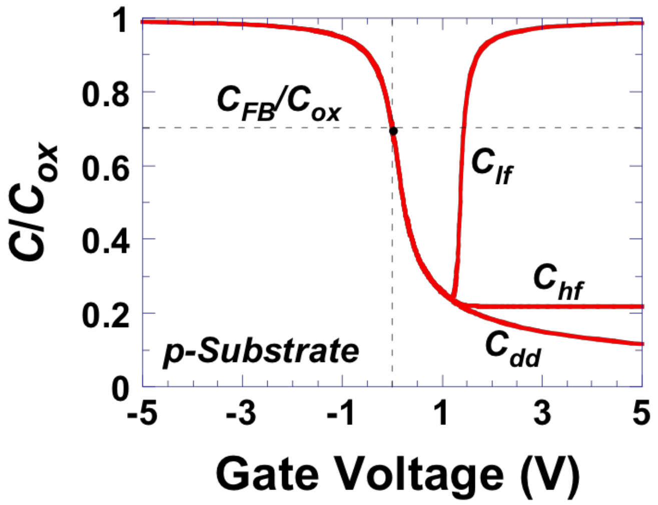

Fig. 4.4: Low frequency (lf), high frequency (hf) and deep depletion (dd) normalized SiO_2-Si C-V curves of a MOS-C [18]

The flat-band voltage (V_{FB}) is the voltage applied at the gate of the MOS-C that is able to make the semiconductor bands straight by balancing all the semiconductor charges. V_{FB} depends on the metal semiconductor work function (Φ_{MS}) and different oxide charges and is given by Eq. 4.4

$$V_{FB} = \phi_{MS} - \frac{Q_f}{C_{ox}} - \frac{Q_{it}(\phi_s)}{C_{ox}} - \frac{1}{C_{ox}}\int^{t_{ox}} \frac{x}{t_{ox}}\rho_m(x)dx - \frac{1}{C_{ox}}\int^{t_{ox}} \frac{x}{t_{ox}}\rho_{ot}(x)dx \qquad 4.4$$

where, ρ(x) is the oxide charge per unit volume as a function of thickness.

The fixed charge density (N_f) for any given sample in this work was calculated by the C-V software assuming that the charge density was located just at the interface between the film and the underlying silicon substrate. However, as will be shown in the next chapter, this assumption is not the exact picture as the K center defects were found to be distributed throughout the bulk of the nitride film and therefore, the true charge density can be bigger than the ones presented in this work. However, the fixed charge density N_f calculated by the software still is a good estimate to give an idea about the behavior of charge and the effect of various treatments (charge injection, UV illumination, annealing) on the magnitude of charge.

All the C-V test samples used for this work were boron doped (1-5 Ω.cm), p-type CZ silicon, 675 μm thick, prime grade, single side polished substrates. The C-V test structures were created by the following steps:

- Clean: Si substrate was cleaned in standard RCA B solution at 75 °C for 10 min, followed by a 10 min rinse in DI water and dried in a spin rinse dryer tool.
- Oxidation: A thin (~18 nm) layer of thermal oxide was grown in a thermal furnace at 950 °C for 20 minutes was on cleaned silicon substrates. The oxide layer was important because it stopped the charge movement causing hysteresis effect between the Si substrate and the SiN_x film.
- Forming Gas Anneal: Substrates were then annealed in forming gas (FGA, N_2/H_2) at 400 °C, 20 min to minimize the defects in the thermal oxide layer.
- SiN_x film deposition: 78-80 nm of SiN_x film was deposited on top of the thin oxide layer in Applied Materials AMAT P5000 PECVD tool. The deposition conditions were the same as described in Table 4.1

- Metal contacts: The contacts for taking C-V measurements were either Aluminum dots deposited using a shadow mask or a Mercury probe contact.

4.2.1.1 Nitride Silicon vs. Nitride Oxide Silicon C-V structure

Two different C-V test structures were created to measure the SiN_x film charge, one without a thin thermal oxide layer: Nitride-Silicon and one with the thin oxide layer: Nitride-Oxide-Silicon between the SiN_x film and Si substrate as shown in Fig. 4.5.

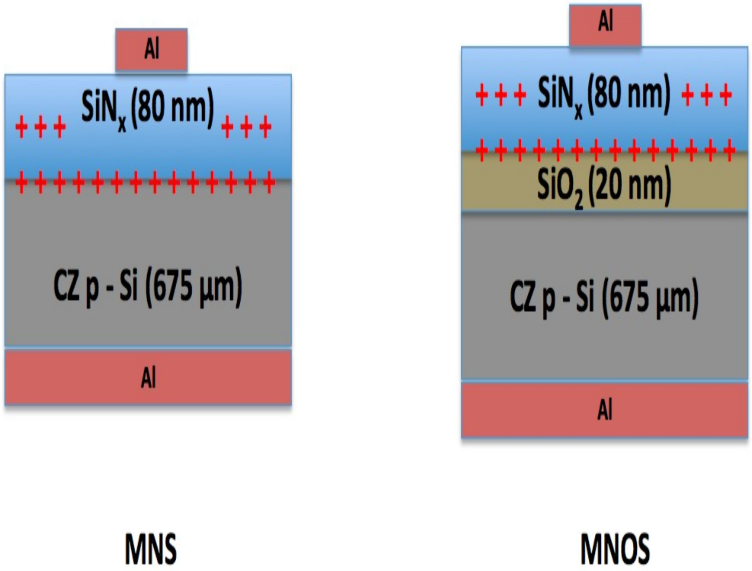

Fig. 4.5: Metal Nitride Silicon (left) and Metal Nitride Oxide Silicon (right) C-V test structures

When C-V measurements were taken on a Nitride Si structure, the applied gate voltage did not produce a proper accumulation, depletion or inversion region underneath the gate, compared to the C-V measurements taken on Nitride Oxide Si test structure as shown in Fig. 4.6.

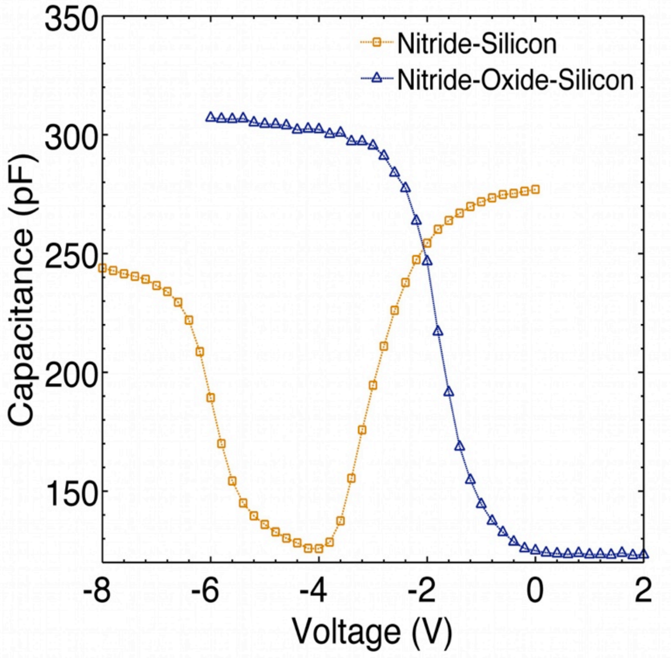

Fig. 4.6: C-V on Nitride-Silicon vs. Nitride-Oxide-Silicon structure

The non-stoichiometric SiN_x film, deposited in a PECVD tool contains lot of interface defects and charges. When a gate bias is applied on a Nitride Si structure, the applied voltage tries to create an accumulation or an inversion layer depending on the polarity. As soon as the gate voltage is increased in either direction, the charged carriers start moving under the influence of applied bias, between the nitride film and the silicon substrate due to the presence of interface defects and due to the high conductivity of the nitride film. The charges easily tunnel back and forth between nitride and silicon interface primarily due to Poole-Frenkel conduction and do not produce a stable accumulation or inversion region. However, as seen for the case of Nitride Oxide Si test structure, the thin thermal oxide layer (~18-20 nm) between the PECVD deposited nitride film and the silicon substrate, acts as a barrier that blocks the charge movement and allows the formation of accumulation and inversion layer of charges in the silicon substrate. Therefore, all the C-V measurements in this work were taken on MNOS structures.

4.2.1.2 Depositing Al dots: E-beam vs. thermal evaporation

To take C-V measurements on nitride samples, Al dots (~ 100 nm thick) were deposited to the front of the samples using a shadow mask. Initially, E-beam evaporator was used to deposit Al dots on the nitride-oxide layer. However, it was found that the flat-band voltage of the nitride-oxide layer with E-beam deposited Al dots, shifted to larger negative values, indicating a larger amount of positive charges in the film, compared to when the Al dots were deposited in a thermal evaporator, as shown in Fig. 4.7.

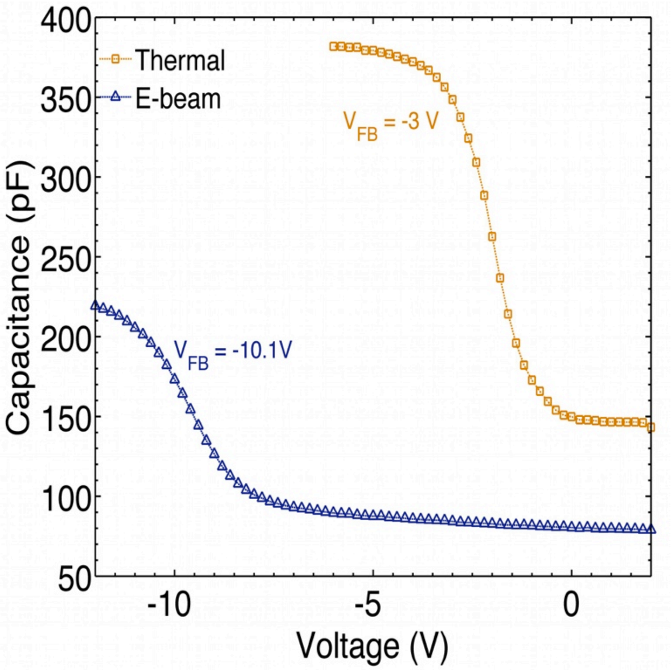

Fig. 4.7: C-V plot - E-beam vs. thermal evaporation of Al dots on nitride oxide silicon structures

The reason of this large positive charge injection was due to the damage induced to the nitride layer by radiations (X-rays) emitted during e-beam evaporation. This artificial shift in V_{FB} of nitride film was not acceptable, as it did not represent the true charges present in the film. As a solution to this problem, C-V measurements were taken on test structures with Al dots deposited using a thermal evaporator.

However, using depositing Al dots over the films prevented any further treatment on the samples once the metal dots were deposited. Since, the samples were subjected to UV illumination, charge injection or thermal annealing treatments, C-V measurements for most part of this work were taken primarily using a Hg probe C-V tool.

4.2.1.3 Selecting proper voltage bias sweep range

It is critical to carefully select the magnitude of applied voltage bias while taking the C- V measurements, to accurately quantify the magnitude and sign of charge in the SiN_x film. A large gate bias can induce a large field across the dielectric film. This applied field leads to Fowler-Nordheim tunneling of charges from the silicon substrate through the thin thermal oxide barrier layer and into the SiN_x film. These injected charges therefore, generate hysteresis during the C-V measurements leading to shifts in the V_{FB} and therefore, erroneous determination of the charges present in the SiN_x film (Fig. 4.8).

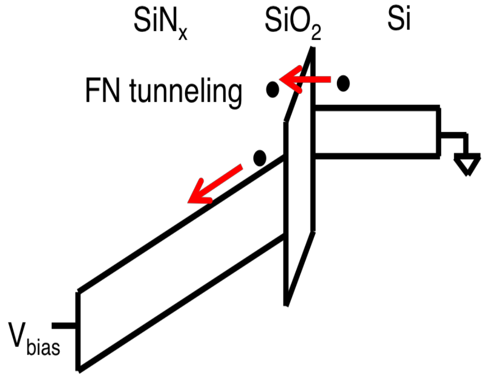

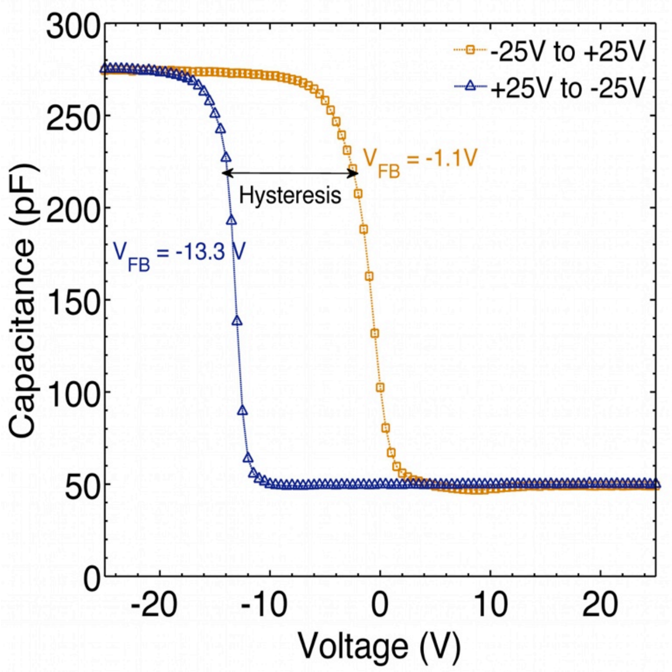

Figure 4.8: Simplified band diagram (top) and C-V plot (bottom) of SiN_x-SiO_2-Si showing hysteresis due to large applied voltage bias

Therefore, it is very important to use a small gate bias, enough to measure the V_{FB} and small enough to not inject charges through the oxide film (Fig. 4.9). Therefore, in this work, absence of hysteresis in C-V curves was always checked prior to taking any C-V measurements.

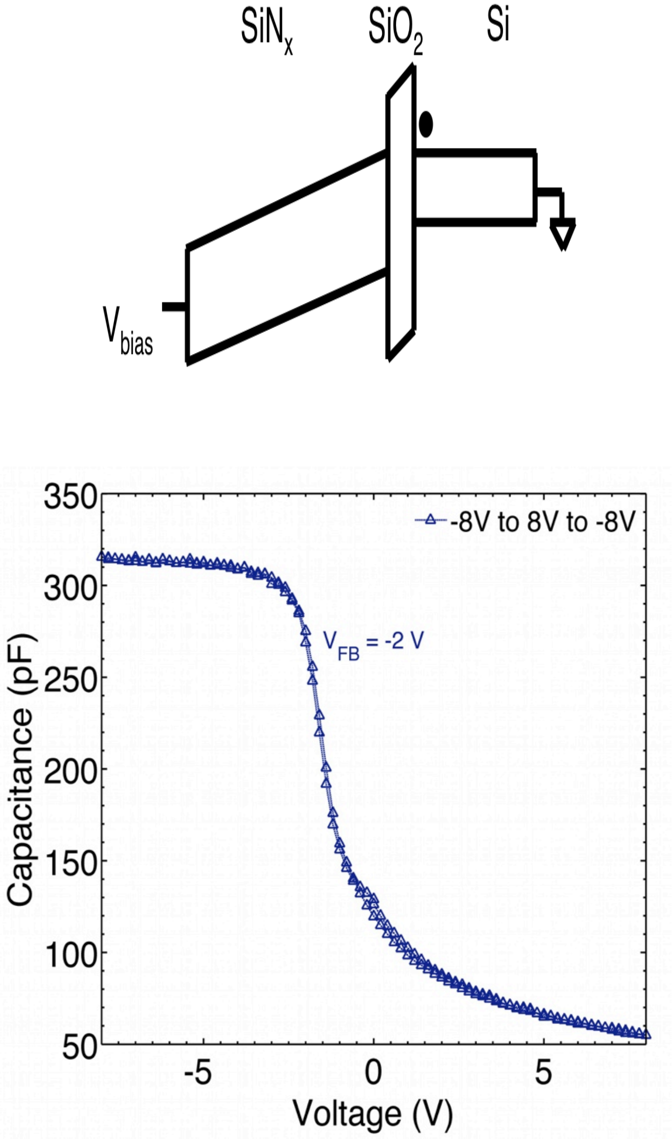

Figure 4.9: Simplified band diagram (top) and C-V plot (bottom) of SiN_x-SiO_2-Si showing no hysteresis due to small applied voltage bias.

4.2.2 Photoconductance

As previously mentioned in Chapter 2, the effective minority carrier lifetime τ_{eff} is controlled by different recombination events taking place in the bulk of the semiconductor or at the surfaces and is given by:

$$\frac{1}{\tau_{eff}} = \frac{1}{\tau_{SRH}} + \frac{1}{\tau_{rad}} + \frac{1}{\tau_{Auger}} + \frac{1}{\tau_{Surface}} + \frac{1}{\tau_{emitter}} \qquad 4.5$$

$$\frac{1}{\tau_{eff}} = \frac{1}{\tau_{bulk}} + \frac{1}{\tau_{Surface}} \qquad 4.6$$

To determine the effectiveness of the charges present in the thin films to passivate the surface defects and reduce the surface recombination, it is important to minimize the bulk recombination rate. For this work, high purity Float-Zone (FZ) silicon wafers with high bulk lifetime (τ_{bulk} > 10 ms) were used. After cleaning the wafers to remove the native oxide and metallic impurities, thin (~ 78 nm) SiN_x films were deposited on both sides of the FZ wafer sample (Fig. 4.10) to passivate the surfaces and to measure the effective lifetime (τ_{eff}) of the carriers and to determine the maximum upper limit of effective surface recombination rate S_{eff} using the Eq. 4.7:

$$\frac{1}{\tau_{eff}} = \frac{1}{\tau_{bulk}} + \frac{2S_{eff}}{W} \qquad 4.7$$

where, W is the thickness of the FZ Si sample.

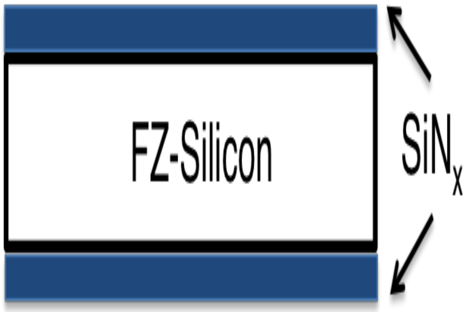

Fig. 4.10: Test structure for measuring effective carrier lifetime and surface recombination velocity

The minority carrier lifetimes of the samples were measured using a Sinton Photoconductance Lifetime Tester WCT 120 tool. Excess carriers in the test sample are created through optical generation by using a flash lamp. The continuity equation for uniform carrier generation in the sample is given by Eq. 4.8:

$$\frac{d\Delta n(t)}{dt} = G(t) - \frac{\Delta n(t)}{\tau_{eff}} \qquad 4.8$$

where, G(t) is the time dependent generation rate in the sample and Δn(t) is excess minority carrier density as a function of time. Therefore, the effective lifetime (τ_{eff}) of the sample as a function of minority carrier density is given by Eq. 4.9:

$$\tau_{eff}(\Delta n) = \frac{\Delta n(t)}{G(t) - \frac{d\Delta n(t)}{dt}} \qquad 4.9$$

Under transient photoconductance method, the illuminating flash duration is extremely small with $G(t) << \frac{d\Delta n(t)}{dt}$, therefore, τ_{eff} is now given as:

$$\tau_{eff}(\Delta n) = -\frac{\Delta n(t)}{\frac{d\Delta n(t)}{dt}} \qquad 4.10$$

Transient photoconductance method is valid only for samples with higher lifetime (τ_{eff} > 100 μs) so that the excess generated carriers can survive and their decay can be calculated.

On the other hand, under steady-state conditions, $G(t) >> \frac{d\Delta n(t)}{dt}$, making τ_{eff} now independent of carrier decay as:

$$\tau_{eff}(\Delta n) = \frac{\Delta n(t)}{G} \qquad 4.11$$

For the case of Quasi-Steady State Photoconductance (QSSPC) method, the sample is subjected to a long slow decaying pulse of light. This makes sure that the excess carriers generated in the sample are always close to stead-state conditions through nearly balanced generation and recombination rates. For the QSSPC method, both the generation rate G(t) and excess carrier density Δn(t) in the sample should be known. A picture of the Sinton photoconductance tool is given in Fig. 4.11.

Fig. 4.11: Sinton instruments WCT-120 wafer lifetime tester

Excess carriers generated in the sample by illumination, change the conductivity of the sample as explained by Eq. 4.12:

$$\sigma(t) = q(\mu_n + \mu_p)\Delta n(t) \tag{4.12}$$

The sample is inductively coupled to a RF coil that measures the change in sheet conductivity of the sample as a result of illumination and the excess carriers Δn(t) generated in the samples are thus calculated (Fig. 4.12).

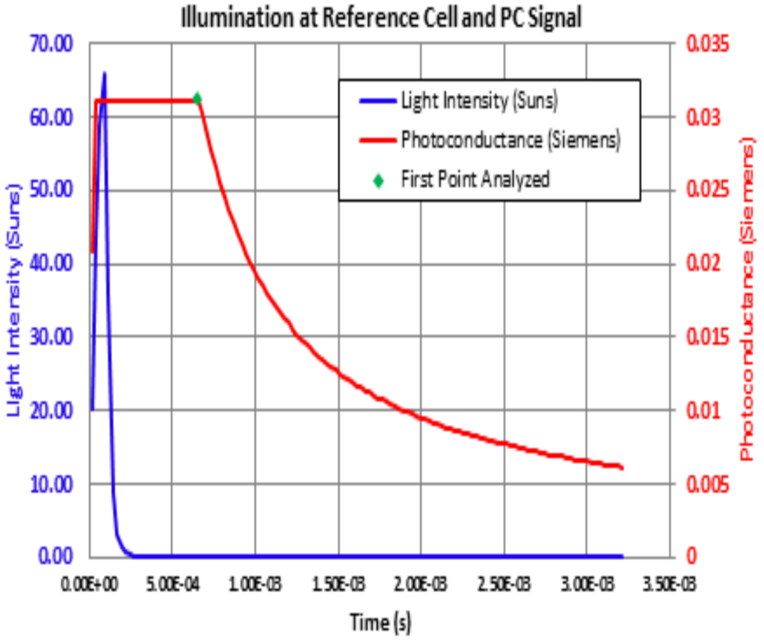

Fig. 4.12: Screen shot of light intensity and photoconductance vs. time (Transient measurement mode)

A calibrated reference cell is used to determine the generation rate G(t) through illumination intensity I(t) from the following relation:

$$G(t) = \frac{I(t).f_{abs}.N_{ph}}{W} \tag{4.13}$$

where, f_{abs} is the fraction of light entering the sample and depends on whether is sample is polished or textured or coated with anti-reflection film. N_{ph} are the number of photons under 1 sun illumination. Therefore, once $\Delta n(t)$ and $G(t)$ are known, τ_{eff} can then be easily calculated by Eq. 4.11 over a varying range of excess carrier concentrations as shown in Fig. 4.13.

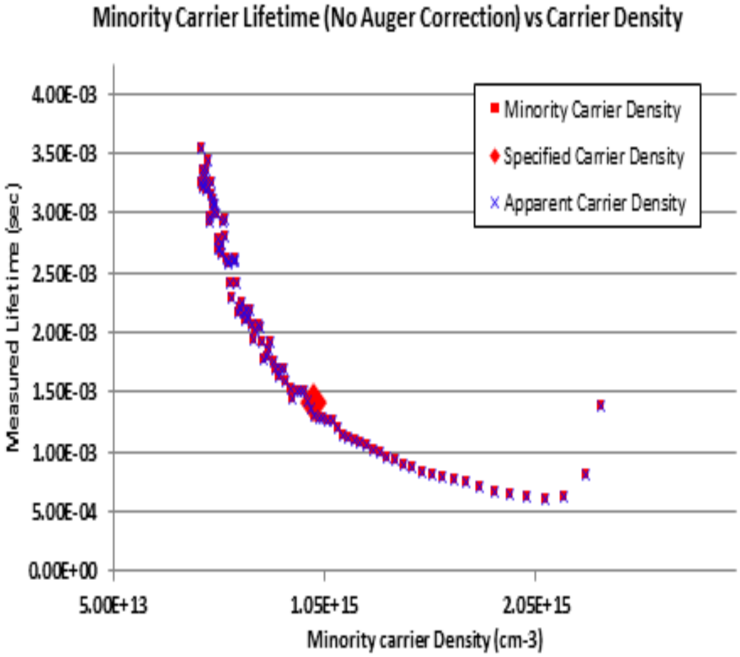

Fig. 4.13: Minority carrier lifetime τ_{eff} vs. excess carrier density Δn (t) plot

4.2.3 Electron Paramagnetic Resonance

Electron Paramagnetic Resonance (EPR) also known as Electron Spin Resonance (ESR) measurements were taken on silicon nitride (SiN_x) deposited silicon substrates to understand the properties of K center defects with single spin (neutral charge K^o defect) present in the nitride film. K center defects with single spin (neutral charge K^o defect) are paramagnetically active and hence, detected by ESR measurements. ESR measurements taken on these SiN_x films give direct evidence of the presence of silicon-nitrogen dangling bond (·Si≡N), also known as K center with single unpaired spin of electron. This neutral K center (K^o) with a single spin acts as an amphoteric defect and therefore, can capture either an electron or a hole. C-V measurements can determine the net charge present in the film but cannot quantify the neutral K center. ESR measurements on the other hand, can detect and quantify the density of neutral K centers present in the film. Therefore, C-V and ESR measurements are complimentary to each other and help understand the complete charge distribution in the nitride films. ESR measurements were used to quantify the total spin density in SiN_x samples and this spin density was compared with the fixed charge density (N_f) obtained from C-V measurements.

ESR technique is used to study materials that contain unpaired spin of electrons in their orbitals. The spin quantum number m_S describes the spin of the electrons. Every electron has a spin $s = \frac{1}{2}$ that makes the spin quantum number m_S to be $+\frac{1}{2}$ (up-spin) or $-\frac{1}{2}$ (down-spin). Every electron in a particular orbital must have distinct spins according to Pauli's exclusion principle, and therefore, a particular orbital can only have two electrons, each with an opposite spin.

Application of external magnetic field of strength B_o to the material (SiN_x in this case) splits the energy levels between the two spin states. The electron's magnetic moment m_S aligns itself parallel or anti-parallel to the field, with $m_S = -\frac{1}{2}$ (down-spin) being anti-parallel to the field and occupying a lower energy state. The separation between the energy states (Fig. 4.14) is given by Eq. 4.14, where μ_B is Bohr's magneton, a constant, defined as the magnetic moment for one unit of quantum mechanical angular momentum with a value of 9.274 x 10^{-20} J/T. B_o is the applied magnetic field strength and g_e = 2.002319 is known as the g-value for free electron, used as a correction factor for the anomalous magnetic moment of the electron.

$$\Delta E = g_e \mu_B B_o \tag{4.14}$$

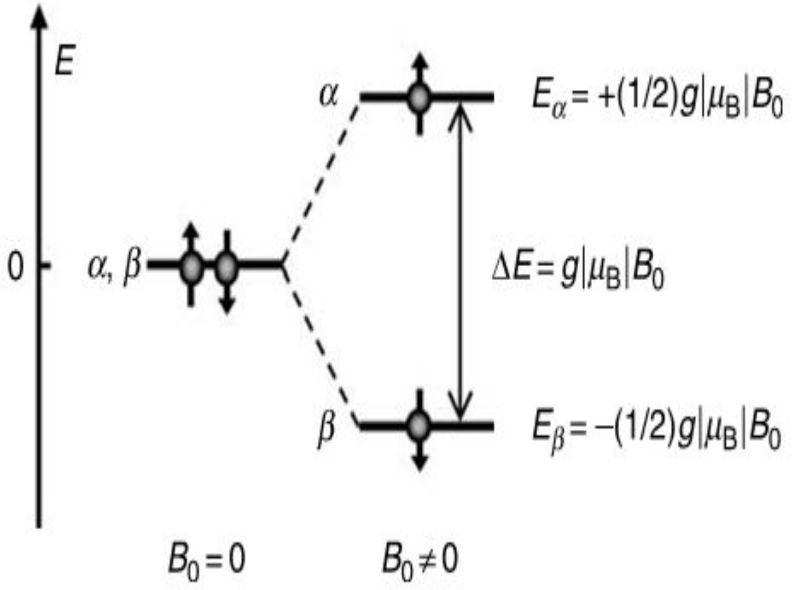

Fig. 4.14: ESR - splitting of energy levels with applied magnetic field [145]

When applied magnetic field B_o splits the energy levels, the unpaired electron with the single spin ($m_S = -\frac{1}{2}$; down-spin) makes a transition from the lower level to the upper level by absorbing the energy from an incident electromagnetic radiation with energy E = hν, so that the resonance condition of $\Delta E = E_{+1/2} - E_{-1/2} = h\nu$ is met. The frequency of the electromagnetic radiation is typically between 9-10 GHz (X-band).

Majority of ESR measurements are taken by varying the applied magnetic field and keeping the frequency of the incident electromagnetic radiation fixed. The electron from the lower spin state moves to the upper spin state by absorbing the incident energy of the radiation. This transition is measured and plotted as a first derivative of the absorbance of the incident electromagnetic radiation against magnetic field strength.

For this work, ESR measurements were taken at ESR facility at Arizona State University. All the measurements were taken at room temperature on a Bruker ELEXSYS 580 X-band spectrometer. The samples were the same PECVD deposited SiN_x films on silicon substrates that have been used for C-V and photoconductance measurements. Thin walled high purity glass tubes were used to hold the samples. The following parameters were selected for taking the ESR spectra: magnetic field modulation frequency 100 kHz, attenuation 29 dB, modulation 10 Gauss, and microwave power 0.25 – 1 mW. Spin densities (spins / cm^2) present in the samples quantifying an approximate number of neutral paramagnetic K^0 defect centers were determined by using Manganese Chloride ($MnCl_2$) solution as a calibration standard.

Chapter 5

PROPERTIES OF CHARGES IN SILICON NITRIDE: RESULTS AND ANALYSES

5.1 As deposited charge distribution

Solar cells are large area devices, so mapping the charges present in as-deposited SiN_x film was necessary to determine their uniformity and magnitude prior to any treatment. It was found that the deposition tool settings and the plasma plays an important role in the distribution of charges. Fig. 5.1 shows the charge distribution map of a sample with 80 nm thick SiN_x film. The wafer flat is located at the 180 radians.

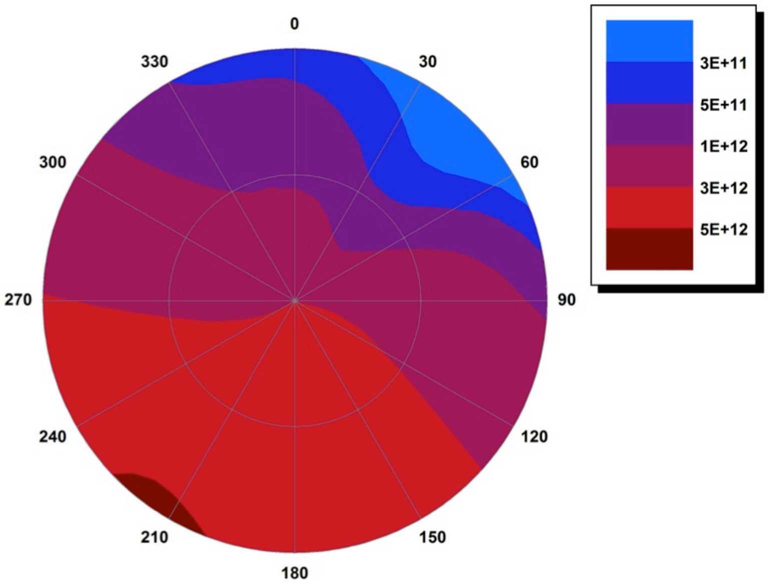

Fig. 5.1: Fixed charge density (charge/cm²) plot of a SiN_x film sample – tilted

As seen in the Fig. 5.1, the charge density gradually increases going diametrically from 30 radians to 210 radians. The reason behind this non-uniformity in charge deposition was later found to be a slight tilt between the silicon substrate and the showerhead for gas injection in the PECVD tool. Due to this slight tilt (< 5 mils), the deposited films were also slightly thinner in the same area around 30 radians, where lesser amount of charge was measured. After fixing the tilt in the PECVD tool and mapping the charge density in the SiN_x film again, the charges were more uniformly distributed in the wafer as seen in Fig. 5.2.

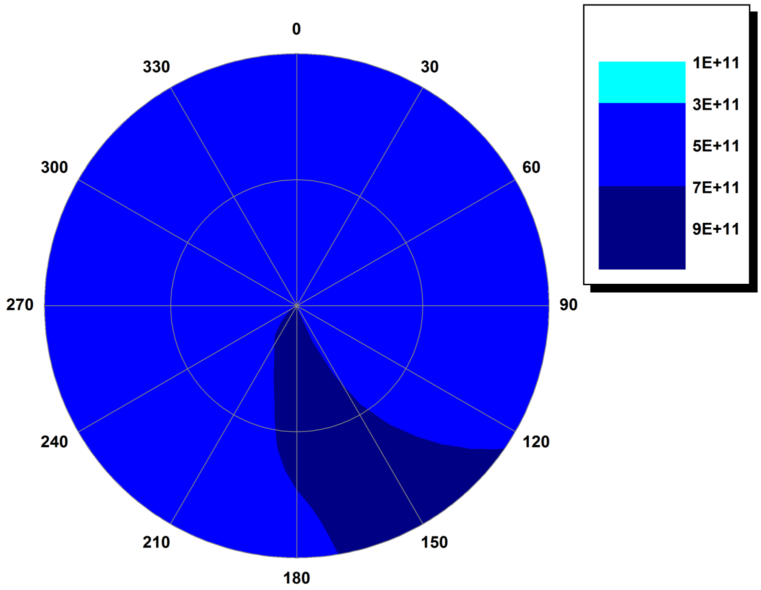

Fig. 5.2: Fixed charge density (charge/cm^2) plot of a SiN_x film sample after fixing the tilt

5.2 Effect of gate bias voltage

During regular C-V measurements of SiN_x samples, it was found that applying a suitable gate bias could easily change the magnitude and sign of charges present in the nitride film. First C-V measurement taken on an as-deposited (untreated) SiN_x film sample gave a V_{FB} of -1.8 V indicating a fixed charge density N_f of +3.5 x 10^{11} cm^{-2} present in the nitride film. After applying a gate bias of +40 V for 3 minutes prior to taking the second C-V measurement, the V_{FB} shifted to -11 V giving a net *POSITIVE* charge density of +2.1 x 10^{12} cm^{-2} in the film, as shown in Fig. 5.3. The net charge density in the nitride film increased by one order of magnitude by applying a positive gate bias. On the other hand, after applying a gate bias of -40 V for the same duration prior to taking the third C-V measurement, the V_{FB} was shifted to the positive side to +7.5 V, giving a net *NEGATIVE* charge density of -3.4 x 10^{12} cm^{-2} in the nitride film (see Table 5.1). This experiment proved that the K centers present in the nitride film behave as amphoteric defects that can trap both holes and electrons based on the applied external gate bias, thereby, giving a net positive or a net negative charge to the SiN_x film.

Another important point to take from this experiment is that the thin thermal oxide film (~18 nm) underneath the nitride film acted as a perfect charge blocking layer, preventing any charge movement between the silicon substrate and the nitride film. When +40V gate bias was applied to the nitride film, the electrons present in the as-deposited nitride film were pulled out by the applied bias and therefore, the net positive charge density in the nitride film increased. There was no sign of electron injection from the silicon substrate into the nitride film via tunneling through the thin oxide film, because, if this had been the case, net negative charge density would have been measured after applying positive gate bias. Similarly, applying a negative voltage of -40V on the gate injected electrons into the nitride film, giving rise to net negative charge density, clearly indicating that the source of these negative charges in the nitride film measured by C-V was the applied gate bias and not the silicon substrate. This gate bias experiment opened a way to manipulate the charges, positive or negative, in the nitride film by applying external bias of either polarity. The charges present in the SiN_x film can now be easily switched between positive or negative depending on whether the solar cell surface doping is n-type or p-type.

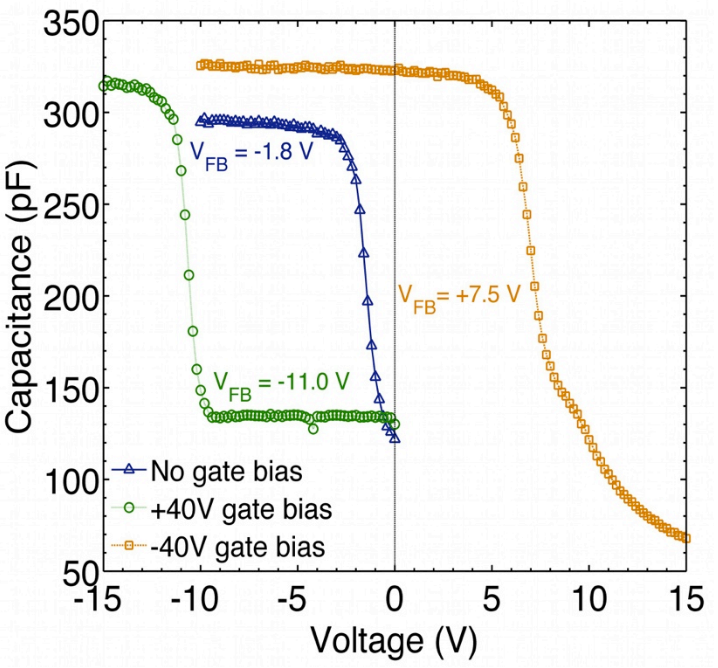

Fig. 5.3: C-V plot - Effect of applied gate bias on net charge density in the SiN_x film

TABLE 5.1: Effect of applied gate bias on the net charge density in the SiN_x film

Test#	Sweep	Gate bias	V_{FB}	N_f
	(V)	(V)	(V)	(cm^{-2})
1	0 to -10	N/A	-1.8	$+3.5 \times 10^{11}$
2	0 to -15	+40	-11	$+2.1 \times 10^{12}$
3	-10 to +15	-40	+7.5	-3.4×10^{12}

5.3 Corona charging for charge injection in SiN_x films

Once the gate bias experiments proved that the negative charge could easily be injected into the SiN_x films, a corona discharge tool was built to facilitate charging the nitride films with positive or negative charge. As previously explained, K centers being the primary charge trapping defects present in the nitride films exist in three different charge states: the neutral K^0, positively charged K^+ and the negatively charged K^- defects. The total population of the these K center defects remain constant depending on the total number of silicon-nitrogen dangling bonds (·Si≡N) present in the film, however, following the external injection of electrons or holes, the net charge in the nitride film changes.

For this work, a custom-built corona discharge tool was used for the charge injection process. The tool consisted of a thin copper wire connected to a positive or a negative power supply capable of voltages up to 20,000 V. The nitride film sample to be charged was kept underneath the copper wire at a distance of about 1 inch. Switching on the power supply created a discharge in the surrounding air by ionizing the oxygen, nitrogen and water molecules due to high voltage applied across the copper wire. The ions thus created, settled on the nitride sample kept underneath the copper wire and changed the charges present in the nitride film to net positive or negative depending on the selected discharge polarity. It was also found that the polarity of the injected charges in the film, subjected to the corona discharge, was the same as the polarity of selected corona voltage i.e. negative charges were injected in the nitride film after negative corona charging as shown in Fig. 5.4. Table 5.2 lists the charge densities measured on the SiN_x film samples following corona charging. After negative corona charging, the SiN_x film had a net *NEGATIVE* charge density of -6.9×10^{12} cm^{-2}. Similarly, a net *POSITIVE* charge density of $+4.6 \times 10^{12}$ cm^{-2} was measured after subjecting the SiN_x sample to positive corona charging. Corona discharge method thus proved to be the quick and easy method to change the net charge of the SiN_x film. Depending on the end application, whether the SiN_x film is to be applied on p-doped or n-doped surfaces, the net charge in the film can now be easily changed to negative or positive.

It is important to understand the source of negative or positive injected charges in the SiN_x film following corona charging. The silicon sample under the corona discharge was a heavily doped (1-5 Ω.cm) p-type substrate upon which an 18 nm thick oxide layer was thermally grown, followed by PECVD deposited 78 nm thick SiN_x film. The oxide layer prevented any charge movement from the silicon substrate into the nitride film or vice versa. Therefore, the charges injected in the film following corona discharge treatment must have come from the ions generated due to corona discharge of air.

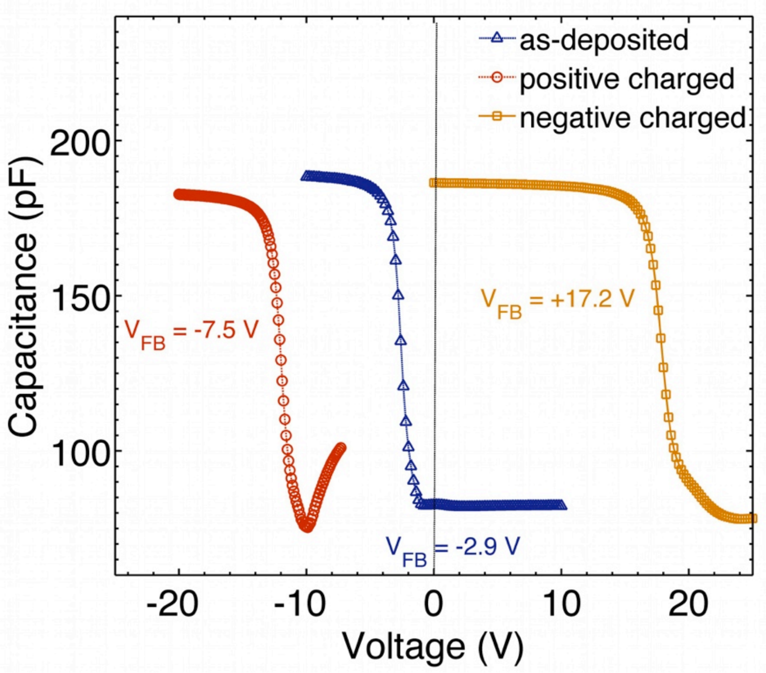

Fig. 5.4: Manipulation of charge in the SiN_x film using corona discharge technique

TABLE 5.2: Effect of corona charging on the net charge density in the SiN_x film

Test#	Condition	V_{FB}	N_f
		(V)	(cm^{-2})
1	As deposited	-2.9	$+3.3 \times 10^{11}$
2	Negative corona charged	+17.2	-6.9×10^{12}
3	Positive corona charged	-7.5	$+4.6 \times 10^{12}$

To investigate the relation between time duration of corona charging and charge injected in the SiN_x films, five samples taken from the same wafer were subjected to negative corona discharge for varying time durations. Standard nitride film thickness of 78 nm was used and the objective of this experiment was to understand if longer exposure of the nitride films to the corona charging translated to higher amount of injected charge in the film. After treating the samples with negative corona discharge, C-V measurements using a Hg probe were taken to measure the polarity and magnitude of the injected charge. As shown in Fig. 5.5 and listed in Table 5.3 the injected charge in the film saturated and reached its maximum just after a short 30 second exposure, indicating that the amount of injected charge in the SiN_x film is independent of the exposure time and just 30 seconds are enough to inject charges up-to 5 x 10^{12} cm^{-2}. This experiment thus allows corona charging technique to be integrated into the high volume solar cell production lines for fast charge injection process.

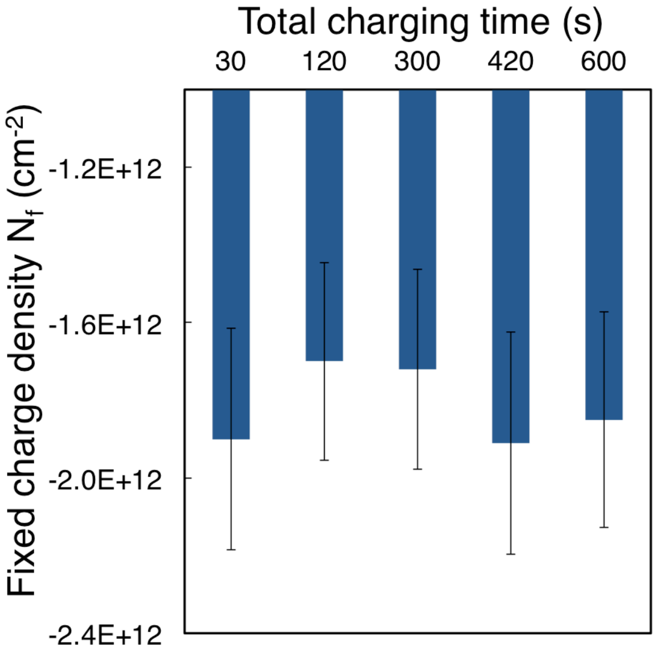

Fig. 5.5: Total charging time vs. fixed charge density N_f in the SiN_x film

TABLE 5.3: Effect of charging time on net charge density in the SiN_x film

Test#	Charging time	V_{FB}	N_f
	(s)	(V)	(cm^{-2})
1	30	9.4	-1.9×10^{12}
2	120	7.2	-1.7×10^{12}
3	300	7.8	-1.7×10^{12}
4	420	9.5	-1.9×10^{12}
5	600	8.9	-1.8×10^{12}

5.4 Effect of high energy UV radiation on nitride film charges

As previously mentioned in Chapter 3, it has been reported in the literature that illuminating SiN_x film with high energy (~ 4.9 eV) Ultra-Violet (UV) radiation increases the paramagnetic signal. UV radiation was found to annihilate all the charges present in the nitride film (K^+ or K^-) and convert them to neutral paramagnetic K^0 centers. The exact mechanism by which the UV radiation is able to neutralize the charge is still not clear. Williams [146] and Goodman [147] suggested that the incident high energy UV photons can create an electron - hole pair in the silicon substrate and these excited carriers with high energies can easily move from silicon into the silicon nitride film by crossing over the oxide barrier layer and neutralize the charges present in the nitride layer through a process known as photoemission. Photoemission can inject electrons from silicon substrate for any photons with energy higher than 4.3 eV and holes for photons having energy higher than 4.9 eV. However, it was later suggested by Crowder [106] and by Seager [107] that the sub-band gap absorption of UV light simply changes the spin and therefore, neutralizes the charge of the K center through a process known as photobleaching. UV illumination does not induce any chemical or structural change in the SiN_x film. In terms of K centers present in the nitride film, when illuminated by the high energy UV light, both the positively charged K^+ centers (with no spin) and the negatively charged K^- centers (with two spins) are converted to neutral K^o center defects (with one spin).

5.4.1 Charge neutralization by UV radiation

For this experiment, a high energy (4.9 eV, 254 nm) UV lamp was used to illuminate the nitride-oxide samples and measure its effect on the net charges present in the nitride film. A SiN_x-SiO_2-Si sample with ~ 80 nm SiN_x film deposited on a thermally grown ~ 20 nm SiO_2 film was measured with a Mercury (Hg) probe C-V tool. First C-V measurement taken on as-deposited N-O-Si sample gave a V_{FB} of -2.9 V indicating the presence of net positive charges (N_f = +3.3 x 10^{11} cm^{-2}) in the film, as shown in Fig. 5.6 and listed in Table 5.4. The sample was then treated with negative corona discharge and a second C-V measurement gave a V_{FB} of +17.2 V and a net negative fixed charge density N_f = -6.9 x 10^{12} cm^{-2} due to large negative charges injected in the film. As a final step, the sample was then illuminated with 254 nm (4.9 eV) UV light for 5 min and the C-V measurement was taken again. As seen from Fig. 5.6, the UV light neutralized all the negative charges present in the nitride film and the measured V_{FB} was -2.8 V giving approximately the same magnitude of positive charges as in the case of as-deposited film. These positive charges might be possibly located at the SiN_x- SiO_2 interface or in the underlying SiO_2 film itself. While corona charging technique gave the ability to inject either polarity of charges in the nitride film, illuminating the nitride film with high energy UV radiation, neutralized the injected charges. This ability to manipulate (inject-neutralize) the charges in the nitride film will be extremely beneficial for solar cell applications, where, on one hand, SiN_x films carrying a particular polarity of charges can be applied to either type of doped surfaces and on the other hand, UV illumination will allow controlling the magnitude of these injected charges depending on the substrate doping levels.

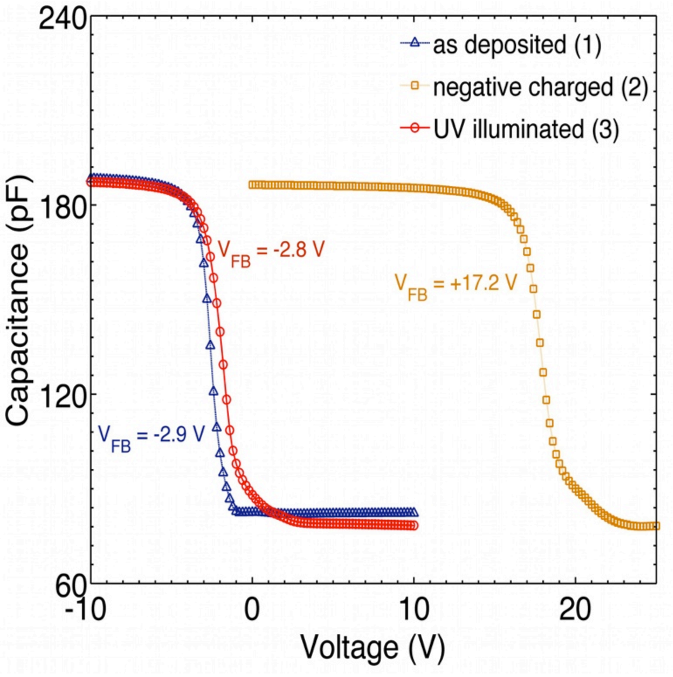

Fig. 5.6: CV plot - Effect of negative corona charging and subsequent UV illumination on net charge density of SiN_x film

TABLE 5.4: Effect of negative corona charging and subsequent UV illumination on net charge density of SiN_x film

Test#	Condition	V_{FB}	N_f
		(V)	(cm^{-2})
1	As deposited	-2.9	$+3.3 \times 10^{11}$
2	Negative corona charged	+17.2	-6.9×10^{12}
3	UV illuminated	-2.8	$+3.2 \times 10^{11}$

Moreover, such high energy UV radiation is not present in the global AM1.5 G solar radiation under which the solar cells are tested and operate [148]. As shown in Fig. 5.7, the solar radiation starts at ~ 290 nm translating to 4.3 eV and has significantly less energy than the energy of UV radiation (~ 4.9 eV) used in this work for charge neutralization. It will be shown in a later section that only 254 nm UV radiation is able to neutralize the charge and a higher wavelength (365 nm) UV radiation had no effect of the injected charge. Further, when the solar cells are connected in a module, a standard 3.2 mm thick PV glass is placed over the module with a typical transmissivity curve as shown in Fig. 5.7 [149]. The PV glass is able to transmit just 30% of the incident radiation at 300 nm. Therefore, once the samples are charged, the injected charge will remain present in the silicon nitride film for a longer period of time even under sunlight.

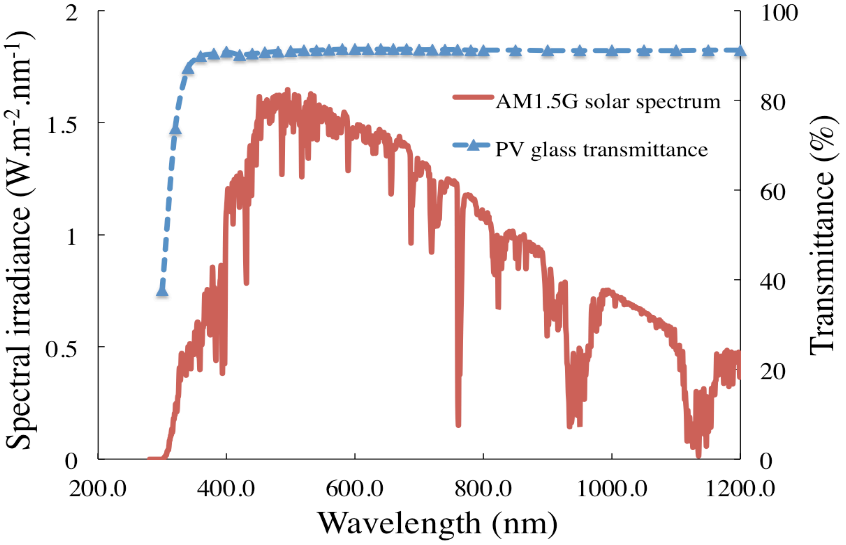

Fig. 5.7: AM1.5G spectrum and PV glass transmissivity

5.4.2 Increase in neutral paramagnetic K^0 defect density

ESR measurements were taken on SiN_x film samples to understand and quantify the effect of UV illumination on K center defect density present in the silicon nitride films. The samples used for this experiment were Si substrates with 1 μm thick SiN_x film deposited on both sides of the wafer. It was determined that at least 1 μm thick film is required to get a decent detectable ESR signal. As previously explained, specific silicon-nitrogen dangling bonds ($\cdot Si\equiv N$), known as K^o defects, are paramagnetic due to presence of one spin, and therefore, can be detected by ESR technique. The ESR signal is the first derivative of the absorbance of the incident electromagnetic radiation by the unpaired electron making a transition from the lower level to the upper level. The magnitude of the ESR signal is therefore, proportional to the total number of neutral K^o defects present in the sample.

First ESR measurements taken on samples with as deposited, untreated, PECVD SiN_x film confirmed the presence of neutral, paramagnetic K^O centers, as shown in Fig. 5.8. It is reported for the first time in this work that even as-deposited SiN_x film consists of neutral paramagnetic K^o centers. Krick and co-workers [99-101] have earlier reported that no paramagnetic signal and therefore, no K^o defects were detected in as-deposited SiN_x films; and these paramagnetic K^o defects in the nitride film were generated only after UV treatment of the film. Further, as seen in Fig. 5.8, illuminating the nitride film with 254 nm UV light for approximately 5 min nearly doubled the peak-to-peak amplitude of the ESR signal. As Table 5.5 lists, 1 μm thick SiN_x film deposited on both side of the Si sample prior to UV illumination had a spin density of 1.24×10^{13} spins / cm^2 (Test-1) that increased to 2.31×10^{13} spins / cm^2 after UV illumination (Test - 1A), directly implying that the increase in the number of total spins present in the film was due to 254 nm UV treatment of the SiN_x film. Similarly, another Si sample with 80 nm thick SiN_x film deposited on only one side of the sample was measured to carry a spin density of 1.2×10^{12} spins / cm^2 (Test 2) that increased to 1.34×10^{12} spins / cm^2 after the UV illumination (Test - 2A).

TABLE 5.5: ESR spin density of as-deposited and UV illuminated SiN_x film

Test#	Condition	Spin density (spins/cm²)
1	SiN_x 1 μm both sides (As deposited)	1.24×10^{13}
1-A	SiN_x 1 μm both sides (UV treatment)	2.31×10^{13}
2	SiN_x 80 nm single side (As deposited)	1.2×10^{12}
2-A	SiN_x 80 nm single side (UV treatment)	1.34×10^{12}

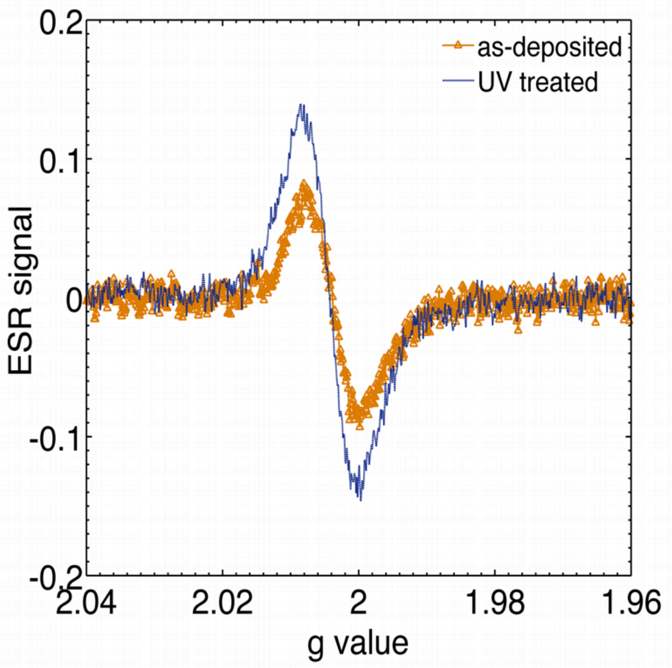

Fig. 5.8: ESR data: Effect of UV on 1 μm thick SiN_x film

This mechanism of increase in neutral K^0 defect center density can be better understood by visualizing the distribution of K center defects in the SiN_x films as shown in Fig. 5.9. Since, the K center defects arise from specific silicon-nitrogen dangling bonds $\cdot Si\equiv N$, the total density of these silicon-nitrogen dangling bonds in the SiN_x film remains constant. The K center defects can exist in three states: positively charged K^+ (no electron), negatively charged K^- (two electron) or neutral K^0 (one electron) defects.

Depending on the specific treatment (UV illumination, charging, annealing etc.) carried on the nitride film, the percentage of these individual charged K center defects: positively charged K^+, negatively charged K^- or the neutral K^o defects, change. The total K center density in the film remains constant after the treatments, but the change in individual K center defects can be detected by C-V and ESR measurements. While C-V measurements quantify the net charge (difference between positive and negative charged K defects) in the nitride film, ESR measurements quantify the total neutral defects (K^o) in the film that are paramagnetic. The positively charged K^+ or the negatively charged K^- defects are diamagnetic and therefore, do not give any ESR signal, whereas, neutral K^o defects being paramagnetic are detected by the ESR measurements. Therefore, as shown in Fig. 5.9, after illuminating the as-deposited SiN_x film with high energy UV radiation, the density of neutral paramagnetically active K^o defects increased whereas; the density of positively charged K^+ center defect and the negatively charged K^- center defect decreased.

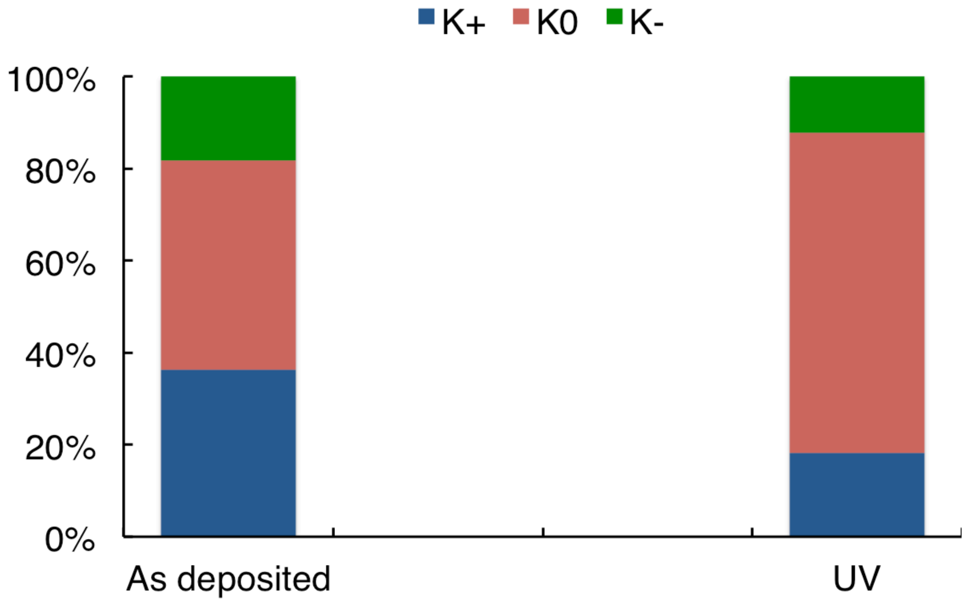

Fig.5.9: Visual representation of K center charge distribution in as-deposited and UV illuminated SiN_x film

5.4.3 Effect of charging on K center population

It was explained in the previous sections 5.2 and 5.3 using C-V measurements that the corona charging can inject either positive or negative charges in the silicon nitride film due to capture of holes or electrons by the K center defects present in the film. Eqs. 5.1 and 5.2 show how the paramagnetic signal seen in ESR measurements arising due to presence of paramagnetically active K^o centers decreases when these K^o centers capture an electron or a hole:

$$K^{o}(\uparrow) + e^{-} \rightarrow K^{-}(\uparrow\downarrow) \qquad 5.1$$

$$K^{o}(\uparrow) - e^{-} \rightarrow K^{+}() \qquad 5.2$$

The negatively charged K^- (↑↓) defects and positively charged K^+ () defects carry two electrons and zero electrons respectively and hence, are non-paramagnetic. Therefore, ESR measurements were taken on samples before and after charging to quantify approximate number of K center defects involved in the charging process and to further understand the behavior of K center defects.

First set of measurements was taken on SiN_x samples that were UV illuminated prior to corona charging (Fig. 5.10). As expected, UV illumination increased the magnitude of neutral paramagnetic K^o defects in the nitride film, evident by the increase in ESR signal strength, from 1.24 x 10^{13} spins / cm^2 (Test-1) to 2.31 x 10^{13} spins / cm^2 (Test-2), a rise of approximately 86%, as listed in Table 5.6. Further, after negative charging the UV treated sample (Test-3), a decrease in the ESR signal thus, indicated a decrease in the magnitude of K^o defects. It also showed an increase in the magnitude of negatively charged negatively charged K^- (↑↓) defects that are non-paramagnetic.

Following the negative corona charging, the number of spins present in the sample dropped approximately 40% from 2.31 x 10^{13} spins / cm^2 to 1.41 x 10^{13} spins / cm^2.

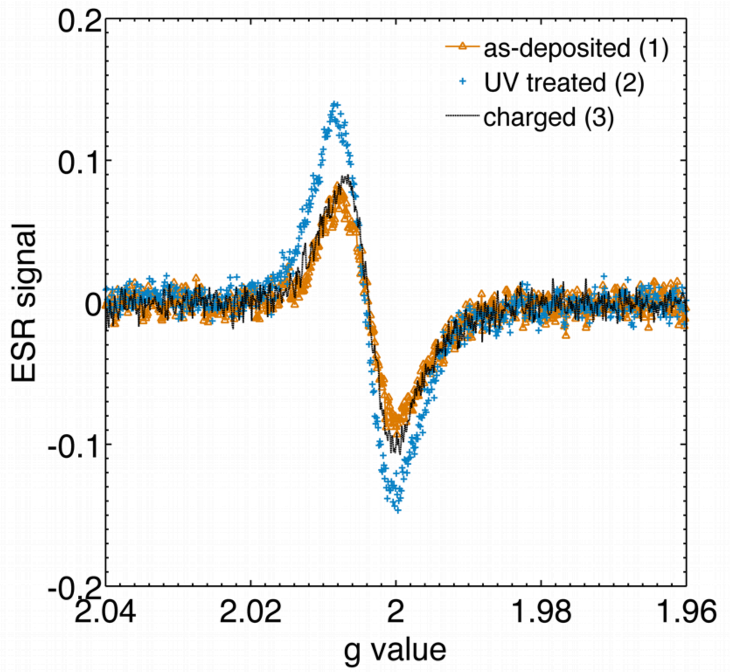

Fig. 5.10: ESR data: Effect of charging on K center density in SiN_x films

TABLE 5.6: ESR spin density of as-deposited, UV treated and negatively charged SiN_x film sample

Steps#	Condition	Spin density	Relative change
		(spins/cm^2)	(%)
1	As deposited film	1.24 x 10^{13}	N/A
2	After UV treatment	2.31 x 10^{13}	+86%
3	After negative charging	1.41 x 10^{13}	-40%

For the second set of measurements, the as-deposited nitride samples were first charged and then UV illuminated. In this case too, charging the samples decreased the magnitude of neutral paramagnetic K^0 defects present in the as-deposited film by approximately 50% from 5.11 x 10^{13} spins / cm^2 to 2.6 x 10^{13} spins / cm^2 as listed in Table 5.7. Further, following a 5 min UV illumination, the spin density in the sample increased from 2.6 x 10^{13} spins / cm^2 to 3.54 x 10^{13} spins / cm^2, an increase of approximately 35%.

TABLE 5.7: ESR spin density of as-deposited, negatively charged and UV treated SiN_x film sample

Steps#	Condition	Spin density	Relative change
		(spins/cm^2)	(%)
1	As deposited film	5.11 x 10^{13}	N/A
2	After negative charging	2.6 x 10^{13}	-49%
3	After UV treatment	3.54 x 10^{13}	+35%

Another mechanism through which the magnitude of individual charged K center defects change during charge injection process can be understood as follows: During the charge injection process, negative charging in this particular test, both the positively charged K^+ (no electron) defects as well as the neutral K^0 (one electron) defects can simultaneously capture the electrons as described by Eqs. 5.3 and 5.4. While, the first reaction step (Eq. 5.3) of electron capture by a positively charged K^+() defect increases the paramagnetic signal from the sample as it generates more neutral K^0 defect centers that are paramagnetic. On the other hand, the second step (Eq. 5.4) of electron capture by neutral K^0 defect decreases the paramagnetic signal as it creates diamagnetic K^- defect centers at the expense of K^0 defects. It is therefore, not possible to clearly distinguish between the two competing charge capturing events and thus, to determine the exact mechanism taking place behind the increase or decrease in the spin density of the sample.

$$K^{+}() + e^{-} \rightarrow K^{o}(\uparrow) \quad \textit{Paramagnetic} \qquad 5.3$$

$$K^{o}(\uparrow) + e^{-} \rightarrow K^{-}(\uparrow\downarrow) \quad \textit{Diamagnetic} \qquad 5.4$$

However, from both of the experiments described above, the ESR results still conclusively prove that the K center defects are the primary charge trapping defects present in the silicon nitride films that can capture both electrons and holes. While charge injection decreases the total number of spins (neutral K centers) present in the film, UV illumination increases the spin density by neutralizing the injected charge.

5.4.4 Time dependence of UV illumination on net charge in SiN_x film

To determine the amount of time required by the UV radiation to neutralize the net charge in the film, a nitride-oxide sample was subjected to UV illumination for certain duration of time. C-V measurements were taken at regular intervals to determine the flat- band voltage (V_{FB}) and fixed charge density (N_f) in the film. The fixed charge density in as-deposited SiN_x sample, prior to any UV treatment, was measured to be 2.9 x 10^{11} cm^{-2}. Next, the sample was subjected to negative charge injection treatment that resulted in a net charge density of -1.9 x 10^{12} cm^{-2} in the SiN_x film (Table 5.8). The sample was then treated with 254 nm UV light and the C-V measurements were taken. As shown in Fig. 5.11, just 15 s of UV exposure started decreasing the magnitude of the negative injected charge. Finally, after approximately 1 min of cumulative UV exposure, all the injected charge in the SiN_x film was neutralized and the measured V_{FB} of the sample was approximately equal to the as-deposited, pre-charged V_{FB}.

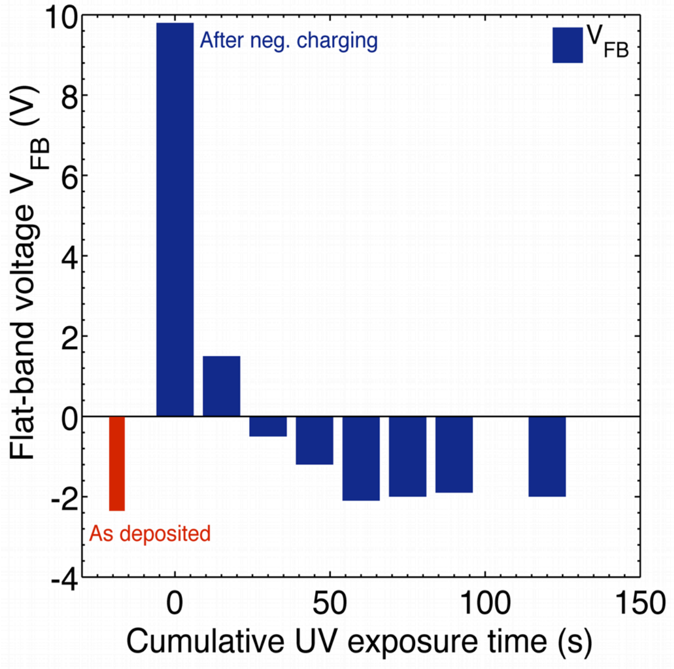

Fig. 5.11: Effect of UV exposure on net injected charge in the SiN_x film

TABLE 5.8: Effect of UV exposure on net injected charge in the SiN_x film

Test#	Condition	Flat-band voltage V_{FB}	Fixed charge density N_f
		(V)	(cm^{-2})
1	As deposited film	-2.1	2.9×10^{11}
2	After neg. charging	9.8	-1.9×10^{12}
3	After 15 s of UV exposure	1.5	-3.9×10^{11}
4	After 30 s	-0.5	-4.3×10^{9}
5	After 45 s	-1.2	1.3×10^{11}
6	After 60 s	-2.1	2.8×10^{11}
7	After 75 s	-2.0	2.7×10^{11}
8	After 90 s	-1.9	2.5×10^{11}
9	After 120 s	-2.0	2.7×10^{11}
10	After 180 s	-2.1	2.9×10^{11}
11	After 300 s	-2.1	2.9×10^{11}

5.4.5 Effect of UV illumination on SiN_x bond densities: FTIR measurements

To understand the role and effect of high energy UV radiation on SiN_x film's chemical bonds, FTIR measurements were taken at room temperature on SiN_x film samples. The aim of this experiment was to detect whether the neutralization of charges present in SiN_x film and the subsequent increase in the spin density after UV illumination was due to any hydrogen bond breaking or other bonding rearrangments taking place in the SiN_x film. Two samples were used for this experiment: (a) thermally grown ~ 20 nm SiO_2 film on CZ-Si substrate and (b) PECVD deposited SiN_x film (~ 80 nm) on CZ-Si substrate. It should be noted that there was no thermal oxide film between SiN_x and Si substrate for the second sample. CZ-Si substrates received standard cleans (RCA-B and BOE last) prior to SiO_2 or SiN_x deposition. FTIR measurements were taken on Thermo-Nicolet 6700 FTIR system at room temperature. 128 scans were recorded per sample for a higher signal to noise ratio with a resolution of 4 cm^{-1}. FTIR spectra were recorded on both samples (SiO_2/Si and SiN_x/Si) before and after UV illumination, and the difference in spectra (after illumination - before illumination) is given in Fig. 5.12.

As shown in Fig. 5.12, the FTIR spectra for both the samples show a strong absorbance peak at ~ 1106 cm^{-1}. No other noticeable peak is seen in the spectra for these samples. The negative going absorption peak at ~ 1106 cm^{-1} in the difference spectra suggests that the absorption peak at ~ 1106 cm^{-1} was smaller for the spectra taken after the UV illumination compared to the spectra taken before UV illumination for both the samples. Since, the absorption peak at ~ 1106 cm^{-1} is present in both SiO_2/ Si and SiN_x/ Si IR spectra, it is clear that the cause for this peak is independent of the film deposited on the silicon substrate.

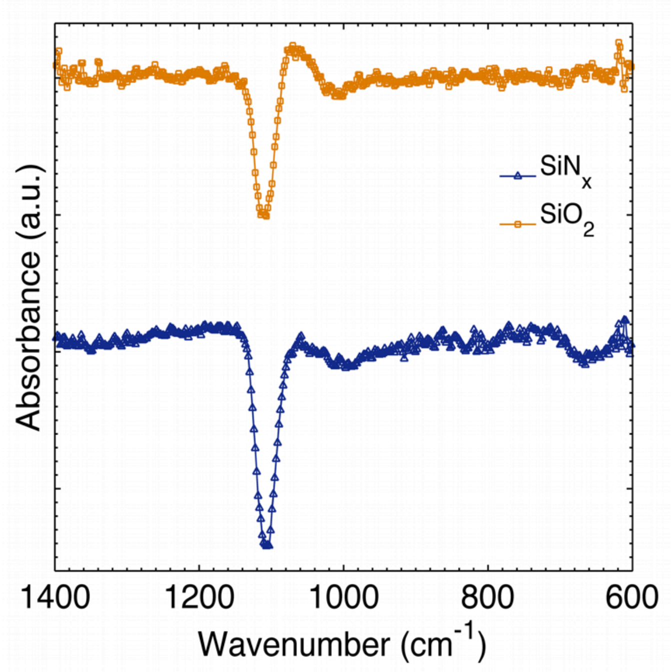

Fig. 5.12: FTIR spectra showing the effect of UV illumination on SiN$_x$/Si and SiO$_2$/Si samples

It has been well documented in the literature [150] that the interstitial oxygen present in the CZ-Si substrates due to quartz crucibles used during the CZ growth process of the silicon boules gives a strong absorption peak at ~ 1110 cm^{-1} (Fig. 5.13). Therefore, the negative absorption peak at ~ 1106 cm^{-1} seen for both SiO$_2$/Si and SiN$_x$/Si difference IR spectra is most probably due to the interstitial oxygen present in the underlying CZ-Si substrate. This change in absorption peak due to interstitial oxygen following UV illumination suggests that the UV treatment may have changed the concentration of interstitial oxygen atoms, possibly altering the Boron-Oxygen complexes present in the silicon substrates that are known to be light sensitive [151-153]. The difference in absorption might also be due to positional differences on the samples while taking FTIR measurements and the non-uniform distribution of interstitial oxygen concentration in the CZ-Si substrate.

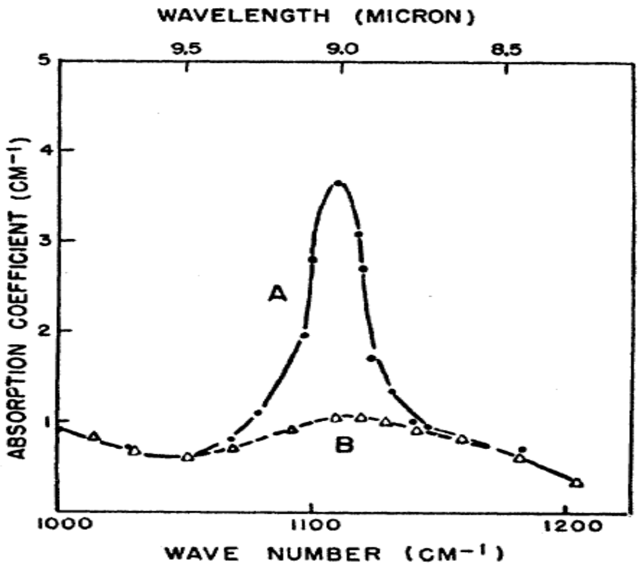

Fig. 5.13: Absorption coefficient of silicon at room temperature. A: pulled from quartz crucible, B: prepared from float-zone technique [150]

Coming back to the effect of UV illumination on bond density changes in the PECVD deposited SiN_x films, this experiment thus showed that the high energy UV illumination did not induce any changes in the bonding configuration [Si-H, N-H] in the SiN_x film. This further confirms that the charge neutralization and the increase in spin density in the SiN_x films seen after UV illumination is not related to any breaking of bonds or chemical rearrangements in the nitride film. Similar results were reported by Kanicki et al. [108] and by Seager [109] where the nitride films were subjected to long UV exposures and no effect was seen on the bond arrangements in the nitride film as a result of UV illumination. As it has been explained in the previous sections, charge neutralization in the nitride film takes place due to sub- band gap absorption of UV radiation in the SiN_x film that leads to optical rearrangement of charges. A negatively charged K^- center releases an electron upon illumination by UV light to become neutral paramagnetic K^o center as shown by Eqn. 5.5. This electron is then captured by a positively charge K^+ center to become another neutral K^o center (Eqn. 5.6). Therefore, UV radiation simply rearranges the spin on K center defects to increase the density of neutral K^o defect centers by decreasing the density of charged (K^+ or K^-) defect centers in the SiN_x film.

$$K^-(\uparrow\downarrow)+h\nu \rightarrow K^o(\uparrow)+e^- \qquad 5.5$$

$$K^+()+e^- \rightarrow K^o(\uparrow) \qquad 5.6$$

5.4.6 Effect of UV illumination on interface defect density D_{it}

It was important to investigate if the exposure to high energy UV illumination for charge neutralization step was damaging the interface between silicon-silicon oxide or silicon-silicon nitride film. Damage to the interface increases the interface defect density D_{it} ($cm^{-2}.eV^{-1}$), which in turn significantly increases the surface recombination velocity. Increase in the interface defect density D_{it} in the sample reduces the impact of field effect passivation brought by the surface charges and therefore, degrades the solar cell performance.

High frequency (HF) CV measurements are a quick and easy way to determine the presence and effect of D_{it}. As shown in Fig. 5.14, increasing in D_{it} in the sample stretches-out the HF CV curve along the gate voltage axis. For this work, HF CV measurements were taken on SiN-SiO-Si sample before and after UV illumination to qualitatively measure the impact of UV illumination on interface defect density. As seen in Fig. 5.15, no such spread-out of HF CV curve was noticed for samples before and after UV illumination.

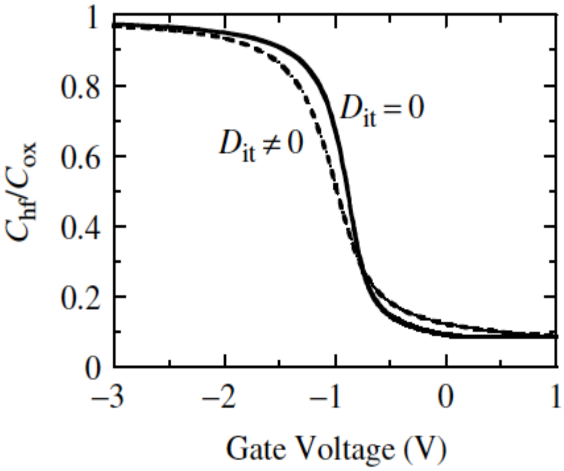

Fig. 5.14: Theoretical high frequency (HF) C-V curves for MOS-C showing the effect of D_{it} [18]

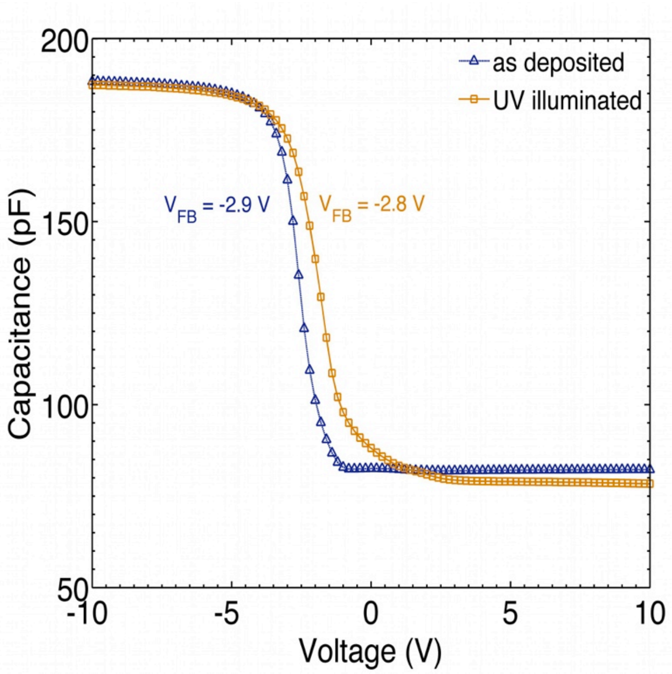

Fig. 5.15: High frequency C-V curves for SiN_x-SiO_2-Si sample before and after UV illumination to detect D_{it} effect

From these experiments involving UV treatment and charging of the nitride films, it was proved that there exists a finite population density of K centers in the

PECVD deposited solar-grade SiN_x films, existing in all three charged forms of positively charged K^+ centers (no electron), neutral K^o centers (one electron) and the negatively charged K^- centers (two electrons). While charge injection process increases the magnitude of charged K centers (K^+ or K^-) at the expense of neutral K^o defect centers, UV treatment of the SiN_x film neutralizes the injected charge and increases the magnitude of paramagnetically active K^o defects. A visual model of this change in individual K center defects after charging or UV treatment is shown in Fig. 5.16.

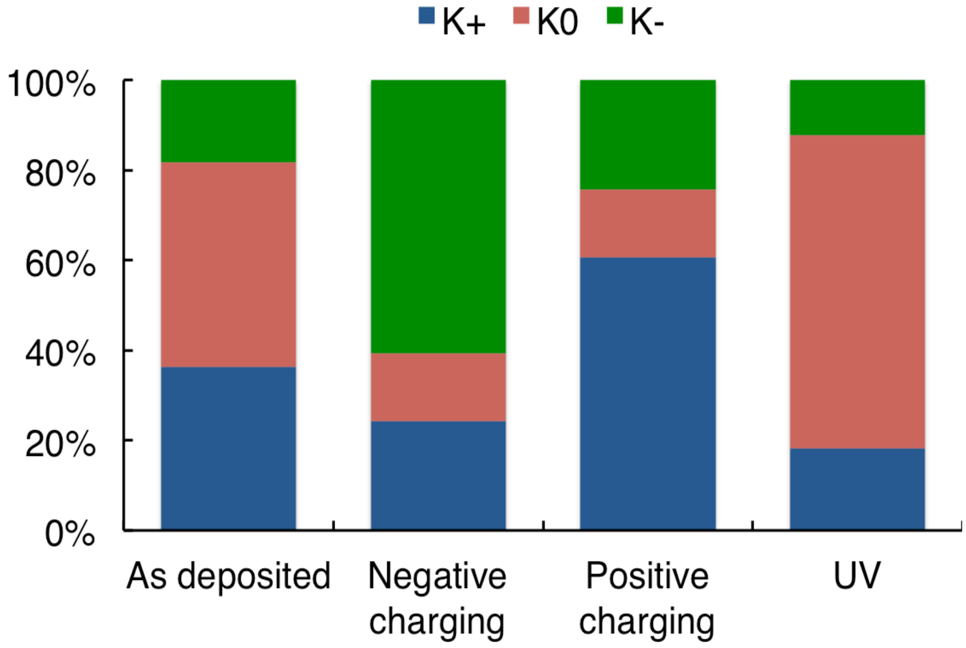

Fig. 5.16: Visual representation of K center charge distribution in as-deposited, negatively charged, positively charged and UV illuminated SiN_x film

Further, while C-V measurements can only determine the net charge present in the film depending on the relative magnitude of these three K center defects, ESR measurements can quantify the magnitude of neutral paramagnetic K^o defects. Depending upon the treatment of the SiN_x film, the density of each type of the defects can be changed easily and therefore, the net charge in the film can accordingly be manipulated. This ability to manipulate the charge in the silicon nitride film is of great technological importance particularly for the solar cell applications because it allows the silicon nitride films, carrying either positive or negative charges, to be applied to either n-doped or p-doped silicon surfaces respectively. The charge densities in the SiN_x film can be controlled in the right order of magnitude as required to accumulate varying levels of doped surfaces and thus, to minimize surface recombination as shown previously through PC1D simulations.

5.5 Distribution of K center defects in the SiN_x film

To determine the location and distribution of K center defects and associated charges in the SiN_x film, etch-back C-V and ESR measurements were taken on standard SiN_x film test samples. Etch-back C-V technique is the preferred method of determining the distribution of charge in the film with respect to the film thickness. C-V measurements are taken as the film thickness is gradually etched. The flat-band voltage (V_{FB}) when plotted against the film thickness gives an idea of the distribution as well as magnitude of charge in the bulk of the film. For this experiment ~ 160 nm thick PECVD SiN_x film was deposited on a ~ 20 nm of thermal SiO_2 film grown on CZ silicon substrate. Two set of experiments were carried out to determine the K center distribution - the first experiment involved etching the 160 nm thick SiN_x film into 7 samples with varying thicknesses and then negatively charging each one of the seven samples for an equal amount of time. For the second experiment, the 160 nm thick SiN_x film was first negatively charged, cleaved into 4 smaller samples and then each of these four charged samples were etched for different duration of time to achieve target thicknesses.

For the first set of experiment, the 160 nm thick SiN_x film was first etched into seven samples with varying thicknesses and each of these seven samples was then negatively charged in the corona charging tool for an equal amount of time to inject negative charges in the etched nitride film. C-V measurements were then taken on the seven samples and flat-band voltage (V_{FB}) and fixed charge density (N_f) was calculated for each of them as listed in Table 5.9 and shown in Fig. 5.17 and Fig. 5.18.

TABLE 5.9: Flat-band voltage (V_{FB}) and fixed charge density (N_f) measured after charging etched SiN_x samples

Test#	SiN_x film thickness	Flat-band voltage V_{FB}	Fixed charge density N_f
	(nm)	(V)	(cm^{-2})
1	13	0.7	-3.1×10^{11}
2	43	4.1	-1.0×10^{12}
3	65	6.8	-1.3×10^{12}
4	76	8.3	-1.8×10^{12}
5	99	11.5	-2.2×10^{12}
6	122	15.3	-2.9×10^{12}
7	155 (no etching)	20.2	-3.8×10^{12}

The purpose of this first set of experiment was to determine the location of the injected charge in the SiN_x film after subjecting the film to charge injection process. Depositing a thick nitride film, etching it into samples with varying thicknesses and then charging them, helped eliminate the run-to-run variation in as-deposited charges in the nitride film and therefore, gave a better idea of the distribution of charge in the bulk of the SiN_x film. As listed in Table 5.9, negative fixed charge density N_f was measured for all the SiN_x film samples with varying thicknesses. This clearly indicated that the K center defects, that are the primary charge trapping defects, are uniformly distributed in the SiN_x film. These uniformly distributed K centers were then converted to negatively charged K- centers after charging, and the negative injected charge was spread throughout the bulk of the SiN_x film and not just at the Si-SiN_x interface.

As the thickness of the SiN_x film increases, the flat-band voltage (V_{FB}) measured by the C-V technique increases quadratically. The V_{FB} is given by Eq. 5.7 as:

$$V_{FB} = \phi_{MS} - \frac{Q_f}{C_{ox}} - \frac{Q_{it}(\phi_s)}{C_{ox}} - \frac{1}{C_{ox}}\int^{t_{ox}} \frac{x}{t_{ox}}\rho_m(x)dx - \frac{1}{C_{ox}}\int^{t_{ox}} \frac{x}{t_{ox}}\rho_{ot}(x)dx \qquad 5.7$$

where, ρ(x) is the oxide charge per unit volume as a function of thickness. V_{FB} as a function of film thickness x can be written as Eq. 5.8, assuming all other charges to be constant.

$$V_{FB} = \frac{x^2}{2.t_{ox}.C_{ox}} \qquad 5.8$$

where, ρ_{ot} is the charge per unit volume uniformly distributed in the film. Therefore, the flat-band voltage (V_{FB}) scales as the square of the film thickness x as $V_{FB} = \frac{x^2}{2.t_{ox}.C_{ox}}$. Similarly, the fixed charge density N_f scales linearly with the film thickness x. Fig. 5.17 and Fig. 5.18 show the change in V_{FB} and N_f of the SiN_x film as a function of film thickness x.

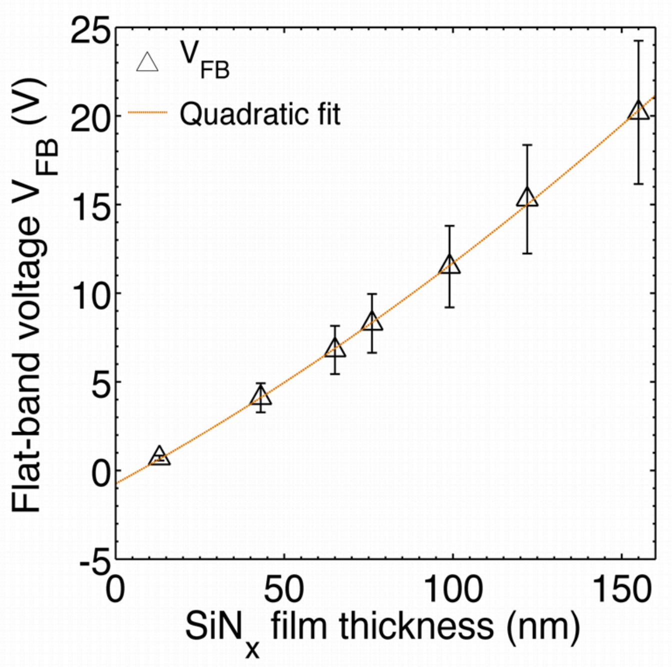

Fig. 5.17: Flat-band voltage (V_{FB}) as a function of SiN$_x$ film thickness measured after charging etched SiN$_x$ film samples

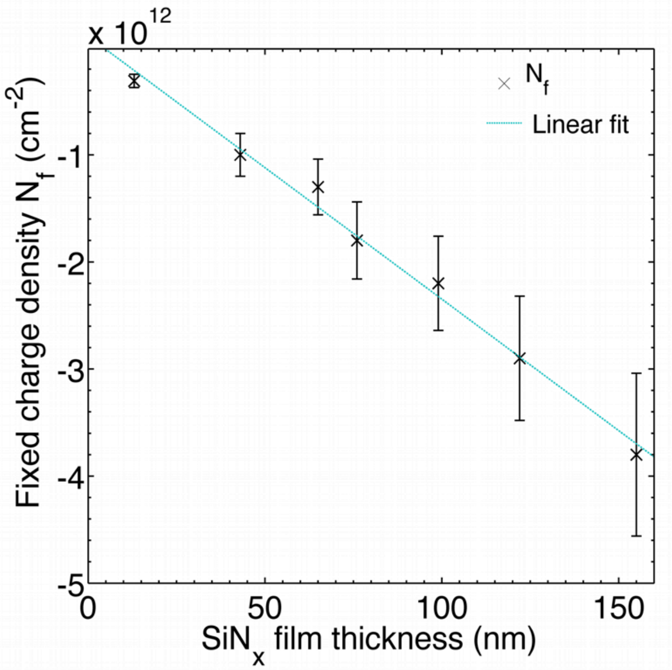

Fig. 5.18: Fixed charge density (N_f) as a function of SiN$_x$ film thickness measured after charging etched SiN$_x$ film samples

For the second set of experiment, a 160 nm thick SiN_x film was first deposited on a 6” round CZ Si substrate. The nitride film sample was then uniformly negatively charged in the corona discharge tool. After charging the nitride film for a certain time, the 6” round substrate was cleaved into four equal sized samples. The SiN_x film on these smaller samples was then etched to achieve different target thicknesses. The charged and etched samples were then measured using C-V technique to determine the magnitude of charge remaining in the SiN_x film. As listed in Table 5.10 and shown in Fig. 5.19, Fig. 5.20 and Fig. 5.21, as the nitride film was gradually etched, the flat-band voltage (V_{FB}) and the fixed charge density (N_f) of the samples also decreased. However, an important point to notice here is that the negative charge injected in the ~ 160 nm SiN_x film prior to etching was present even after etching the nitride film.

TABLE 5.10: Flat-band voltage (V_{FB}) and fixed charge density (N_f) measured after etching charged SiN_x samples

Test#	SiN_x film thickness	Flat-band voltage V_{FB}	Fixed charge density N_f
	(nm)	(V)	(cm^{-2})
1	81	4.6	-9.8×10^{11}
2	105	7.6	-1.4×10^{12}
3	124	10.8	-1.7×10^{12}
4	153 (no etching)	17.7	-2.2×10^{12}

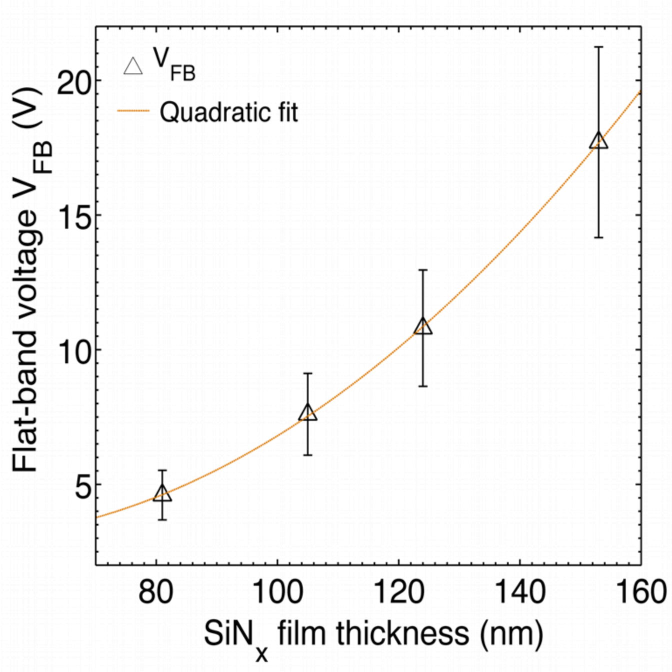

Fig. 5.19: Flat-band voltage (V_{FB}) as a function of SiN_x film thickness measured after etching charged SiN_x film samples

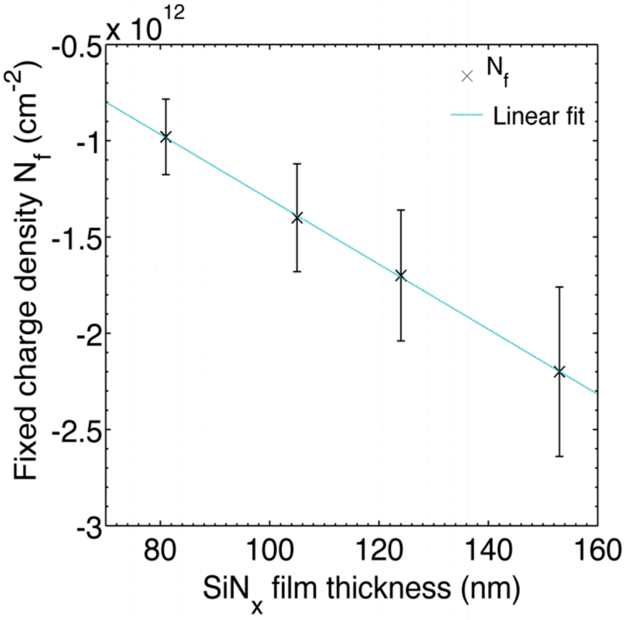

Fig. 5.20: Fixed charge density (N_f) as a function of SiN_x film thickness measured after etching charged SiN_x film samples

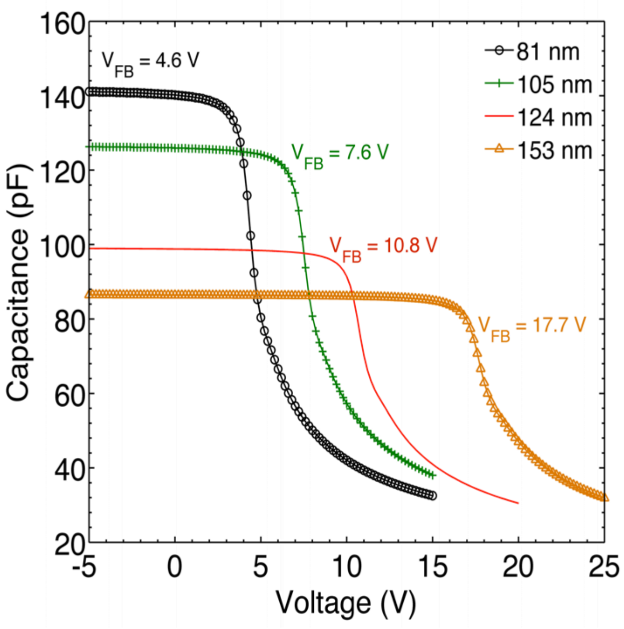

Fig. 5.21: C-V plot showing the variation in measured V_{FB} of SiN_x film samples that were first charged and then etched to get target thicknesses

Two important observations can be made from the second set of experiment. Firstly, the charge injected in the nitride film prior to etching using the corona discharge tool was distributed throughout the bulk of the film evident from the measured fixed charge density N_f values from the etched samples. This measurement further confirmed the fact that the K center defects originating from specific Si-N dangling bond are distributed evenly in the bulk of the nitride film during the film deposition. Secondly, etching the charged SiN_x film sample or rinsing it with DI water or IPA did not erase the charge present in the sample, further confirming that the injected charges are carried by the K center defects present in the bulk of the film and the charges thus, do not exist just as surface charges.

To further confirm the presence of K centers in the bulk of the SiN_x film, ESR measurements were taken on two samples: one with 80 nm of SiN_x film and second with 1 μm thick SiN_x film deposited on Si substrates. As shown in Fig. 5.22, the sample with 1 μm thick SiN_x film gave a significantly larger ESR signal compared to the sample with 80 nm thick SiN_x film. As explained previously, the peak-to-peak amplitude of the ESR signal is proportional to the density of neutral paramagnetic K^0 centers in the SiN_x film. As listed in Table 5.11, while the 80 nm thick SiN_x film sample had 1.2 x 10^{12} spins / cm^2, the 1 μm thick SiN_x film sample had 1.24 x 10^{13} spins / cm^2. These ESR results thus confirmed the fact that the K center defects that participate in the charge injection process are uniformly distributed in the bulk of the SiN_x films and the spin density increases as the thickness of the film increases. This directly implies that a thicker SiN_x film can carry a larger magnitude of injected charge (positive or negative) due to large number of K center defects present in the bulk of the thicker film.

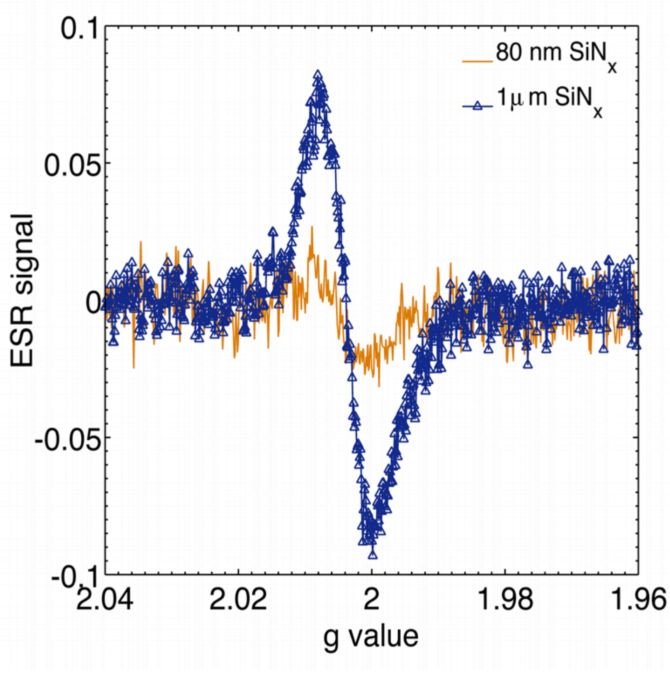

Fig. 5.22: ESR data: 80 nm vs. 1 μm thick SiN_x sample showing the distribution of K centers throughout the bulk of the SiN_x film

TABLE 5.11: ESR spin density of 80 nm thick and 1 μm thick SiN_x samples

Sample#	SiN_x film thickness	Spin density (spins/cm^2)
1	80 nm	1.2 x 10^1
2	1 μm	1.24 x 10^{13}

5.5.1 New model for charge distribution in SiN_x films

There are many different and often conflicting views described in the literature on the distribution and location of charges present in the silicon nitride films [90-93]. Later, Aberle [20, 65] also proposed that the measured positive charge in the SiN_x film is due to a constant contribution from an ultra-thin (< 2 nm) silicon oxynitride (SiO_xN_y) interfacial film along with the K^+ centers present in the SiN_x film (Fig. 5.23). According to this model, the thin native oxide film. During the initial SiN_x film deposition, the thiin native oxide layer, grown on the silicon substrates during the time elapsed between cleaning the substrate and prior to the deposition of silicon nitride in the PECVD tool, is converted to SiO_xN_y film that contributes to the net positive charges measured for the SiN_x films along with the K^+ centers distributed only up-to ~ 20 nm from the interface. This charge distribution model suggests that the as-deposited positive charges measured for the silicon nitride film are located only up-to ~20 nm from the interface within the SiN_x film.

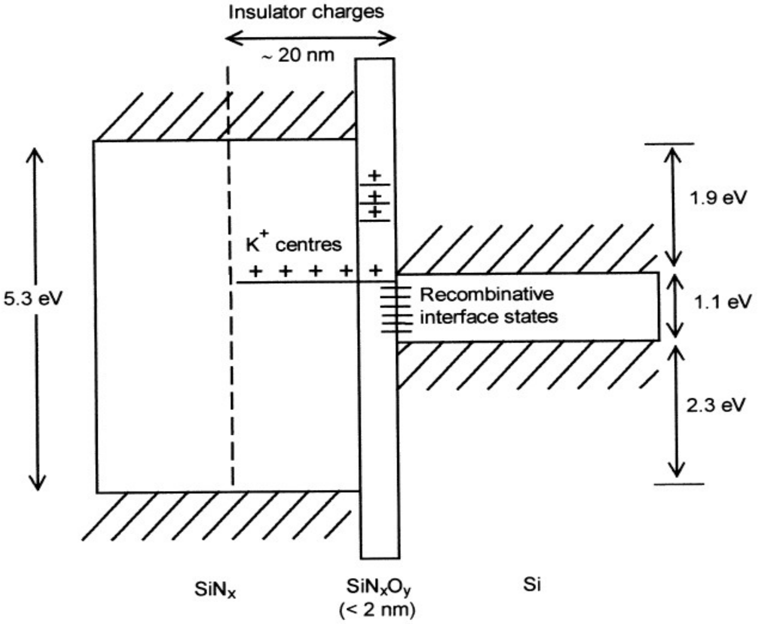

Fig. 5.23: Energy band diagram of the Si-SiN_x interface showing the distribution of positive insulator charge ($+Q_f$) up-to 20 nm in the SiN_x film [65]

However, as it was proved by the experiments involving etch-back SiN_x C-V measurements and ESR measurements that the K center defects are infact distributed throughout the bulk of the SiN_x film and not just near the interface. Further, it was also shown from charge injection experiments that the charge injected in the SiN_x film was also uniformly distributed in the bulk of nitride film and not just near the interface. The K center defects distributed uniformly in the bulk of the nitride film capture electrons or holes during charging process and thus give a net charge of the film. Therefore, as a result of this work, a new charge distribution model shown in Fig. 5.24 is proposed to enhance the understanding of K centers and associated charge distribution in the SiN_x films. It is proposed that the small (~ 5×10^{11} cm^{-2}) positive charge present in the as-deposited SiN_x films arises due to defects present at the SiN_x-Si interface and also due to few positively charged K^+ defect centers present in the SiN_x film. Further, the bulk of the nitride film consists of uniformly distributed K centers, the amphoteric charge trapping defects, that can exist in all three charged states: positive, negative or neutral. Since, the C-V measurements can only determine the net charge present in the film, it is not possible to exactly determine the exact density of the individual K center defects (positive, negative or neutral) present in the nitride film. ESR measurements, on the other hand, give an approximate density of neutral, paramagnetic K^o centers present in the nitride film that participate in the charge injection process. Still, when charge is injected in the nitride film through external means, this charge is uniformly distributed throughout the nitride film and not just near to the interface due to uniformly distributed K center defects.

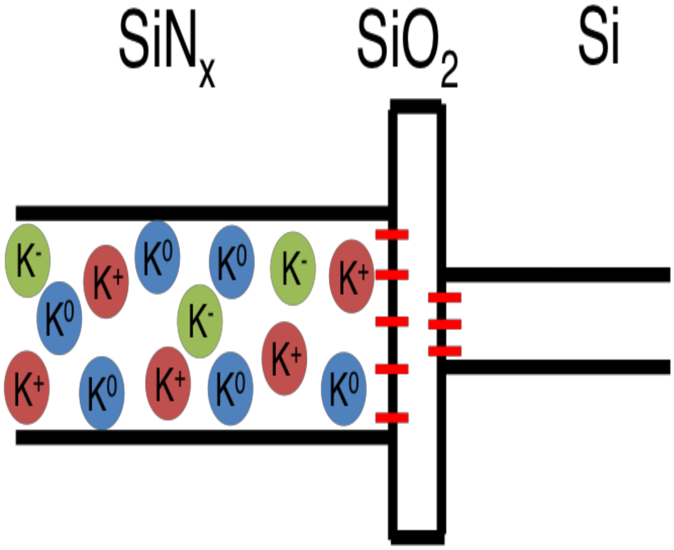

Fig. 5.24: New model for charge distribution in SiN_x films

5.6 Effect of high temperature treatments on injected charges and spin densities in the SiN_x film

The next sets of experiments were performed to understand the effects of high temperature annealing on the density of K centers present in the nitride film. This particular experiment involved annealing the PECVD deposited SiN_x film samples first to quantify the change in charge density and the K center density due to high temperature treatments. The annealed samples were then charged in the corona discharge tool to quantify any change in charge carrying capacity of the nitride film due to annealing. C-V and ESR measurements were taken to quantify the charge and spin densities present in the nitride film samples. One 6” round silicon substrate with 20 nm of thermal oxide grown underneath the 80 nm of standard PECVD silicon nitride film was used for this experiment. Four quarters were then cleaved out from the 6” round substrate: A) Control sample (no treatment), B) Belt-furnace fired sample, C) Forming Gas Anneal sample and D) Nitrogen anneal sample. The Forming Gas Anneal (FGA) sample received a FGA (N_2/ H_2) treatment at 400 °C for 20 min. Similarly, the Nitrogen anneal sample was annealed in N_2 ambient at 400 °C for 20 min. To simulate the effect of actual contact firing step in the solar cell fabrication process, the belt furnace sample was annealed at a peak temperature of 835 °C and the sample stayed underneath the high temperature zone approximately for 30 s. C-V measurements were taken on all the four samples at every step of the process: as-deposited condition, after annealing the samples and then after charging the samples. Similarly, for ESR measurements, 1 μm thick PECVD SiN_x film was deposited on both sides of another 6” round Si substrate and different samples were then cleaved out of it and received the same treatments of annealing and charging as of the C-V samples.

5.6.1 Effect of high temperature treatments on charge density: C-V results

For this first set of experiment, four samples were cleaved out of a 6” round SiN_x-SiO_2-Si sample as previously explained. These four samples were measured using C-V technique to determine the magnitude and polarity of charge present in the film before and after different annealing steps. While sample A served as a control sample, sample B was the belt furnace fired sample, sample C was FGA annealed and sample D was N_2

annealed sample. After annealing the samples, negative charge was injected in all the samples for equal time duration and C-V measurements were taken again.

TABLE 5.12: Flat-band voltage (V_{FB}) and fixed charge density (N_f) measured on 1) As deposited, 2) Annealed and 3) After charging annealed SiN_x samples

Sample	Condition	As-deposited		After annealing		After charging	
		V_{FB}	N_f	V_{FB}	N_f	V_{FB}	N_f
		(V)	(cm^{-2})	(V)	(cm^{-2})	(V)	(cm^{-2})
A	Control	-2.1	2.9×10^{11}	-1.9	2.4×10^{11}	6.4	-1.3×10^{12}
B	Belt furnace fired	-1.2	1.2×10^{11}	-1.3	1.3×10^{11}	9.0	-2.0×10^{12}
C	FGA	-1.1	1.1×10^{11}	-0.6	2.2×10^{10}	8.2	-1.8×10^{12}
D	N_2 annealed	-1.1	1.1×10^{11}	-0.8	4.4×10^{10}	8.9	-1.9×10^{12}

As listed in Table 5.12, different annealing steps slightly reduced the flat-band voltages (V_{FB}) of all the three samples (B, C and D) primarily due to hydrogen passivation of the dangling bonds and the charged K center defects present in the film. All the four samples were then subjected to negative charging treatment and then measured by C-V again. No trend was seen after negative charging of the samples and all four of them carried approximately equal magnitude of negative charge within the error of the measurements as shown in Fig. 5.25.

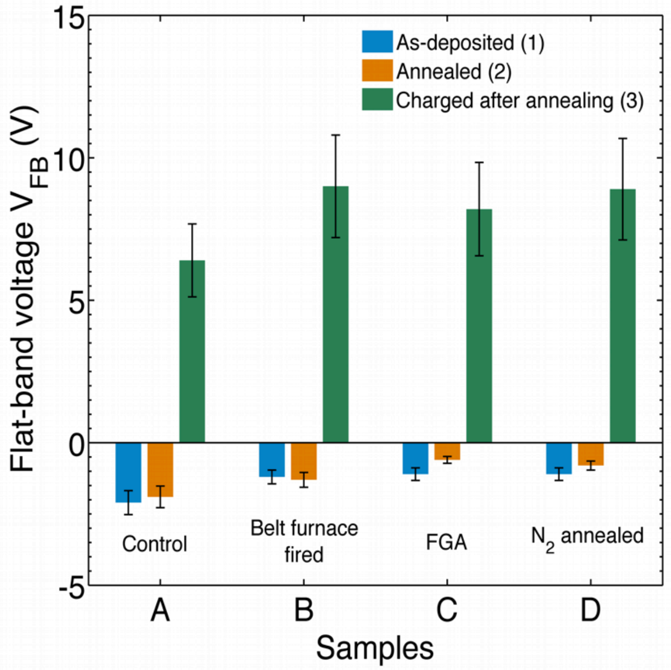

Fig. 5.25: Flat-band voltage (V_{FB}) measured on 1) As deposited, 2) Annealed and 3) After charging annealed SiN_x samples

5.6.2 Effect of high temperature treatments on spin density: ESR results

To further investigate the behavior of high temperature annealing steps on spin densities of SiN_x films, ESR measurements were taken on SiN_x samples to understand and quantify the effects of annealing and subsequent charge injection process on the density of K centers present in the nitride film. For ESR measurements, 1 μm thick PECVD SiN_x film was deposited on both sides of a 6” round Si substrate and four samples were then cleaved out of it. These four samples were: A) Control sample (no treatment), B) Belt-furnace fired sample, C) Forming Gas Anneal sample and D) Nitrogen anneal sample. All the four samples were measured by ESR technique before annealing, after annealing and then after charge injection step.

As seen in Table 5.13, all the three annealed samples (B, C, and D) show a decrease in the total spin density in the nitride film after high temperature annealing steps compared to the control sample A. For instance, the ESR signal for FGA annealed sample C was significantly smaller compared to the ESR signal for non-annealed control sample A as shown in Fig. 5.26. This decrease in the ESR signal directly related to a drastic reduction in the spin density present in Sample C, as much as 66%, compared to the spin density in Sample A. The reason for this reduction in the spin density (equivalent to the paramagnetic K^0 defect density) in the nitride film is due to the passivation of the silicon-nitrogen dangling bonds ($\cdot Si \equiv N$) by atomic hydrogen released by breakages of [Si-H] or [N-H] bonds due to high temperature steps.

TABLE 5.13: Relative change in the measured spin densities of the SiN_x film samples after various high temperature annealing steps

Sample	Condition	Spin density	Relative change w.r.t. Control sample A
		(Spins/cm^2)	(%)
A	Control	5.1×10^{13}	N/A
B	Belt furnace fired	4.6×10^{13}	- 9 %
C	FGA	1.7×10^{13}	- 66 %
D	N_2 annealed	3.1×10^{13}	- 40 %

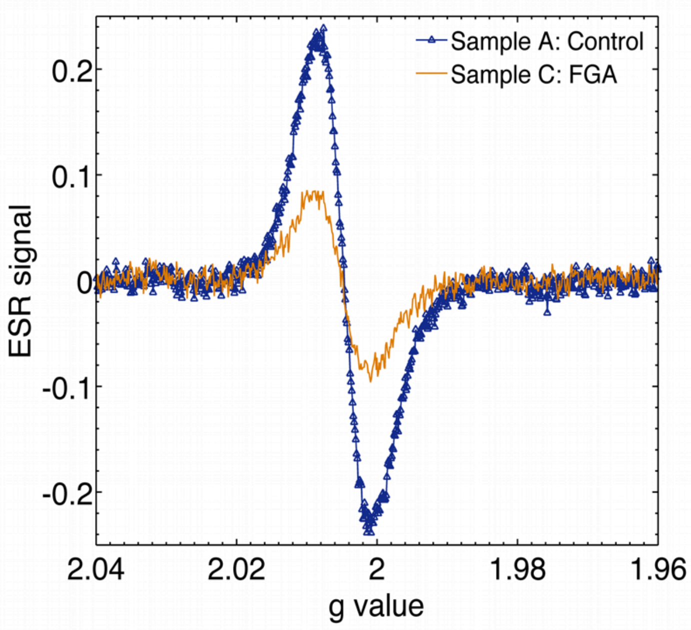

Fig. 5.26: ESR data: Effect of Forming gas anneal on spin densities of SiN_x film

After annealing, all four samples were negatively charged and measured with ESR technique again to quantify the change in spin densities due to charge injection process. Table 5.14 lists the spin densities measured on each of the four samples after charging and the relative change in spin densities due to charging process. As it has been previously explained in Sect. 5.4.3 that how the neutral and paramagnetic K^o defect centers present in the SiN_x film capture electrons or holes during charging process and become diamagnetic as given by Eqs. 5.9 and 5.10. This conversion of neutral, paramagnetic K^o defects in the SiN_x film to charged, diamagnetic K^+ or K^- defects shows up as a reduction in ESR signal that translates to a decreased spin density as shown in Fig. 5.27.

$$K^{o}(\uparrow)(Paramagnetic) + e^{-} \rightarrow K^{-}(\uparrow\downarrow)(Diamagnetic) \qquad 5.9$$

$$K^{o}(\uparrow)(Paramagnetic) - e^{-} \rightarrow K^{+}()(Diamagnetic) \qquad 5.10$$

TABLE 5.14: Relative change in the measured spin densities of the SiN_x film samples after charge injection process

Sample	Condition	Spin density (spins/cm^2)		Change due to charging
		Before charging	After charging	(%)
A	Control	5.1 x 10^{13}	2.6 x 10^{13}	- 49 %
B	Belt furnace fired	4.6 x 10^{13}	8.5 x 10^{12}	- 82 %
C	FGA	1.7 x 10^{13}	9.7 x 10^{12}	- 44 %
D	N_2 annealed	3.1 x 10^{13}	9.8 x 10^{12}	- 68 %

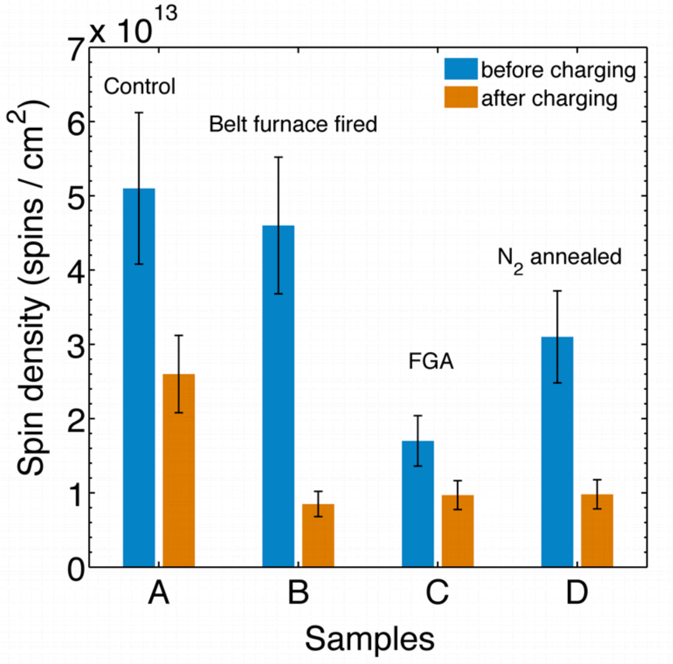

Fig. 5.27: Relative change in the measured spin densities of the SiN_x film samples after charge injection process

While on one hand, C-V measurements did not show any particular trend after charging the annealed samples; on the other hand, ESR measurements depicted a clearer picture of the effect of annealing and subsequent charging on the density of K center defects in the SiN_x film. Spin densities in the SiN_x film were significantly reduced as an effect of high temperature annealing steps and further reduced when the samples were charged. This behavior of K centers is useful to understand the effect of high temperature processing steps employed during solar cell fabrication on overall charge carrying capacity of the SiN_x films. As a result of annealing, the K center density in the SiN_x film decreases, which in turn limits the maximum charge density that can be carried by the SiN_x film.

5.7 Stability of injected charges in the SiN_x film

5.7.1 Long-term indoor stability

The next set of experiments involved determining the long-term stability of injected charges in the SiN_x films. For this experiment, two samples were cleaved out of a 6” round silicon substrate with 80 nm thick standard PECVD SiN_x film deposited on it. One sample was positively charged and the other was negatively charged in the corona charging tool. Flat band voltages V_{FB} and fixed charge densities N_f of both the samples were then measured using the C-V tool every month to determine the stability of the injected charge in the SiN_x film samples over a long duration of time. As shown in Table 5.15, both the samples showed no loss of injected charge (positive or negative) up-to 12 months after charging the samples. Both the samples were kept under normal indoor environment with standard room light and temperature conditions. The injected charge did not dissipate with exposures to the voltage sweeps during repeated measurements. This long term stability of externally injected charges in the standard solar grade SiN_x

film indicates that the injected charge is spread throughout the bulk of the nitride film, firmly held by the K center defects.

TABLE 5.15: Long term indoor stability of positive and negative injected charges in SiN_x film

Months	Positive charge injection		Negative charge injection	
	V_{FB}	N_f	V_{FB}	N_f
	(V)	(cm^{-2})	(V)	(cm^{-2})
0	-12.2	2.3×10^{12}	10.5	-2.2×10^{12}
1	-12.6	2.7×10^{12}	10.2	-2.0×10^{12}
2	-12.5	2.6×10^{12}	10.4	-2.2×10^{12}
3	-12.2	2.3×10^{12}	10.5	-2.2×10^{12}
4	-12.1	2.1×10^{12}	10.3	-2.1×10^{12}
5	-12.5	2.6×10^{12}	10.1	-2.0×10^{12}
6	-11.9	2.0×10^{12}	10.4	-2.2×10^{12}
7	-12.1	2.1×10^{12}	10.6	-2.3×10^{12}
8	-12.1	2.1×10^{12}	10.4	-2.2×10^{12}
9	-12.4	2.5×10^{12}	10.2	-2.0×10^{12}
10	-12.3	2.3×10^{12}	10.3	-2.1×10^{12}
11	-12.2	2.2×10^{12}	10.1	-2.0×10^{12}
12	-12.4	2.5×10^{12}	10.5	-2.2×10^{12}

5.7.2 Outdoor stability: Exposure to sunlight and heat

The next experiment to check the stability of injected charge was to expose the charge injected SiN_x film samples to direct sunlight and then to measure the magnitude of charge present in the film over a period of time. For this experiment, four samples A, B, C and D were cleaved out of a 6” round silicon substrate with 80 nm thick standard PECVD SiN_x film. Sample A served as the control sample and was not charged. Sample B was positively charged, whereas, samples C and D were negatively charged for equal duration in the charging tool. The flat-band voltages (V_{FB}) and fixed charge densities (N_f) were measured on these four samples using the C-V technique at three different steps: 1) as-deposited, prior to charging, 2) after respective charging treatments and 3) after 1 week of sunlight exposure.

TABLE 5.16: Flat-band voltage (V_{FB}) and fixed charge density (N_f) measured on charged SiN_x film samples to understand the effect of sunlight exposure

Sample	Condition	As-deposited		After charging		After 1 week of sunlight exposure	
		V_{FB}	N_f	V_{FB}	N_f	V_{FB}	N_f
		(V)	(cm^{-2})	(V)	(cm^{-2})	(V)	(cm^{-2})
A	Control	-2.7	3.7×10^{11}	-2.7	3.7×10^{11}	-2.5	3.1×10^{11}
B	Positive charged	-1.7	2.0×10^{11}	-13.0	2.3×10^{12}	-1.3	1.1×10^{11}
C	Negative charged	-1.1	1.1×10^{11}	10.0	-1.9×10^{12}	-3.0	4.1×10^{11}
D	Negative charged	-1.2	1.2×10^{11}	9.9	-1.8×10^{12}	-2.2	2.7×10^{11}

The 2nd column of Table 5.16 gives the magnitude and polarity of injected charges in samples B, C and D prior to sunlight exposure. The samples were then kept outside under direct sunlight for 1 week. The total insolation per day during one week of exposure was 6.2 kWh/m^2 with the peak daily ambient temperature of 38 ^oC. After first week of sunlight exposure, when the samples were measured again using C-V, the injected charge was no longer present in samples B, C and D. Positive injected charge in sample B and the negative injected charge in samples C and D got completely dissipated as listed in the 3rd column of Table 5.16. These results suggested that the injected charge that was stable over a year under controlled indoor conditions was not stable when exposed to real world conditions of sunlight or heat. From the previous experiments involving UV treatment of SiN_x films, it has been shown that the injected charges are neutralized only when exposed to 254 nm UV radiation. Therefore, it is possible that the injected charges in these samples that were subjected to sunlight were neutralized possibly due to the higher temperatures that the samples were subjected to and not due to the UV radiation present in the sunlight.

5.7.3 Thermal stability: Exposure to high temperature annealing treatments

To further understand the effect of temperature on the stability of injected charges in the SiN_x films, the next set of experiments was performed, where the charged SiN_x samples were subjected to high temperature annealing treatments. One 6” round silicon substrate with 20 nm of thermal oxide grown underneath the standard 80 nm of PECVD silicon nitride film was used for this experiment. Four quarters were then cleaved out from the 6” round substrate: A) Control sample (no treatment), B) Belt-furnace fired sample, C) Forming Gas Anneal sample and D) Nitrogen anneal sample. All four samples were subjected to charging process to inject negative charges in the SiN_x film prior to the high temperature treatments. C-V measurements were taken on all four samples at every step of the process: as-deposited condition, after negative charging of the samples and then after high temperature treatment step to quantify the remaining injected charge in the nitride film.

As seen from Table 5.17, the negative charging step injected approximately the same amount of negative charge in all four samples. However, when the samples B, C and D were subjected to respective high temperature steps, all the injected charge was completely wiped out. The control sample A was not annealed and therefore did not show any loss of charge. This experiment thus proved that the injected charge is unable to survive high temperature processing steps like FGA or contact firing steps. During high temperature processing, the extra electrons or holes captured by the K center defects of the SiN_x film, are relinquished and the sample shows loss of charge. Further, as shown by the previous experiments, ESR measurements also indicate that high temperature annealing is also responsible for the reduction of paramagnetic K center defects possibly due to hydrogen passivation of the dangling bonds in the nitride film.

TABLE 5.17: Flat-band voltage (V_{FB}) and fixed charge density (N_f) measured on 1) As deposited, 2) Negatively charged and 3) After annealing charged SiN_x samples

Sample	Condition	As-deposited		After charging		After annealing	
		V_{FB}	N_f	V_{FB}	N_f	V_{FB}	N_f
		(V)	(cm^{-2})	(V)	(cm^{-2})	(V)	(cm^{-2})
A	Control	-1.9	2.2×10^{11}	10.4	-2.1×10^{12}	10.5	-2.1×10^{12}
B	Belt furnace fired	-1.0	8.8×10^{10}	10.9	-2.2×10^{12}	-0.7	4.2×10^{10}
C	FGA	-1.2	1.2×10^{11}	10.0	-2.1×10^{12}	-0.9	6.2×10^{10}
D	N_2 annealed	-1.2	1.2×10^{11}	9.7	-1.7×10^{12}	-0.1	-8.4×10^{10}

Chapter 6

EFFECT OF SiN$_x$ CHARGE MANIPULATION ON SOLAR CELL PARAMETERS

6.1 Effect of SiN$_x$ charges on minority carrier lifetime

After understanding the properties of K center defects present in the SiN$_x$ films and having the ability to change the net charge of these K centers through corona charging and UV radiation, new set of experiments were conducted to further understand and quantify the effect of net charge present in SiN$_x$ films on minority carrier lifetime (τ_{eff}) of the silicon sample. As previously explained in Section 2.2, fixed charges present at the surfaces of the sample control the surface recombination through field effect passivation. If the bulk lifetime of the sample is large (for FZ Si sample τ_{bulk} ~ 5 - 10 ms) or if the samples are thin, the excess light generated carriers can have large diffusion lengths, allowing the carriers to diffuse to the surfaces of the samples. If the surfaces are accumulated or inverted by virtue of fixed dielectric charges, the recombination rate at the surfaces will be minimum and a higher τ_{eff} of the sample will be measured. However, if the surfaces are depleted and unpassivated, the carriers can now recombine through surface defects (D_{it}) and τ_{eff} will be drastically reduced. In this experiment, net charge present in the SiN$_x$ films deposited on both sides of either p or n-type FZ samples was manipulated by corona charging and UV radiation to understand and quantify its effect on minority carrier lifetime of the sample.

6.1.1 Role of thin oxide layer

For this experiment, a 475 μm thick, 100 Ω.cm, n-doped FZ Si sample coated with standard 78 nm PECVD thick SiN$_x$ film on both side was used as shown in Fig. 6.1. Minority carrier lifetime (τ_{eff}) was measured before and after various charging treatments using a Sinton WCT 120 lifetime tester tool at a specified minority carrier density of 1 x

10^{15} cm^{-3}. τ_{eff} of the as-deposited, pre-treatment sample was 1900 μs as shown in Fig. 6.2. The sample was then subjected to negative corona charging on both sides to inject negative charges in the SiN_x film. τ_{eff} was measured immediately after charging (time = 0 min) and then regularly up-to 5 hours (time = 300 min).

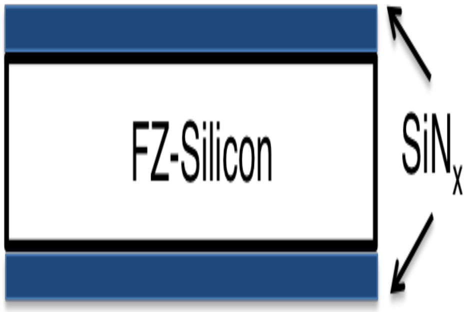

Fig. 6.1: Test structure to measure minority carrier lifetime (τ_{eff})

As shown in Fig. 6.2, immediately after negative charge injection, the minority carrier lifetime of the sample drastically reduced to 424 μs from the as-deposited carrier lifetime of 1900 μs. The reduction in τ_{eff} was due to enhanced recombination taking place at the surfaces that were depleted due to negative injected charge. However, as the time elapsed after charge injection treatment, the τ_{eff} of the sample gradually increased. The reason for this increase in the carrier lifetime was due to the lack of thin blocking oxide layer between the SiN_x film and the underlying Si substrate. Due to the absence of a thin oxide layer underneath it, the SiN_x film was unable to hold the injected charge. As a result of charge transition between the SiN_x film and the Si substrate, all the injected charge gradually dissipated or leaked. The surfaces that were depleted immediately after charge injection slowly accumulated again due to inherent positive charge present in the

SiN_x film and a higher τ_{eff}, approximately equal to the as-deposited case, was measured for the sample.

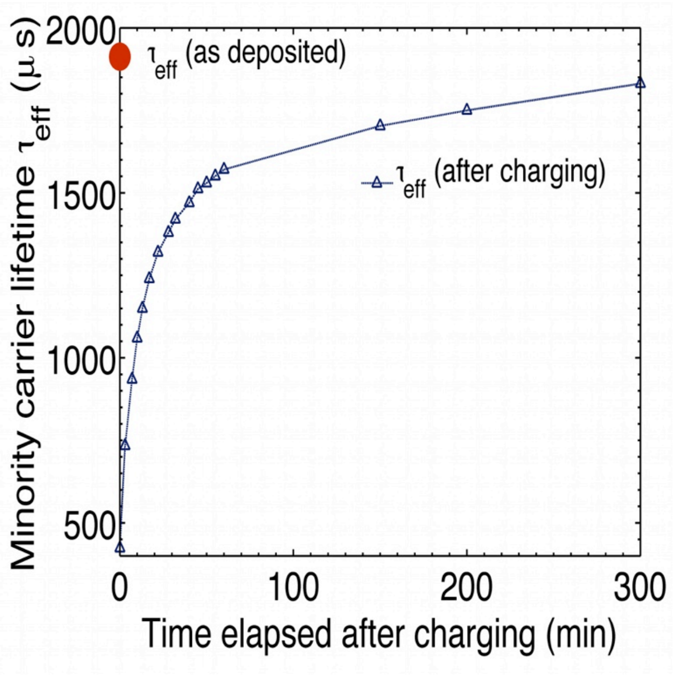

Fig. 6.2: Effect of charge injection in SiN_x film on minority carrier lifetime (τ_{eff})

The next sets of experiments were conducted on Si substrate that had a thin (~ 20 nm) of SiO_2 layer between the Si substrate and the SiN_x film to block the charge transition. Photoconductance as well as photoluminescence (PL) measurements were taken on test structures after injecting either polarity (negative and positive) of charges in the nitride film. Test structures to measure minority carrier lifetimes were p-doped, 480 μm thick FZ Si samples with 80 nm thick standard PECVD SiN_x film deposited on both sides. PL measurements along with lifetime measurements were also taken on the same samples after every charge injection treatment to further confirm the effect of injected charge on surface conditions. Table 6.1 and Fig. 6.3 show the effect of various charge manipulation treatments on minority carrier lifetime of the sample.

As-deposited pre-charged sample gave a minority carrier lifetime of 800 μs. When negative charges were injected in the SiN_x film, the minority carrier lifetime increased significantly to 2147 μs, giving an approximate effective surface recombination velocity (S_{eff}) of 11 cm/s. Negative charges on a p-doped Si sample accumulated the surfaces and reduced the surface recombination. The same sample when subjected to positive charge injection gave a minority carrier lifetime of 462 μs, equating to a S_{eff} value of 51 cm/s. This deterioration of minority carrier lifetime following positive charge injection was due to depletion / weak inversion of surfaces. In the end, the sample was illuminated with UV radiation and the measured τ_{eff} was just 84 μs equating to a S_{eff} of 285 cm/s. UV illumination annihilated all the charge, positive or negative, in the nitride film and the surfaces were nearly at flat-band, maximizing the surface recombination and reducing the minority carrier lifetime of the sample.

TABLE 6.1: Minority carrier lifetime τ_{eff} as a function of charge manipulation in SiN_x film

Test#	Process step	τ_{eff}	S_{eff}
		(μs)	(cm/s)
1	As deposited	800	30
2	Negative charging	2147	11
3	Positive charging	462	51
4	UV illumination	84	285

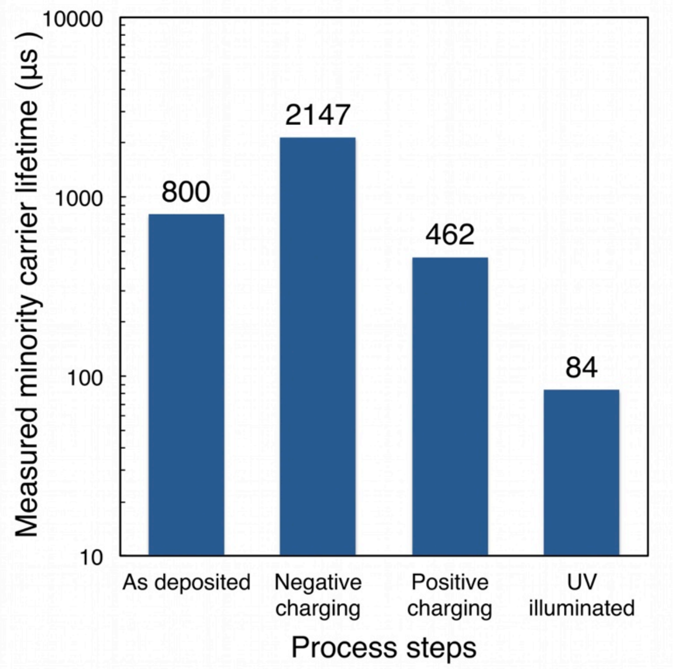

Fig. 6.3: Minority carrier lifetime τ_{eff} as a function of charge manipulation steps in SiN_x film

Photoluminescence (PL) measurement works on the principle of creating excess carriers in the bulk of the sample substrate through photo-generation and then capturing the radiative recombination events of these excess carriers through an Infrared camera. If the primary recombination mechanisms of these carriers generated in the sample are either due to defects present either in the bulk or at the surfaces (SRH recombination), the radiative recombination is significantly reduced and the image captured by the IR camera is dark. On the other hand, samples with higher bulk lifetimes and well passivated surfaces show up as a bright PL image.

For this experiment, PL images were taken on the p-FZ sample with SiN_x film deposited on both surfaces after negative or positive charge injection. When negative charges were injected in the nitride film, the surfaces were accumulated with majority holes present in the p-type FZ silicon sample and the S_{eff} decreased due to significant decrease in surface recombination activity. The PL image of the accumulated sample after negative charge injection as shown in Fig. 6.4 indicates that the surface recombination is dramatically reduced leading to a bright IR image. On the other hand, injecting positive charges in the same nitride film sample led to depletion and weak inversion conditions at the surfaces that increased the surface recombination and gave a darker PL image also shown in Fig. 6.4. Changing the net polarity of the fixed charge in the nitride film changed the surface conditions from accumulation to depletion/inversion that further led to changes in the surface passivation. This experiment thus proved that the net charge present in the SiN_x films can be manipulated to either polarity and their effect on surface passivation can then be easily measured using photoconductance and photoluminescence techniques.

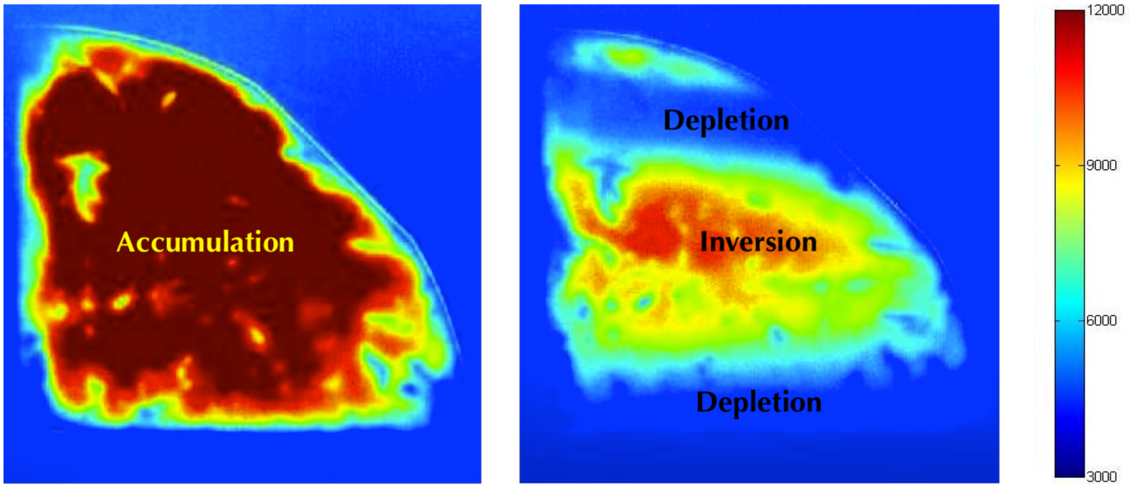

Fig. 6.4: Photoluminescence (PL) images taken on p-doped FZ Si substrate with SiN_x film deposited on both surfaces show accumulation (left) and inversion/depletion (right) conditions after injecting negative and positive charges respectively in the SiN_x film

6.1.2 Effect of UV radiation on minority carrier lifetime

The aim of the next set of experiments was to quantify the effect of annihilation of charges present in SiN_x films due to UV illumination by measuring the change in minority carrier lifetime τ_{eff} of the sample. As previously explained, high energy UV radiation can annihilate / neutralize the as-deposited or injected charges present in SiN_x films through a process known as Photobleaching [106, 107]. It was also shown in Section 5.4 through C-V measurements as how the UV illumination can neutralize the injected charge in the SiN_x films. Further, ESR measurements showed that UV illumination increases the density of neutral, paramagnetic K^0 defect center in the nitride film at the expense of positively charged K^+ or negatively charged K^- defect centers.

For this experiment, a 675 μm thick, 10-15 Ω.cm, DSP, p-FZ Si wafer was used. 78 nm thick standard PECVD SiN_x film was deposited on top of ~ 20 nm thick SiO_2 film on both sides of the wafer to create a test structure for minority carrier lifetime measurements. Two samples were then cleaved out of the wafer: Sample-1 for injecting negative charges and Sample-2 for injecting positive charges in the nitride film. Both the negatively charged and the positively charged samples were further divided in two smaller samples each, where one of the samples was subjected to 254 nm UV and the other sample was subjected to 365 nm UV radiation. Minority carrier lifetime τ_{eff} of the samples was measured at a specified carrier density of 1×10^{15} cm^{-3} immediately after charge injection and then regularly during the UV illumination process to measure the effect of UV illumination on surface charges and surface recombination.

Minority carrier lifetime τ_{eff} measured for Sample-1 immediately after negative charge injection was 384 μs, giving an approximate S_{eff} of 88 cm/s. The sample was then cleaved into two smaller samples: 1A and 1B. Sample 1A was illuminated with 254 nm UV light source and Sample 1B was illuminated with 365 nm UV light source. As shown in Fig. 6.5 and listed in Table 6.2, the τ_{eff} measured for Sample-1A, subjected to 254 nm UV radiation, quickly decreased and eventually stabilized at 85 μs after a cumulative UV exposure time of 600 s. On the other hand, τ_{eff} measured for Sample-1B, exposed to 365 nm UV light, did not show any change. The reason behind this behavior is primarily due to the different energies of photons from the two UV light sources. While on one hand, the 254 nm UV light with photons of energy ~ 4.9 eV was able to neutralize the injected negative charge in the SiN_x film, on the other hand, photons of ~ 3.4 eV energy present in the 365 nm UV light were not able to neutralize the charge. As 4.9 eV UV photons present in 254 nm UV gradually annihilated the injected charges, the surfaces of the p-doped Si sample that were under accumulation before UV illumination, eventually moved to depletion or flat-band conditions after UV exposure. The recombination at the depleted surfaces increased, thereby, decreasing the τ_{eff} of the sample. No such effect was noticed for 365 nm UV illumination on Sample-1B.

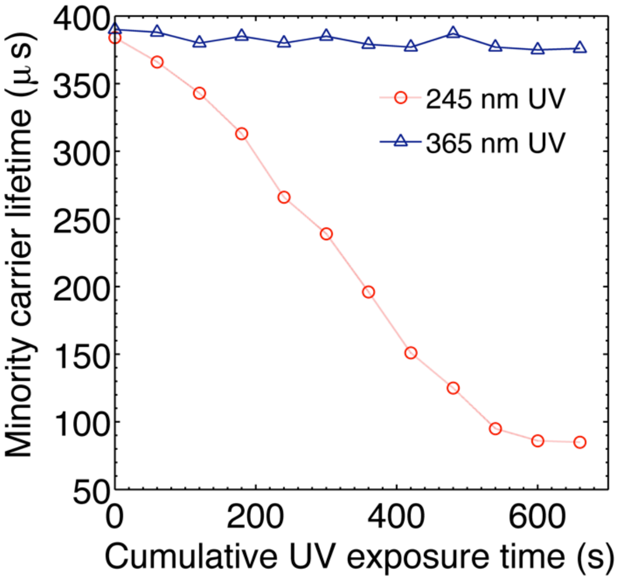

Fig. 6.5: Effect of UV exposure on minority carrier lifetime of p-FZ Si sample for negative charge injection in the SiN_x film

TABLE 6.2: Effect of UV exposure on τ_{eff} and S_{eff} of p-FZ Si sample for negative charge injection in the SiN_x film

Test#	Cumulative UV exposure time	245 nm UV		365 nm UV	
		τ_{eff}	S_{eff}	τ_{eff}	S_{eff}
	(s)	(μs)	(cm/s)	(μs)	(cm/s)
1	0	384	88.5	390	87.2
2	60	366	92.9	388	87.6
3	120	343	99.1	380	89.5
4	180	313	108.6	385	88.3
5	240	266	127.8	380	89.5
6	300	239	142.3	385	88.3
7	360	196	173.5	379	89.7
8	420	151	225.2	377	90.2
9	480	125	272.0	387	87.9
10	540	95	357.9	377	90.2
11	600	86	395.3	375	90.7
12	660	85	400.0	376	90.4

Similarly, positive charges were injected in the SiN_x film on Sample 2 cleaved out from the same original p-FZ wafer. The sample was then further cleaved in two smaller samples: Sample-2A subjected to 254 nm UV and Sample-2B subjected to 365 nm UV light and the carrier lifetime τ_{eff} in the sample was measured. In this case too, results similar to those measured on Samples-1A and 1B were observed, as shown in Fig. 6.6 and in Table 6.3. While 254 nm UV illumination annihilated the positive injected charges in Sample-2A and moved the surfaces of the sample from strong inversion to flat-band / depletion condition giving rise to higher surface recombination and lower τ_{eff}, 365 nm

UV radiation, on the other hand, had no such effect on the minority carrier lifetime of the Sample 2B.

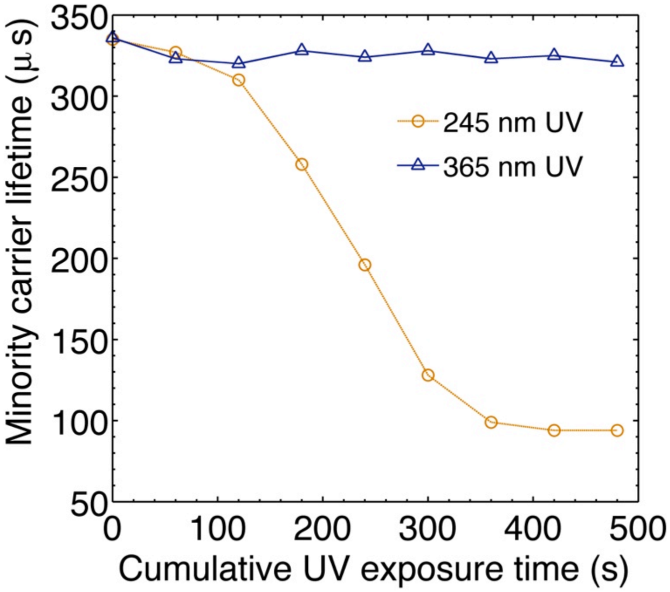

Fig. 6.6: Effect of UV exposure on minority carrier lifetime of p-FZ Si sample for positive charge injection in the SiN_x film

This experiment, therefore, showed that only specific very high-energy (~ 4.9 eV or higher) photons could neutralize or annihilate the charges injected in the SiN_x films and therefore, degrade the field effect passivation created by the injected charges. Lower energy photons, such as those present in 365 nm UV cannot neutralize the injected charge and will have no effect on the minority carrier lifetime of the sample. Further, as shown Section 5.4, such high energy photons (corresponding to 254 nm radiation) are absent in the AM 1.5 G solar spectrum. The PV glass covering the solar cells in the modules also blocks the high energy UV spectrum up-to 300 nm. Therefore, the charges (positive or negative) once injected in the SiN_x films should remain stable over a long duration of time when exposed to sunlight.

TABLE 6.3: Effect of UV exposure on τ_{eff} and S_{eff} of p-FZ Si sample for positive charge injection in the SiN_x film

Test#	Cumulative UV exposure time	245 nm UV		365 nm UV	
		τ_{eff}	S_{eff}	τ_{eff}	S_{eff}
	(s)	(μs)	(cm/s)	(μs)	(cm/s)
1	0	335	101.5	336	101.2
2	60	327	104.0	323	105.3
3	120	310	109.7	320	106.3
4	180	258	131.8	328	103.7
5	240	196	173.5	324	104.9
6	300	128	265.6	328	103.7
7	360	99	343.4	323	105.3
8	420	94	361.7	325	104.6
9	480	94	361.7	321	105.9

6.2 Charge assisted surface passivation on solar-grade CZ Si substrates

All the previous lifetime measurement experiments involving charge manipulation in the SiN_x films were conducted on thick (~ 480-680 μm), polished, FZ Si substrates. To integrate the SiN_x charge manipulation technique into standard silicon solar cell fabrication process, typical 180 μm thick, 156 mm x 156 mm, CZ, p- and n-doped, mono –Si substrates were used for this experiment. The aim of this experiment was to determine the effectiveness of externally injected charges in SiN_x film, deposited on cleaned and textured standard solar substrates, to minimize the surface recombination activity.

For this experiment, both p- and n-doped, solar grade CZ Si substrates were used. The p-doped CZ substrates were as-cut, 180 μm thick, Boron doped, 1-3 Ω.cm wafers, whereas, the n-doped Si substrates were 180 μm thick, Phosphorus doped, 1-5 Ω.cm wafers. Prior to charging treatments, all the samples went through standard texturing and cleaning processes. The samples were textured in KOH solution at 80 °C followed by RCA B and 10:1 BOE cleans. Once the substrates were textured and cleaned, 20 nm of SiO_2 followed by 80 nm of SiN_x was deposited on both sides of the Si substrates in the PECVD tool to create the lifetime measurement test structures. After deposition, the substrates were annealed in FGA at 400 °C for 20 min. Finally, the SiN_x film deposited on p-doped CZ Si sample was negatively charged and similarly, for n-doped CZ Si sample, the SiN_x film was positively charged using the corona charging tool. Minority carrier lifetimes (τ_{eff}) of both p-doped and n-doped samples were measured at various stages: 1) immediately after film deposition, 2) after FGA annealing and 3) after charging the SiN_x film to determine the effectiveness of charge assisted passivation on solar grade substrates. The carrier lifetime was measured in QSS mode at a specified minority carrier density of 1×10^{15} cm^{-3}.

Fig. 6.7 and Fig. 6.8 show the measured effective lifetime (τ_{eff}) of p-CZ and n-CZ Si samples respectively. As shown in Fig. 6.7, the as-deposited τ_{eff} measured for p-CZ sample was only 2.8 μs that improved to 33 μs after annealing the sample due to hydrogen passivation of the interface defects. However, after negative charging of the SiN_x film, the τ_{eff} further improved by over an order of magnitude to 252 μs, indicating very low surface recombination activity. Similar behavior was seen on n-CZ sample with positive charge injected in the SiN_x film (Table 6.4). This improvement in minority carrier lifetime of the samples after external charge injection in SiN_x films shows as how the charge induced field effect passivation plays a crucial role in improving the effective lifetime over chemical passivation, by inducing accumulation of majority carriers at the surfaces and thus minimizing the surface recombination. For the case of p-doped CZ Si sample, the measured τ_{eff} of 252 μs is almost equal to the bulk lifetime τ_{bulk} of the sample, implying that the surface recombination velocity was almost zero due to accumulation of carriers brought by externally injected charges in the SiN_x film.

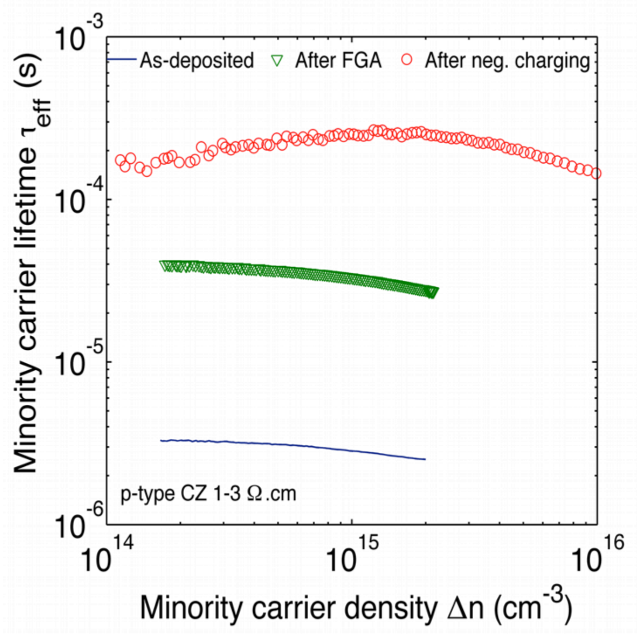

Fig. 6.7: Effective lifetime (τ_{eff}) vs. carrier density (Δn) for p-type CZ Si sample measured 1) after deposition, 2) after FGA anneal and 3) after negative charging of SiN_x film

TABLE 6.4: Effective lifetime (τ_{eff}), implied V_{OC}, and saturation current density J_o for p-type and n-type CZ Si samples measured 1) after deposition, 2) after FGA anneal and 3) after charging the SiN_x film

Test#	Condition	p-type CZ		n-type CZ	
		τ_{eff}	Implied V_{OC}	τ_{eff}	Implied V_{OC}
		(μs)	(mV)	(μs)	(mV)
1	As-deposited	2.8	542	2.5	520
2	FGA annealed	33	612	28	592
3	After SiN_x charge injection	252	677	379	664

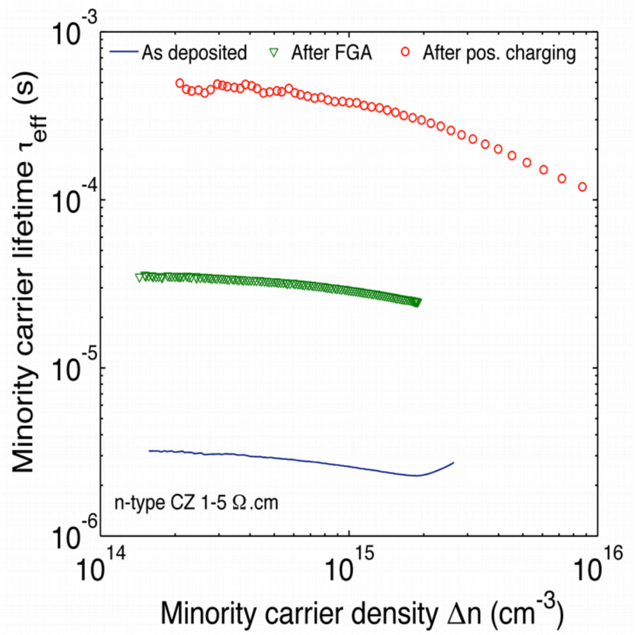

Fig. 6.8: Effective lifetime (τ_{eff}) vs. carrier density (Δn) for n-type CZ Si sample measured 1) after deposition, 2) after FGA anneal and 3) after positive charging of SiN_x film

Fig. 6.9 shows the photoluminescence (PL) images taken on the n-type CZ sample before and after positive charge injection in the SiN_x film. As seen from the PL images, injecting charges in the SiN_x films significantly improved the carrier lifetime in the Si substrate due to reduced surface recombination as a result of accumulation of majority carriers at the surfaces. Another important point to notice here is that the as-deposited SiN_x film is known to carry approximately 5 x 10^{11} cm^{-2} of positive fixed charges. However, those positive charges were not sufficient enough to induce strong accumulation of majority electrons at the surfaces in n-CZ Si sample and the measured carrier lifetime was low (~ 28 μs). After injecting a higher amount of positive charges through corona charging tool, the minority carrier lifetime improved by over an order of magnitude due to dramatic reduction of surface recombination brought by the positive injected charges in the SiN_x film.

Therefore, these experiments thus proved the effectiveness of charge injection process for minimizing surface recombination for standard p-type as well as n-type solar grade Si substrates. The improvement in carrier lifetime due to externally injected charges in the SiN_x film can significantly improve the overall cell performance.

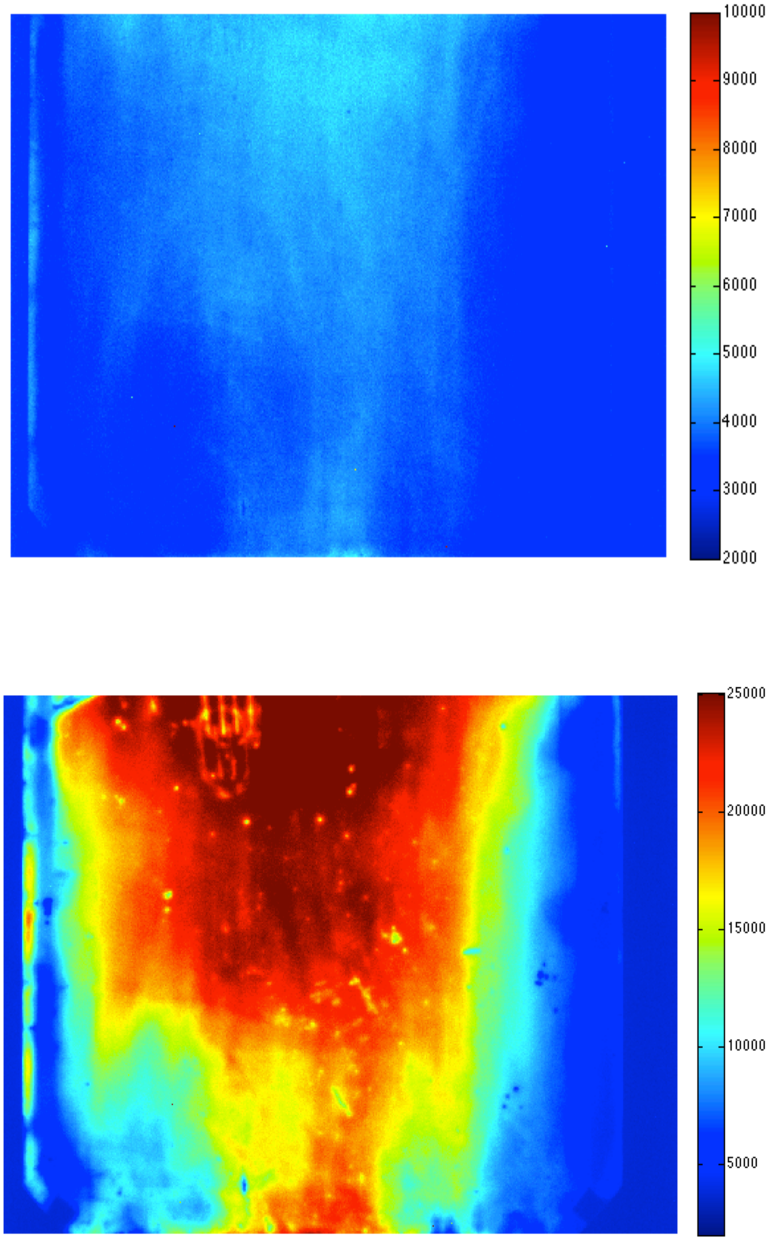

Fig. 6.9: Photoluminescence images taken on n-type CZ before (top) and after (bottom) positive charging of SiN_x film

Chapter 7

PERFORMANCE ANALYSIS OF 15 MW_P GRID CONNECTED DISTRIBUTED PV SYSTEMS INSTALLED AT ARIZONA STATE UNIVERSITY CAMPUS

7.1 Introduction

As the world population continues to increase above 7 billion, there is an ever-increasing demand for essential necessities like food, water and electricity. As the primary sources of fuel for the generation of electricity are coal and natural gas, this higher demand for electricity ultimately leads to increased green house gas (GHG) emissions (especially CO_2) into the environment. Electric Power Annual 2009 report [154] released by the US Energy Information Administration (EIA) states that about 69% of the total electricity generated in 2009 in the United States came from coal, petroleum, and natural gas fired power plants. This dependence on fossil fuels led to a total of 2.3 billion metric tons of CO_2 emissions in 2009 from both electricity generation and production of thermal output. The advantage of renewable electricity generation resources, especially Photovoltaic (PV) systems, over conventional power plants is that they do not emit CO_2 and other GHGs during operation. However, it is important to accurately measure the PV generated electricity to analyze and quantify the reductions in CO_2 emissions and peak load offset. The electricity load demand can be divided into baseline, intermediate and peak load. Traditionally, coal and nuclear power plants handle the baseline electricity loads and the quick response natural gas fired plants handle intermediate and peak demand loads. In some cases, a PV system's generation cycle matches that of a daytime peak electricity demand cycle i.e. the peak generation from a PV system coincides with the daily peak electricity load. Large scale grid connected PV power plants can offset the peak electricity demand by closely matched generation cycles and reduce the necessity of firing natural gas fired power plants.

Arizona State University (ASU) has added more than 15 MW_p of PV systems over the past two years on its campus buildings and parking structures, the majority of them at the Tempe campus [155]. As per the Carbon Neutrality Action Plan report [156] published by ASU in 2010, approximately 75% of the total 308,226 metric tons of CO_2 emissions from the university were due to electricity purchased from local utility companies generated from fuel sources such as coal, natural gas and nuclear. The aim of this work was to analyze the impact of PV generated electricity on the university's electricity demand and its ability to reduce the CO_2 emissions. The results from this study can help understand the bigger picture of how utility scale PV systems can reduce the dependence on gas or coal fired plants. In previous studies, data from a simulated PV system was used instead of real or actual measured electricity data to analyze the impact of PV generated electricity on peak demand reduction. Rahman and Kroposki [157] analyzed the demand side management applicability of three small-scale roof top PV arrays for a typical university building's peak load. Similarly, Denholm and Margolis [158] simulated the impact of large-scale PV generation, capable of generating up to 50% of the demand, on traditional electric power system's existing infrastructure.

We analyzed ASU's grid connected PV (15 MW_p) systems in terms of their capability to offset the peak electricity demand using real time data. We report the reduction in CO_2 emissions for a period of one year from the PV system generated electricity. Capacity factors of various PV systems were calculated to determine the effects of seasons, module technologies (crystalline silicon, thin film), tracking (fixed tilt, single axis tracking), and component failures on PV system performance. Further, we simulated one campus system using the System Advisor Model (SAM) to determine the variations in system's capacity factor due to different orientations (fixed, latitude tilt, tracking) and compared results with the real measured capacity factor of the system.

7.2 Methodology

The Campus Metabolism (CM) project at ASU monitors the real time energy usage and groups the data into different categories of heating, cooling, electricity used and electricity generated by PV systems. For most of the buildings, the electricity load does not include the cooling load as the building cooling is maintained by circulating chilled water from a central storage plant. The electricity data is available for individual buildings as well as for the entire campus for any particular period down to 15 min intervals. Meteorological data (solar radiation, ambient temperature, wind speed etc.) from a weather station located on campus is also available for the same time intervals.

7.3 Results and analyses

7.3.1 Peak load offset

We selected two separate scenarios to determine the peak electric load offset by the PV systems. For the first scenario, we analyzed the ability of a single PV system to offset the electricity demand (no cooling load) of a typical university building. For this purpose, we chose a 110 kW_p PV system installed on the roof of a classroom building. The electricity load from this particular building resembles a typical office building and is different from the other general set of residential halls, libraries or parking structures on campus. The peak electricity demand for residential halls or libraries occur during evenings and nights when the classes are over and therefore, such buildings do not show a typical weekday electricity demand curve that peaks during the afternoon and when the electricity generated from the PV system is highest. Fig. 7.1 shows electricity consumed (load), PV electricity generated and net (electricity consumed – PV electricity generated) curves on a typical workday for the classroom building. The demand for electricity gradually increased from 6 am and peaked during the afternoon hours. The close match between the electricity demand curve and the PV generated electricity flattened the demand peak. The electricity generated from the 110 kW_p PV system was able to offset about 50% of the peak electricity demand from 150 kWh to 70 kWh.

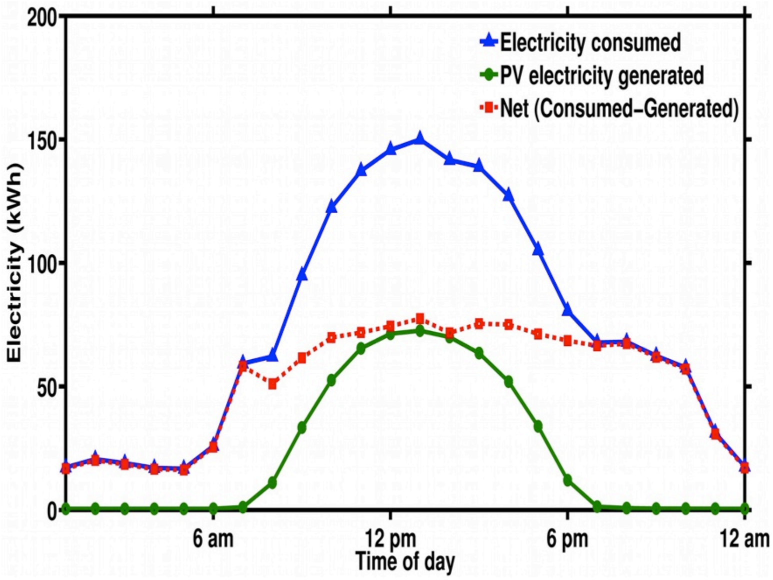

Fig. 7.1: Peak load shaving by a 110 kW_p PV system at a classroom building

For the second scenario of peak load offset, we measured the combined peak load offsetting by all the PV structures on the whole campus. The total electricity consumed for the campus was the summation of electricity used by the individual structures being monitored and recorded. Similarly, the total PV generation was the summation of electricity generated by all the PV systems on Tempe campus. We analyzed the electricity consumed and PV electricity generated for every hour on a weekend (Sunday) and weekday (Monday) for three different seasons.

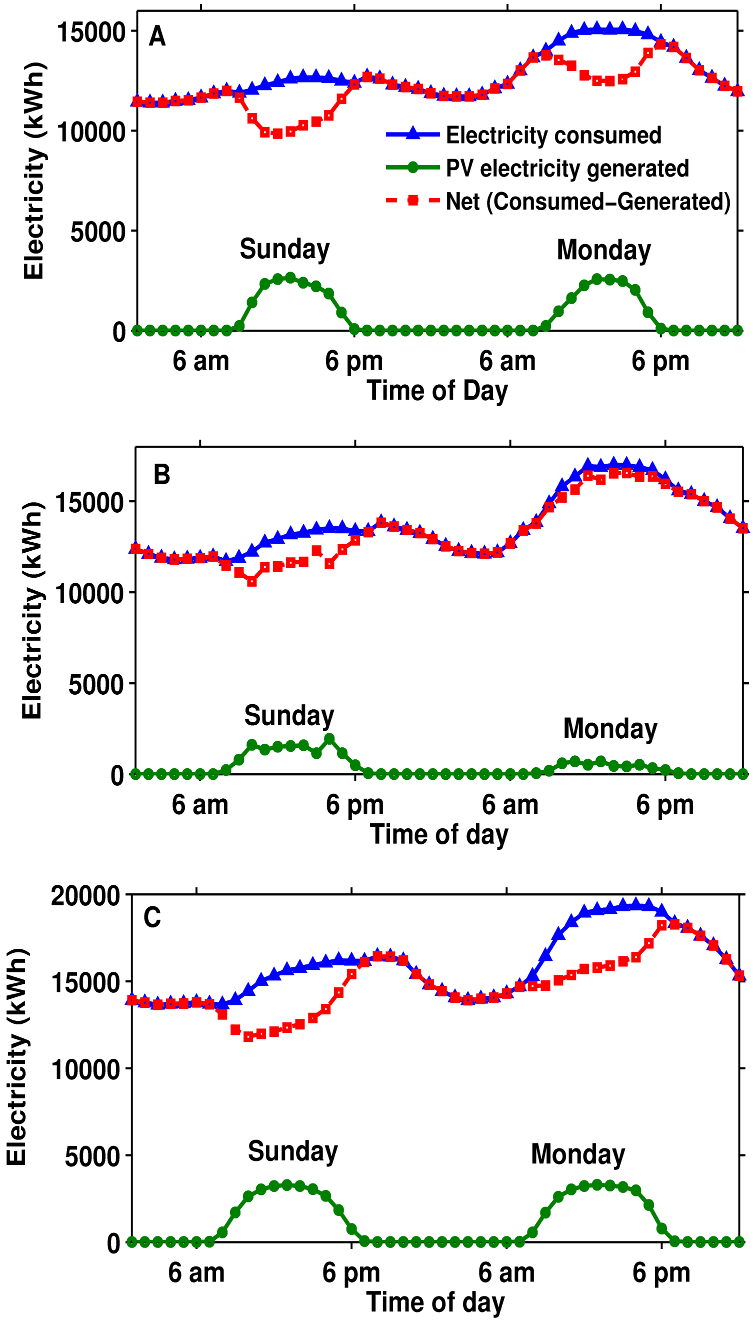

Fig. 7.2: Peak load shaving by total PV generated electricity at ASU's Tempe campus on a weekend and weekday for (a) winter (January), (b) rainy day (July) and (c) summer (August) season

As shown in Fig. 7.2, the total electricity consumed on campus was significantly higher on a workday during a week as compared to a weekend. Since the total PV generated electricity remains almost equal on Sunday and Monday, the PV systems were able to offset a higher percentage of the peak electricity consumed on campus on a weekend. In Fig. 7.2-a, the effect of PV electricity generation on the peak electricity demand load during winter season is shown. For the case of overcast skies and rainy days (Fig. 7.2-b), reduced electricity generation from the PV systems made them ineffective for load offset. However, rainy days are rare occurrences in Arizona during a calendar year and therefore, the PV systems effectively perform for more than 340 days per year. Fig. 7.2-c shows the peak load shaving during summer season. Both the electricity demand and PV electricity generation were higher in summer than in winter. A much lower peak now occurs in the late afternoon during both summer and winter. With the current installed capacity, the PV systems on campus are able to offset about 18-20% of the peak electricity demand for the campus.

7.3.2 Effect of dust storms

In 2011, Tempe and Phoenix metropolitan area witnessed occurrences of massive dust storms during the months of July to November. The largest dust storm on July 5th 2011 made headline news worldwide, limited the visibility to zero and coated every object in its way with a thick layer of dust (Fig. 7.3). We analyzed the effect of high profile dust storms, as distinct from long-term dust accumulation, on the performance of PV systems. Since the presence of dust reduces the amount of sunlight incident on the PV modules, the effect of dust storms on PV systems can be severely degrading.

Fig. 7.3: Exceptionally large dust storm in Phoenix on July 5th 2011 that reduced the visibility to zero and coated every object with a thick layer of dust (Image courtesy: Mike Olbinski)

A significant amount of research has been done in the past to understand and quantify the degradation of PV module output due to accumulation of dust. El – Shobokshy and Hussein [159-160] carried out systematic experiments to quantify the effects of five different kinds of dust on the output of PV cells. They emphasized three important parameters of dust namely, dust material, particle size and accumulated dust density (g/m^2) to accurately estimate the cell output losses. Zorilla – Casanova and co-workers [161] calculated the mean daily energy loss due to accumulated dust of flat plate PV collectors to be 4.4%. However, for long dry spells between rains, the losses can be even larger than 20%. They also found that intermittent rainfall, even less than 1 mm, is enough to clean the dust accumulated on the PV module and significantly reduce the soiling losses. Similar results were reported by Hammond et al. [162] on the performance degradation by accumulated dust on radiometers and fixed tilt, single and double axis tracking systems. They also reported that the output power of modules regularly recovered to with 1% of the rated power after slight intermittent rain (~ 5 mm). However, it is still suggested that the fixed tilt system be cleaned frequently for cost benefits. Mani and Pillai [163] have summarized past research on the impact of dust on module performance. They point to few areas, for example, properties of natural dust, geographic location, wind direction, system tilt among others that still need to be explored to clearly understand the impact of dust. Dust storms in Arizona result due to strong monsoon winds particularly during June – September. These dust storms are usually followed by strong thunderstorms and brief periods of rain.

For our analysis, we chose two different PV systems (20° fixed tilt) installed on campus buildings (Building A and B) for the period of July 3rd to July 12th, 2011. The modules were relatively clean after a small thunderstorm and rain on May 18th, 2011 prior to the July 5th dust storm. We calculated the change in system efficiency by dividing the daily AC electricity output (kWh) by the product of irradiance (kWh/m^2) and total module area (m^2).

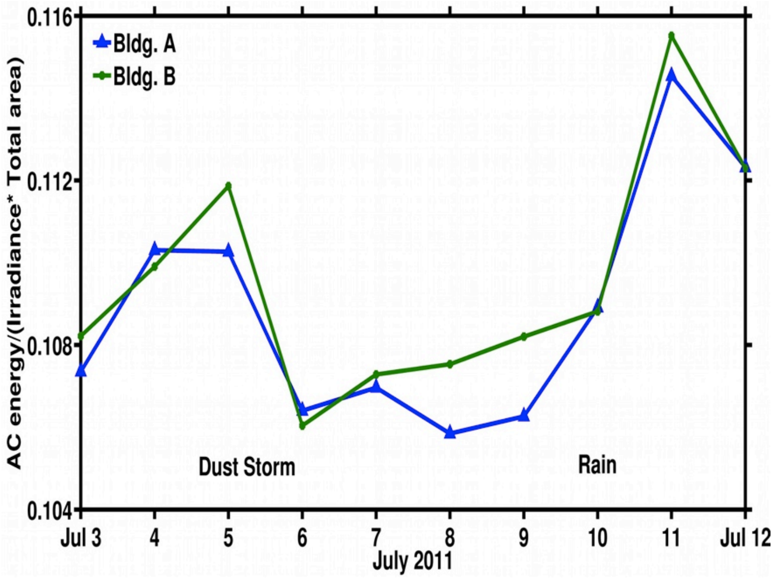

Fig. 7.4: Effect of dust storm (July 5, 2011) and rain (July 10, 2011) on the performance of two PV systems

Fig. 7.4 shows that the performance of the systems dropped approximately by 4-5% absolute on the day after of the dust storm (July 6th). The dust from Phoenix area storm is typically a fine dry material that can be quite thick but does not adhere well and therefore, can be easily removed by wind or rain [164]. The dust storm was followed by a light rain (less than 5 mm) on the night of July 10th that cleaned off the accumulated dust on the modules. As expected, both the systems gave higher performances on July 11th (Fig. 7.4).

To verify that the performance degradation was only due to the dust storms and not from the variations in temperature, we compared the performance ratio (PR) of one of the PV system with back of the module temperature for the same time period. Performance ratio, given by Eq. 7.1, is a metric to quantify overall effect of losses on a system's rated output. The losses can be due to irradiance, component failures, system downtime, module mismatch or soiling.

$$Performance\ Ratio\,(PR) = \frac{\dfrac{net\ system\ energy\ output\,(kWh)}{rated\ system\ DC\ capacity\,(kW)}}{\dfrac{total\ in-plane\ irradiance\,(kWh/m^2)}{reference\ irradiance\,(1kWh/m^2)}} \qquad 7.1$$

As shown in Fig. 7.5, the module temperature over the period of analysis did not show large variations to bring the noticed drop in the performance of the PV system on July 6th. Further, it is also clear that the small amount of rain on July 10th was enough to clear off the dust and bring up the system performance again.

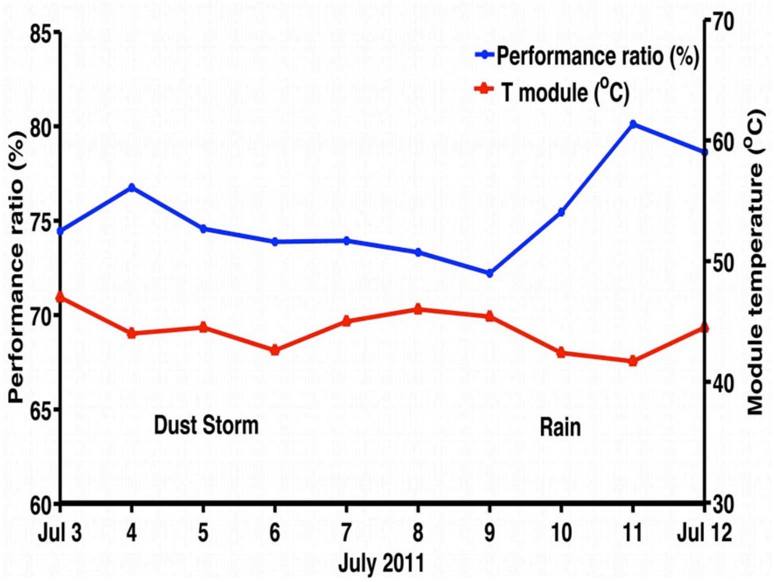

Fig. 7.5: Variations in performance ratio (left axis) and module temperature (right axis) of a PV system during July 3-12, 2011

7.3.3 Approximate yearly reductions in CO_2 emissions

In order to determine the potential impact of this large scale PV installation on the environment, we calculated the approximate yearly reduction in CO_2 emissions due to the PV generated electricity. The total PV generated electricity from all the systems installed at Tempe campus over a period of 1 year (July 1st 2011 – June 30th 2012) was 13.13×10^6 kWh. The Emissions & Generation Resource Integrated Database (eGRID) U.S. total annual CO^2 equivalent output emission rate for 2009 [165] was used to convert PV generated kilowatt-hours into equivalent carbon dioxide emissions units. The US annual total CO^2 emission rate is 5.543×10^{-4} metric tons of CO_2/kWh. The total CO_2 emission rate for the local sub-region AZNM (Arizona New-Mexico) grid is 5.425×10^{-4} metric tons of CO_2/kWh, which is nearly the same as the US annual total CO2 emission rate. Multiplying the total annual PV generated electricity (13.13×10^6 kWh) with the US annual total CO_2 emission rate gives approximately 7300 metric tons of equivalent CO_2 emissions that were reduced over the year.

7.3.4 Capacity factors

PV systems are also compared with other electricity generation systems in terms of capacity factors. Capacity factor for a system of a certain size is defined as the ratio of total energy produced by the system over a period of time to the energy it could have produced running continuously over that period of time at its rated capacity. A report [166] published by National Renewable Energy Laboratory (NREL) estimates the capacity factors for a typical nuclear, coal and PV power plants as approximately 90%, 85% and 22% respectively. To get a better idea for the differences in capacity factors of diverse electricity generation sources, we calculated the monthly capacity factors for the Palo Verde nuclear power plant for a period of one year (Jan 1st 2010 - Dec 31st 2010) as shown in Fig. 7.6. The Palo Verde nuclear power plant located about 50 miles West of Phoenix, AZ is the largest nuclear power plant in the United States rated at 3942 MW. The average capacity factor for this nuclear power plant for the year 2010 was 90.4%.

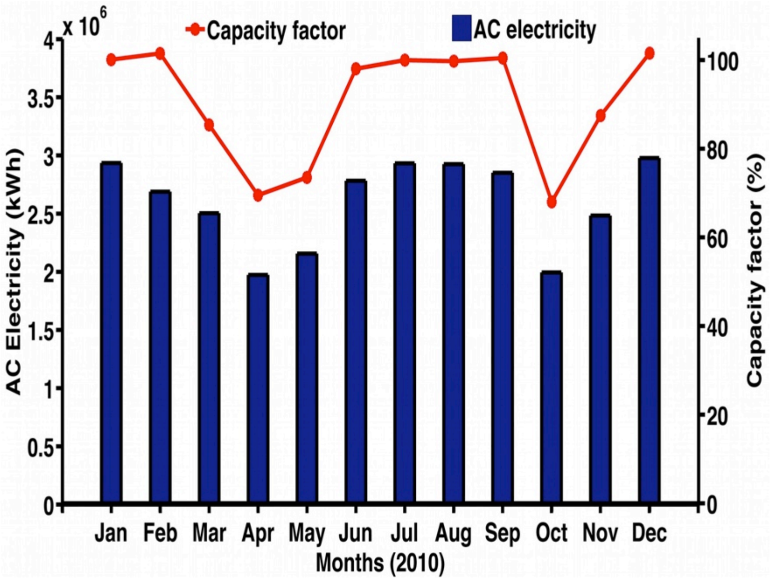

Fig. 7.6: Monthly AC electricity output and capacity factors for Palo Verde nuclear power plant

We then calculated the capacity factors for some of the PV systems installed on the university buildings are given in Table 7.1. We calculated the monthly capacity factors by dividing the monthly total AC electricity energy generated from the PV system by the product of the system size and total number of hours in that particular month. The table also gives the system ratings, tracking type (fixed vs. single axis tracking), and module type (thin film vs. poly silicon). All the fixed tilt systems are south facing systems tilted at 20-degree from the horizontal, instead of the conventional latitude tilt (33 degree for Phoenix, AZ) to minimize the effect of wind load on PV modules. Average annual capacity factors for PV systems installed at ASU campus. The average capacity factor for a fixed tilt poly-silicon system is approximately 20.3%, lower than that for single axis tracking poly-silicon system with capacity factor of 23%. The low capacity factor of 18.5% for Building F poly-silicon PV system compared to a similar system at Building E is due to intermittent component failures.

TABLE 7.1: Average annual capacity factors for PV systems installed at ASU campus

Building	System size	System type	Module type	Annual Capacity factor
	(kW)			(%)
A	161	Fixed	Poly-Si	20.3
B	80	Fixed	Poly-Si	20.3
C	70	Fixed	Poly-Si	20.1
D	108	Fixed	CdTe thin film	19.4
E	76	Fixed	Poly-Si	21.0
F	42	Fixed	Poly-Si	18.5
G	880	1-axis tracker	Poly-Si	23.0
H	711	1-axis tracker	Poly-Si	22.4
I	23	Fixed	Poly-Si	20.4

Fig. 7.7 shows the typical variation in monthly capacity factors for a 711 kW_p single axis tracking poly-silicon system installed on a building. The capacity factors were as high as 31% during the months of May and dropped to 10% in December. As the incident solar irradiance reduces in winter months, the system output and therefore, the capacity factor drops. Capacity factor drops during the months from June to August due to reduced system output as a result of increased cell temperature. The poly-silicon solar cell has a negative temperature coefficient of power of approximately -0.5%/°C, which significantly reduces the system output during hot summer months of June-August. The difference between the capacity factors of a nuclear power plant and a PV system arises due to the simple fact that the sun shines only for certain number of hours per day, which significantly limits the output of PV systems. The negative effect of temperature on system output, non optimal sun tracking, inverter losses, balance of system losses, system downtimes all contribute to further lower the PV system's capacity factor.

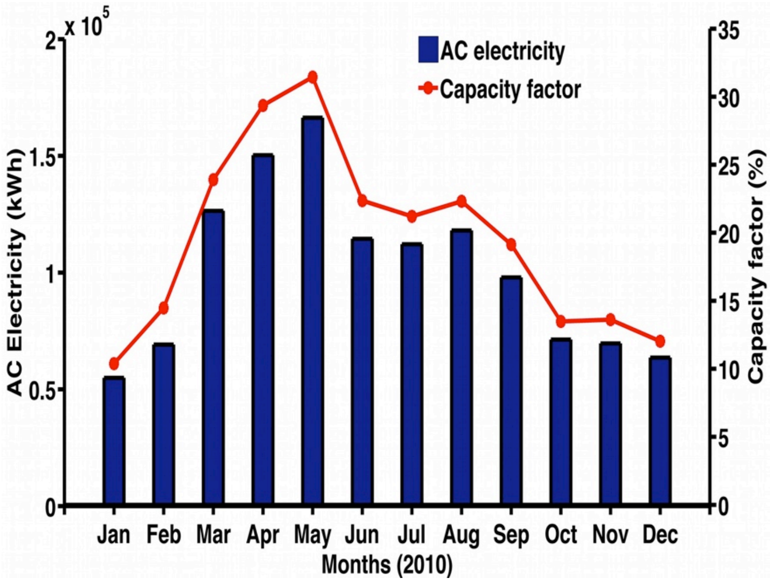

Fig. 7.7: Monthly AC electricity output and capacity factors for a single axis tracking PV system installed at ASU campus

7.3.5 Simulated vs. real capacity factors

In order to further determine the effect of tracking systems on PV system's capacity factor, we decided to simulate a PV system using the System Advisor Model (SAM) made available by National Renewable Energy Laboratory (NREL). SAM is used to simulate and predict the annual performance of a PV system for various input parameters of module and inverter technologies, location, meteorological data and financial conditions. For this work, we designed a PV system using SAM that was equivalent to one of the PV systems (70 kW_p) installed at the university that uses poly-silicon modules fixed at 20-degree tilt. For the simulation, we varied the system mounting for four different cases: fixed 20-degree tilt, fixed latitude tilt (33-degree), single axis, and double axis tracking. TMY3 meteorological data was used as the input to the simulator to calculate the monthly AC electricity output for the four cases. Using the AC electricity output, we calculated the simulated capacity factors for the system and compared it with the actual measured capacity factors obtained under real conditions.

As shown in Fig. 7.8, actual measured system capacity factors closely match the simulated capacity factors and the minor differences arise due to variations between actual and TMY3 meteorological conditions. Another important point that can be noticed from Fig. 7.8 is that the average yearly capacity factor is equal for a system fixed at 20-degree tilt or at latitude 33-degree tilt at 20%. The general trend for mounting a PV system at a given location is to fix the tilt of the system at that location's latitude. Our analysis shows that even though the latitude tilt system performs better (higher capacity factor) during the winter months (October – March), the 20-degree tilt system outperforms it during the rest of the year (April- September). While the fixed 20-degree tilt system's average yearly capacity factor was only 20%, switching to a two axis tracking system significantly improved the system capacity factor to 28%. However, there is a very minor difference between average yearly capacity factors from a single axis and a two-axis system.

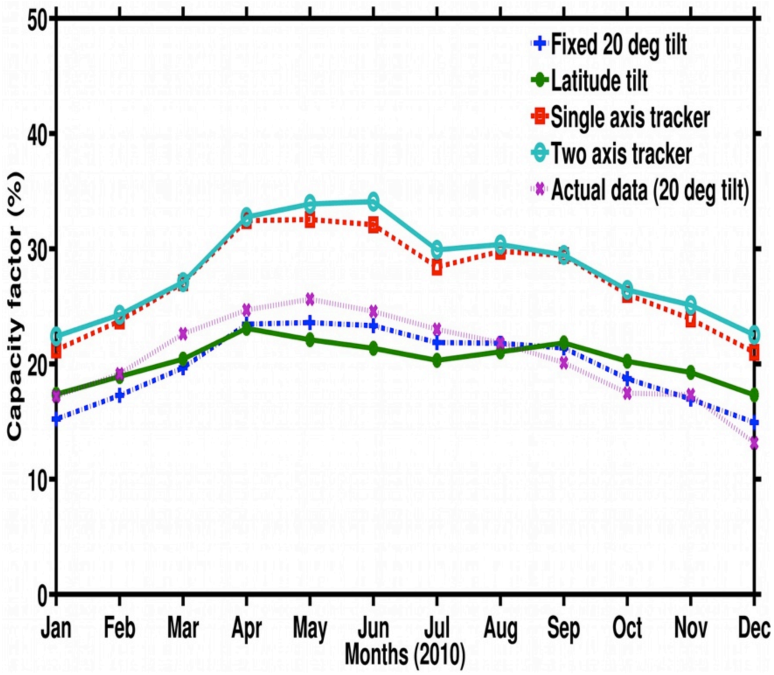

Fig. 7.8: Simulated and actual monthly capacity factors for a 70 kW_p PV system installed at ASU campus

Chapter 8

CONCLUSION AND FUTURE WORK

8.1 Conclusion

In this work, the properties of the charges present in the SiN_x films are studied. These charges are known to originate from specific silicon-nitrogen dangling bonds ($\cdot Si\equiv N$), known as K center defects. The K centers, being the primary charge trapping defects can exist in three different charged states: positively charged K^+ (), neutral K^0 ($\uparrow$) and negatively charged K^- ($\uparrow\downarrow$) defect, carrying zero, one and two electrons respectively on the dangling bond. Corona charging technique was used to externally inject positive or negative charges in the SiN_x film and therefore change the polarity of the charges in the film. This way, SiN_x film can be applied to both n-doped as well as p-doped Si surfaces. C-V measurements showed the presence of net negative charges (~ -7×10^{12} cm^{-2}) after negative charging treatment and net positive charges (~ $+5 \times 10^{12}$ cm^{-2}) after positive charging treatment of the SiN_x film. High energy (~ 4.9 eV) UV radiation was used to neutralize and control the net charge density in the SiN_x film.

Electron Spin Resonance (ESR) technique was used in addition to C-V technique in understanding the overall charge distribution picture in the SiN_x film. While, the C-V measurements could only give the net charge density (positive or negative) in the SiN_x film, ESR measurement were used to detect and quantify the neutral K^0 defect density of the film. ESR measurements showed the presence of neutral, paramagnetically active, K^0 defects in as deposited SiN_x films that enabled positive or negative charging of the film. ESR measurements were also taken to quantify the effect of UV illumination and high temperature annealing treatments on SiN_x film. While UV treatment increased the density of neutral K^0 defects by as much as 86%, both charging treatment and FGA annealing decreased the K^o density by 50% and 66% respectively, indicating that the K centers were indeed participating in the charging processes.

Based on the observations, a new model for charge distribution in the SiN_x films was proposed in this work. This model suggests the presence of K centers throughout the bulk of the SiN_x film and not just at the SiN_x – Si interface. Using etch-back C-V and ESR measurements, it was shown that after the charging treatment, the externally injected charges were uniformly distributed in the bulk of the SiN_x film. Rinsing the SiN_x film did not have any impact on the magnitude of the charges. The externally injected charges in the SiN_x film were found to be stable up-to a year in indoor environment at room temperature. However, high temperature treatments (annealing, contact firing) were found to completely wipe out the injected charges.

Lastly, SiN_x films deposited on either sides of textured and cleaned p-doped as well as n-doped, standard, 180 μm thick, solar grade CZ-Si substrates were charged and the effect of charging the SiN_x film on minority carrier lifetimes of the CZ samples was measured. It was found charging the SiN_x film increased the effective minority carrier lifetime of the sample by over two orders of magnitude (~ 251 μs), which was almost equal to the bulk lifetime of the CZ sample used. This result therefore, proved that the field effect passivation induced by externally injected charges in the SiN_x films can enhance the minority carrier lifetimes of the sample above and beyond the chemical passivation methods and effectively reduce the surface recombination activity to negligible levels.

8.2 Opportunities and challenges in integrating SiN_x charging process into standard solar cell fabrication process

8.2.1 Implication of SiN_x charging on cell efficiency: PC1D

To quantify the effect of externally injected charges in SiN_x films on solar cell efficiency, PC1D simulations were performed again on a standard p-doped silicon cell with n^+ emitter, which was previously described in Chapter 2. For this simulation, two n-emitter doping levels were selected: 60 Ω/□ representing a standard cell with a heavily doped n^+ emitter and 160 Ω/□ representative of lightly doped selective emitter cell architecture. External positive and negative surface charges used in this simulation were equal to the magnitude of charges injected in the SiN_x films using corona charging tool and measured using C-V techniques as explained in Chapter 5. Cell efficiency of the n^+-p solar cell was used as a performance metric measured at three stages:

1) Control: standard n^+-p cell with front SiN_x ARC film carrying $+5 \times 10^{11}$ cm^{-2} of as-deposited positive fixed charges and a rear Back Surface Field (BSF).
2) After positive charging of front SiN_x film: $+5 \times 10^{12}$ cm^{-2} front positive surface charge, rear BSF present.
3) After replacing rear BSF with negatively charged SiN_x film: $+5 \times 10^{12}$ cm^{-2} front positive surface charge, -7×10^{12} cm^{-2} rear negative surface charge, no BSF.

These three stages depict the sequence in which charging simulations were carried on a standard cell. While the first simulation was carried on a standard cell with SiN_x film carrying only as-deposited $+5 \times 10^{11}$ cm^{-2} positive fixed charges prior to any charging treatment, the second simulation was carried to quantify the effect of positive corona charging of the front SiN_x film that injected $+5 \times 10^{12}$ cm^{-2} of external charges in the film. In both of these simulation cases, a standard BSF was present at the rear of the cell. Lastly, for the third simulation, the rear BSF was replaced by a negatively charged SiN_x film carrying -7×10^{12} cm^{-2} charges. The other relevant parameters used for PC1D simulations are listed in Table 8.1.

TABLE 8.1: Cell parameters for PC1D simulation

Parameter	Value
Thickness	180 μm
Cell area	1 cm^2
p-type base doping	Boron, 5×10^{15} cm^{-3}
n-emitter doping (high)	Phosphorus, 2×10^{20} cm^{-3} (60 Ω/□)
n-emitter doping (low)	Phosphorus, 6×10^{19} cm^{-3} (160 Ω/□)
Bulk lifetime	500 μs
Front surface recombination velocity	1×10^4 cm/s
Rear surface recombination velocity	1×10^5 cm/s
Front surface	Textured
Spectrum	AM 1.5 G
Cell temperature	25 °C
Light intensity	0.1 W/cm^2

TABLE 8.2: PC1D simulated cell efficiency as a function of surface charges applied on the front and rear surfaces of the cell

Emitter doping	(1) Control cell	(2) After positive charging of front SiN_x film, BSF present	(3) After replacing rear BSF with negatively charged SiN_x film
	As-deposited front SiN_x ARC ($+5 \times 10^{11}$ cm^{-2}) and rear BSF	$+5 \times 10^{12}$ cm^{-2} front surface charge, rear BSF present	$+5 \times 10^{12}$ cm^{-2} front surface, -7×10^{12} cm^{-2} rear surface charge, no BSF
60 Ω/□	18.2 %	18.2 %	19.1 %
160 Ω/□	18.5 %	18.6 %	20.0 %

Table 8.2 lists the simulated cell efficiencies of the n^+-p cell for two emitter doping levels as a function of surface charges applied on the front and rear surfaces of the cell. For the case of heavily doped n-emitter, the standard control cell, with as-deposited SiN_x film with no externally injected charge, had a cell efficiency of 18.2%. After putting in extra positive front surface charges ($+5 \times 10^{12}$ cm^{-2}) to simulate the effect of positive corona charging of the front SiN_x film in the second simulation case, the cell efficiency did not change. The primary reason being the well passivated front surface and a heavy emitter doping concentration that resulted in no effect of field effect passivation brought by increased surface charges, as previously shown in Fig. 2.4. However, for the third simulation case, where the rear BSF was replaced by a negatively charged SiN_x film carrying -7×10^{12} cm^{-2} charges, the cell efficiency significantly improved to 19.1 %, indicating a better rear surface passivation achieved by the negative charges on the p-doped surfaces compared to the standard Al BSF region. Similar trend was noticed for the lightly doped emitter where replacing the rear BSF region by the negatively charged SiN_x film increased the cell efficiency from 18.6 % to 20.0 %. This simulation thus demonstrated the beneficial role of externally injected charges in SiN_x films applied on the front and rear surfaces of the cell in significantly improving the cell efficiencies.

8.2.2 Opportunities by integrating SiN_x charging process

The single biggest opportunity or advantage in using SiN_x charging process demonstrated in this work is that the same SiN_x film can be applied on the front and rear surfaces (n or p-type) of the silicon solar cell by externally injecting positive or negative charges. This ability to inject either polarity of charge in the SiN_x film therefore, overcomes the inherent limitations of negatively charged Al_2O_3 films and as-deposited SiN_x films with only positive charges. As demonstrated by the PC1D simulations in the previous section, applying a negatively charged SiN_x film at the rear p-doped surfaces significantly improved the cell efficiency by better passivating the surfaces. The dielectric film stack (SiN_x/SiO_2) applied at the rear surfaces can be optimized further to reflect the light from the rear surfaces to further enhance the light trapping properties of the cell. Excess positive charges injected in the SiN_x film applied on the front n-type emitter surfaces, greater than the as-deposited amount, can also improve cell efficiencies for cell architectures with lightly doped emitter profiles such as in selective emitter cells.

The corona charging technique described in this work is an extremely fast and easy charge manipulation process that will allow easy integration of this technique into standard cell fabrication processes. The charging technique works in normal atmospheric conditions and does not require any surface preparation work. Since, no charge tunneling occurs during the charging of SiN_x film and the underlying Si substrates due to the presence of 20 nm thick SiO_2 layer, either polarity (positive or negative) of charges can be injected in the SiN_x film independent of the doping type and doping concentration of the underlying Si substrate. The corona charging mechanism is able to inject charges uniformly over a large area that makes it suitable to use on standard 156 mm x 156 mm solar substrates.

8.2.3 Challenges in integrating SiN_x charging process

There are certain challenges that need to be overcome prior to integrating the SiN_x charging process in the cell fabrication process. The stability of externally injected SiN_x charges under sunlight needs to be understood and improved. As explained in Section 5.7, while the charges were wiped out when the samples were exposed to sunlight for a week, the same charges remained stable when exposed to a 365 nm UV light as shown in Fig. 6.5. Therefore, once the critical cutoff wavelength of the light is determined above which the charges will remain stable; a special PV glass can then be designed accordingly and placed over the charged SiN_x film, to transmit sunlight above the cutoff wavelength. Further, applying a negatively charged SiN_x film on the rear p-type surfaces will not be affected by the UV light and will therefore remain stable for a longer period of time. An Oxide/Nitride/Oxide dielectric film stack can also be investigated to improve the UV stability of the injected charges.

As it was reported in Chapter 5, the externally injected charges in the SiN_x film were found to be stable up-to a year under normal room temperatures (~ 40°C), however, high temperature processing steps (400°C or higher) completely removed these charges. The charge was lost primarily into the atmosphere through the top SiN_x film, as the bottom SiO_2 layer blocked the transition of charge into the Si substrate. The O/N/O film stack can therefore, be used to improve the thermal stability of injected charges in the SiN_x film. Further, charging of SiN_x film should be performed at the end of the cell fabrication sequence once all the high temperature processing steps involving annealing and metal contact firing are done to make the SiN_x charges thermally stable.

8.3 Future work

The UV and thermal stability of the injected charge in the SiN_x film needs to be improved. Modifying the SiN_x film properties, employing new dielectric film stack structure can help retain the injected charges after high temperature exposures. Further, the next step is to integrate the SiN_x charge manipulation step into standard solar cell fabrication processes. The performance of standard n^+-p Si solar cells consisting of positively charged front SiN_x film and negatively charged rear SiN_x film needs to be measured and compared with those cells consisting of negatively charged thin Al_2O_3/SiN_x rear stack.

REFERENCES

[1] Justin Gillis (2013, March 7), Global temperatures highest in 4000 years, The New York Times [Online], Available: http://www.nytimes.com/2013/03/08/science/earth/global-temperatures-highest-in-4000-years-study-says.html

[2] S.A. Marcott, J. D. Shakun, P.U. Clark, A.C. Mix, “A Reconstruction of Regional and Global Temperature for the Past 11,300 Years,” *Science*, vol. 339, no. 6124, pp. 1198-1201, 2013

[3] J. Hansen, M. Sato, R. Ruedy, “Perception of climate change,” Proceedings of the *National Academy of Sciences*, vol. 109, no. 37, pp. E2415-E2423, 2012

[4] NASA Global Climate Change, [Online], 2013, http://climate.nasa.gov/, (Last accessed: March 17, 2013)

[5] O. Edenhofer, R. Pichs-Madruga, Y. Sokona, eds., “Renewable energy sources and climate change mitigation: Special report of the intergovernmental panel on climate change,” Cambridge University Press, NY, USA 2012

[6] R. Gelman, “2011 Renewable Energy Data Book,” National Renewable Energy Laboratory, CO, USA, 2011

[7] Solar Energy Industries Association, “US Solar Market Insight Report 2012 Q2,” Washington, DC, 2012

[8] M.D. Platzer, “US Solar Photovoltaic Manufacturing: Industry Trends, Global Competition, Federal Support,” Congressional Research Service, Washington, DC, 2012

[9] US Department of Energy, “2010 Solar Technologies Market Report,” Washington DC, 2011

[10] Z. Wang, P. Han, H. Lu, H. Qian, L. Chen, Q. Meng, et al., “Advanced PERC and PERL production cells with 20.3% record efficiency for standard commercial p-type silicon wafers,” *Progress in Photovoltaics: Research and Applications*, vol. 20, pp. 260-268, 2012

[11] US Energy Information Administration, “Solar Photovoltaic Cell/Module Shipments Report 2011”, US Department of Energy, Washington D.C., USA 2012

[12] R. A. Sinton, “Crystalline Silicon Technologies” presented at the 38th IEEE Photovoltaic Specialists Conference (PVSC), Austin, TX, 2012

[13] J. Szlufcik, S. Sivoththaman, J.F. Nlis, R.P. Mertens, R. Van Overstraeten, “Low-cost industrial technologies of crystalline silicon solar cells,” in *Proceedings of the IEEE 85*, issue 5, pp.711-730, 1997

[14] M. A. Green, "Crystalline and thin-film silicon solar cells: state of the art and future potential," *Solar energy*, vol. 74, pp. 181-192, 2003

[15] D.H. Neuhaus, A. Münzer, "Industrial silicon wafer solar cells," *Advances in OptoElectronics*, 2007

[16] M.A.Green, "The path to 25% silicon solar cell efficiency: History of silicon cell evolution," *Progress in Photovoltaics: Research and Applications*, vol. 17, pp. 183-189, 2009

[17] ITRPV 2012, "International Technology Roadmap for Photovoltaics Results 2012," Third Edition, Berlin, 2012, www.ITRPV.net

[18] D. K. Schroder, *Semiconductor Material and Device Characterization*, Third Edition, Wiley-Interscience Publication, 2006, ISBN 0 471 73906 5

[19] D.K. Schroder, "Carrier lifetimes in Silicon," presented at Arizona State University, Tempe, AZ, March 2012

[20] A.G. Aberle, *Crystalline Silicon Solar Cells - Advanced Surface Passivation and Analysis,* Center for Photovoltaic Engineering, University of New South Wales, Sydney, Australia, 1999, ISBN 0 7334 0645 9

[21] A.G. Aberle, S. Glunz, W. Warta, "Field effect passivation of high efficiency silicon solar cells," *Solar Energy Materials and Solar Cells*, vol. 29, issue 2, pp. 175-182, 1993

[22] PC1D software version 5.9, [Online], http://www.pv.unsw.edu.au/info-about/our-school/products-services/pc1d, (Last accessed: March 20, 2013)

[23] Z. Wang, P. Han, H. Lu, H. Qian, L. Chen, Q. Meng, N. Tang et al., "Advanced PERC and PERL production cells with 20.3% record efficiency for standard commercial p-type silicon wafers," *Progress in Photovoltaics: Research and Applications*, vol. 20, no. 3, pp. 260-268, 2012

[24] Y. Gassenbauer, K. Ramspeck, B. Bethmann, K. Dressler, J.D. Moschner, M. Fiedler, E. Brouwer, et al., "Rear-Surface Passivation Technology for Crystalline Silicon Solar Cells: A Versatile Process for Mass Production," *IEEE Journal of Photovoltaics*, vol. 3, issue 1, pp.125-130, 2013

[25] J. Dupuis, E. Fourmond, V. Mong-The Yen, O. Nichiporuk, M. Greffioz, N. Le Quang, M. Lemiti, "Study of Rear PECVD Dielectric Stacks for Industrial Silicon Solar Cells," in *Proceedings of the 24th European Photovoltaic Solar Energy Conference*, Hamburg, Germany, 2009, pp. 1623-1627

[26] E. Schmich, Y. Gassenbauer, K. Ramspeck, K. Dressler, M. Fiedler, W. Hefner et al., "Industrial multi-crystalline silicon solar cells with dielectrically passivated rear side and efficiencies above 18%," in *Proceedings of the 25th European Photovoltaic Solar Energy Conference*, Valencia, Spain, 2010, pp. 1154–1157

[27] P. Wawer, J. Müller, M. Fischer, P. Engelhart, A. Mohr, K. Petter, "Latest Trends in Development and Manufacturing of Industrial, Crystalline Silicon Solar-Cells", *Energy Procedia*, Vol. 8, pp. 2-8, 2011

[28] T. Dullweber, S. Gatz, H. Hannebauer, T. Falcon, R. Hesse, J. Schmidt, R. Brendel, "Towards 20% efficient large-area screen-printed rear-passivated silicon solar cells," *Progress in Photovoltaics: Research and Applications*, vol. 20, pp. 630–638, 2012

[29] K.A. Münzer, J. Schöne, A. Teppe, R.E. Schlosser, M. Hein, D. Hammer, S. Hüls et al., "Advanced rear side technology for industrial high efficiency solar cells," in *Proceedings of the 25th European Photovoltaic Solar Energy Conference*, Valencia, Spain, 2010, pp. 2314–2318

[30] S. Dauwe, L. Mittelstädt, A. Metz, R. Hezel, "Experimental evidence of parasitic shunting in silicon nitride rear surface passivated solar cells," *Progress in Photovoltaics: Research and Applications*, vol. 10, pp. 271-278, 2002

[31] R. Hezel, K. Jaeger, "Low Temperature Surface Passivation of Silicon for Solar Cells," *Journal of Electrochemical Society*, vol. 136, pp. 518-523, 1989

[32] G. Agostinelli, A. Delabie, P. Vitanov, Z. Alexieva, H.F.W. Dekkers, S. De Wolf, G. Beaucarne, "Very low surface recombination velocities on p-type silicon wafers passivated with a dielectric with fixed negative charge," *Solar energy materials and solar cells*, vol. 90, issue 18, pp. 3438-3443, 2006

[33] B. Hoex, S.B.S. Heil, E. Langereis, M.C.M Van de Sanden, W.M.M Kessels, "Ultralow surface recombination of c-Si substrates passivated by plasma-assisted atomic layer deposited Al_2O_3," *Applied Physics Letters*, vol. 89, pp. 042112/1-3, 2006

[34] B. Hoex, J. Schmidt, R. Bock, P.P. Altermatt, M.C.M Van de Sanden, W.M.M. Kessels, "Excellent passivation of highly dope p-type Si surfaces by the negative-charge-dielectric Al_2O_3," *Applied Physics Letters*, vol. 91, pp. 112107, 2007

[35] B. Hoex, J.J.H. Gielis, M.C.M. Van de Sanden, W.M.M Kessels, "On the c-Si surface passivation mechanism by the negative-charge-dielectric Al_2O_3," *Journal of Applied Physics*, vol. 104, pp. 113703, 2008

[36] B. Hoex, J. Schmidt, P. Pohl, M.C.M. Van de Sanden, W.M.M. Kessels, "Silicon surface passivation by atomic layer deposited Al_2O_3," *Journal of Applied Physics*, vol. 104, issue 4, pp. 044903, 2008

[37] T. Li, A. Cuevas, "Effective surface passivation of crystalline silicon by rf sputtered aluminum oxide," *Physica Status Solidi RRL*, vol. 3, pp. 160-162, 2009

[38] P. Saint-Cast, D. Kania, M. Hofmann, J. Benick, J. Rentsch, R. Preu, "Very low surface recombination velocity on p-type c-Si by high-rate plasma-deposited aluminum oxide," *Applied Physics Letters*, vol. 95, issue 15, pp. 151502, 2009

[39] F. Werner, B. Veith, V. Tiba, P. Poodt, F. Roozeboom, R. Brendel, J. Schmidt, "Very low surface recombination velocities on p-and n-type c-Si by ultrafast spatial atomic layer deposition of aluminum oxide," *Applied Physics Letters*, vol. 97, pp. 162103, 2010

[40] N.M. Terlinden, G. Dingemans, M.C. Van de Sanden, W.M.M. Kessels, "Role of field-effect on c-Si surface passivation by ultrathin (2–20 nm) atomic layer deposited Al_2O_3," *Applied Physics Letters*, vol. 96, issue 11, pp. 112101, 2010

[41] J. Schmidt, A. Merkle, R. Bock, P.P. Altermatt, A. Cuevas, N.P. Harder, B. Hoex et al. "Progress in the surface passivation of silicon solar cells, " in *Proceedings of the 23rd European Photovoltaic Solar Energy Conference*, Valencia, Spain, 2008, pp. 974-981

[42] J. Schmidt, A. Merkle, R. Brendel, B. Hoex, M.C.M Van de Sanden, W.M.M. Kessels, "Surface passivation of high-efficiency silicon solar cells by atomic-layer-deposited Al_2O_3," *Progress in Photovoltaics: Research and Applications*, vol. 16, pp. 461-466, 2008

[43] P. Saint-Cast, J. Benick, D. Kania, L. Weiss, M. Hofmann, J. Rentsch, R. Preu, S.W. Glunz, "High-efficiency c-Si solar cells passivated with ALD and PECVD aluminum oxide." *IEEE Electron Device Letters*, vol. 31, issue 7, pp. 695-697, 2010

[44] S. Gatz, H. Hannebauer, R. Hesse, F. Werner, A. Schmidt, T. Dullweber, J. Schmidt, K. Bothe, R. Brendel, "19.4%-efficient large-area fully screen-printed silicon solar cells," *physica status solidi RRL*, vol. 5, issue 4, pp. 147-149, 2011

[45] J. Benick, B. Hoex, G. Dingemans, A. Richter, M. Hermle, S. W. Glunz, "High-efficiency n-type silicon solar cells with front side boron emitter," in *Proceedings of the 24th European Photovoltaic Solar Energy Conference*, 2009, pp. 863-870

[46] A. Richter, M. Hoteis, J. Benick, S. Henneck, M. Hermle, S. W. Glunz, "Towards industrially feasible high-efficiency n-type Si solar cells with boron-diffused front side emitter-combining firing stable Al_2O_3 passivation and fine-line printing," in *35th IEEE Photovoltaic Specialists Conference (PVSC)*, Honolulu, HI, 2010, pp. 003587-003592

[47] B. Hoex, M.C.M van de Sanden, J. Schmidt, R. Brendel, W.M.M. Kessels, "Surface passivation of phosphorus-diffused n^+ type emitters by plasma-assisted atomic-layer deposited Al_2O_3," *physica status solidi RRL*, vol. 6, pp. 4 - 6, 2012

[48] J. Schmidt, F. Werner, B. Veith, D. Zielke, S. Steingrube, P. P. Altermatt, S. Gatz, T. Dullweber, R. Brendel, "Advances in the Surface Passivation of Silicon Solar Cells," *Energy Procedia*, vol. 15, pp. 30-39, 2012

[49] M.Z. Rahman, S.I. Khan, "Advances in surface passivation of c-Si solar cells," *Materials for Renewable and Sustainable Energy*, vol. 1, pp. 1-11, 2012

[50] G. Dingemans, E. Kessels, "Status and prospects of Al_2O_3 based surface passivation schemes for silicon solar cells," *Journal of Vacuum Science &*

Technology A: Vacuum, Surfaces, and Films, vol. 30, no. 4, pp. 040802-040802, 2012

[51] K. Matsunaga, T. Tanaka, T. Yamamoto, Y. Ikuhara, "First-principles calculations of intrinsic defects in Al_2O_3," *Physical Review B*, vol. 68, issue 8, pp. 085110, 2003

[52] D. Liu, S.J. Clark, and J. Robertson, "Oxygen vacancy levels and electron transport in Al_2O_3," *Applied Physics Letters*, vol. 96, pp. 032905, 2010

[53] F. Werner, B. Veith, D. Zielke, L. Kühnemund, C. Tegenkamp, M. Seibt, R. Brendel, J. Schmidt, "Electronic and chemical properties of the c-Si/Al_2O_3 interface," *Journal of Applied Physics*, vol. 109, pp. 113701, 2011

[54] J.R. Weber, A. Janotti, C.G. Van de Walle, "Native defects in Al_2O_3 and their impact on III-V/Al_2O_3 metal-oxide-semiconductor-based devices," *Journal of Applied Physics*, vol. 109, pp. 033715, 2011

[55] G. Dingemans, P. Engelhart, R. Seguin, F. Einsele, B. Hoex, M.C.M. Van de Sanden, W.M.M. Kessels, "Stability of Al_2O_3 and Al_2O_3/a-SiN_x:H stacks for surface passivation of crystalline silicon," *Journal of Applied Physics*, vol. 106, pp. 114907, 2009

[56] J. Benick, A. Richter, M. Hermle, S.W. Glunz, "Thermal stability of the Al_2O_3 passivation on p-type silicon surfaces for solar cell applications," *physica status solidi RRL*, vol. 3, pp. 233-235, 2009

[57] B. Veith, F. Werner, D. Zielke, R. Brendel, J. Schmidt, "Comparison of the thermal stability of single Al_2O_3 layers and Al_2O_3/SiN_x stacks for the surface passivation of silicon," *Energy Procedia*, vol. 8, pp. 307-312, 2011

[58] P. Saint-Cast, D. Kania, R. Heller, S. Kuehnhold, M. Hofmann, J. Rentsch, R.Preu, "High-temperature stability of c-Si surface passivation by thick PECVD Al_2O_3 with and without hydrogenated capping layers," *Applied Surface Science*, vol. 258, issue 21, pp. 8371-8376, 2012

[59] T. Lauinger, J. Schmidt, A.G. Aberle, R. Hezel, "Record low surface recombination velocities on 1 Ω cm p-silicon using remote plasma silicon nitride passivation," *Applied Physics Letters*, vol. 68, issue 9, pp. 1232-1234, 1996

[60] M.J. Kerr, A. Cuevas, "Recombination at the interface between silicon and stoichiometric plasma silicon nitride," *Semiconductor Science and Technology*, vol. 17, issue 2, pp. 166, 2002

[61] A.G. Aberle, T. Lauinger, J. Schmidt, R. Hezel, "Injection-level dependent surface recombination velocities at the silicon-plasma silicon nitride interface," *Applied physics letters*, vol. 66, issue 21, pp. 2828-2830, 1995

[62] C. Leguijt, "Low temperature surface passivation for silicon solar cells," *Solar Energy Materials and Solar Cells*, vol. 40, pp. 297-345, 1996

[63] J. Schmidt, A.G. Aberle, "Carrier recombination at silicon–silicon nitride interfaces fabricated by plasma-enhanced chemical vapor deposition," *Journal of Applied Physics*, vol. 85, issue 7, pp. 3626-3633, 1999

[64] A. Aberle, "Surface Passivation of Crystalline Silicon Solar Cells: A Review," *Progress in Photovoltaics: Research and Applications*, vol. 8, pp. 473-487, 2000

[65] A. Aberle, "Overview on SiN surface passivation of crystalline silicon solar cells," *Solar Energy Materials and Solar Cells*, vol. 65, pp. 518-23, 2001

[66] J. Schmidt, M. Kerr, A. Cuevas, "Surface passivation of silicon solar cells using plasma-enhanced chemical-vapour-deposited SiN films and thin thermal SiO_2/plasma SiN stacks," *Semiconductor Science and Technology*, vol. 16, issue 3, pp. 164-170, 2001

[67] M.J. Kerr, J. Schmidt, A. Cuevas, J.H. Bultman, "Surface recombination velocity of phosphorus-diffused silicon solar cell emitters passivated with plasma enhanced chemical vapor deposited silicon nitride and thermal silicon oxide," *Journal of Applied Physics*, vol. 89, issue 7, pp. 3821-3826, 2001

[68] F. Duerinckx, J. Szlufcik, "Defect passivation of industrial multicrystalline solar cells based on PECVD silicon nitride," *Solar Energy Materials and Solar Cells*, vol. 72, pp. 231-246, 2002

[69] I.G. Romijn, W.J. Soppe, H.C. Rieffe, W.C. Sinke, A.W. Weeber, "Passivating multi-crystalline Si solar cells using SiN_x:H," at *15th Workshop on Crystalline Silicon Solar Cells & Modules: Materials and Processes*, Vail, Colorado, USA, 2005

[70] A. Cuevas, M.J. Kerr, J. Schmidt, "Passivation of crystalline silicon using silicon nitride," at *3rd World Conference on Photovoltaic Energy Conversion*, Osaka, Japan, 2003, pp. 913-918

[71] J.D. Moschner, J. Henze, J. Schmidt, R. Hezel, "High-quality surface passivation of silicon solar cells in an industrial-type inline plasma silicon nitride deposition system," *Progress in Photovoltaics: Research and Applications*, vol. 12, issue 1, pp. 21-31, 2004

[72] W. Soppe, H. Rieffe, A. Weeber, "Bulk and surface passivation of silicon solar cells accomplished by silicon nitride deposited on industrial scale by microwave PECVD," *Progress in Photovoltaics: Research and Applications*, vol. 13, pp. 551-569, 2005

[73] H.J. Stein, V.A. Wells, R.E. Hampy, "Properties of Plasma-Deposited Silicon Nitride," *Journal of the Electrochemical Society*, vol. 126, issue 10, pp. 1750-1754, 1979

[74] F.W. Sexton, "Plasma nitride AR coatings for silicon solar cells," *Solar Energy Materials*, vol. 7, issue 1, pp. 1-14, 1982

[75] P. Doshi, G.E. Jellison, A. Rohatgi, "Characterization and optimization of absorbing plasma-enhanced chemical vapor deposited antireflection coatings for silicon photovoltaics," *Applied Optics*, vol. 36, issue 30, pp. 7826-7837, 1997

[76] L. Cai, A. Rohatgi, S. Han, G. May, M. Zou, "Investigation of the properties of plasma-enhanced chemical vapor deposited silicon nitride and its effect on silicon surface passivation," *Journal of Applied Physics*, vol. 83, pp. 5885-5889, 1998

[77] T. Lauinger, J. Moschner, A.G. Aberle, R. Hezel, "Optimization and characterization of remote plasma-enhanced chemical vapor deposition silicon nitride for the passivation of p-type crystalline silicon surfaces," *Journal of Vacuum Science & Technology A: Vacuum, Surfaces, and Films*, vol. 16, issue 2, pp. 530-543, 1998

[78] H. Nagel, A.G. Aberle, R. Hezel, "Optimised antireflection coatings for planar silicon solar cells using remote PECVD silicon nitride and porous silicon dioxide," *Progress in Photovoltaics: Research and Applications*, vol. 7, issue 4, pp. 245-260, 1999

[79] S. Ponce-Alcantara, C. del Canizo, J. Hofstetter, A. Luque, "The Effect of RF and MW Power on the SiN_x Films Grown by PECVD," in *2007 IEEE Spanish Conference on Electron Devices*, pp. 33-36

[80] T. Lauinger, J. Moschner, A.G. Aberle, R. Hezel, "UV stability of highest-quality plasma silicon nitride passivation of silicon solar cells," in *Conference Record of the 25th IEEE Photovoltaic Specialists Conference*, Washington, D.C., 1996, pp. 417-420

[81] A.G. Aberle, R. Hezel, "Progress in Low-temperature Surface Passivation of Silicon Solar Cells using Remote-plasma Silicon Nitride," *Progress in Photovoltaics: Research and Applications*, vol. 5, pp. 29-50, 1997

[82] L. Cai, A. Rohatgi, D. Yang, M.A. El-Sayed, "Effects of rapid thermal anneal on refractive index and hydrogen content of plasma-enhanced chemical vapor deposited silicon nitride films," *Journal of Applied Physics*, vol. 80, issue 9, pp. 5384-5388, 1996

[83] D.N. Wright, E.S. Marstein, A. Holt, "Effect of annealing on PECVD silicon nitride films," presented at *22nd European Photovoltaic Solar Energy Conference*, Milan, Italy, 2007, pp. 1651-1655

[84] B. Karunagaran, S.J. Chung, S. Velumani, E.K. Suh, "Effect of rapid thermal annealing on the properties of PECVD SiN_x thin films," *Materials Chemistry and Physics*, vol. 106, issue 1, pp. 130-133, 2007

[85] J.F. Lelièvre, E. Fourmond, A. Kaminski, O. Palais, D. Ballutaud, M. Lemiti, "Study of the composition of hydrogenated silicon nitride SiN_x:H for efficient surface and bulk passivation of silicon," *Solar Energy Materials and Solar Cells*, vol. 93, issue 8, pp. 1281-1289, 2009

[86] D. Frohman-Bentchkowsky, “The metal-nitride-oxide-silicon (MNOS) transistor Characteristics and applications,” *Proceedings of the IEEE*, vol. 58, 1970, pp. 1207–1219.

[87] D. Frohman-Bentchkowsky, M. Lenzlinger, “Charge Transport and Storage in Metal-Nitride-Oxide-Silicon (MNOS) Structures,” *Journal of Applied Physics*, vol. 40, pp. 3307-3319, 1969

[88] K.I. Lundstrom and C.M. Svensson, “Properties of MNOS structures,” *IEEE Transactions on Electron Devices*, vol. 19, pp. 826–836, 1972

[89] A.V. Ferris-Prabhu, “Theory of MNOS Memory Device Behavior,” *IBM Journal of Research and Development*, vol. 17, pp. 125–134, 1973

[90] P.C. Arnett, B.H. Yun, “Silicon nitride trap properties as revealed by charge–centroid measurements on MNOS devices,” *Applied Physics Letters*, vol. 26, p. 94-96, 1975

[91] K. Lehovec and D.W. Crain, “Charge centroid and trapping model for MNOS structures,” *Journal of Applied Physics*, vol. 47, p. 2763-2764, 1976

[92] Y. Takahashi and K. Ohnishi, “Evaluation of fixed charge distribution and its density in the insulation layer of metal-nitride-oxide-Si structure using slanted etching method,” *Electronics and Communications in Japan (Part II: Electronics)*, vol. 82, pp. 10–17, 1999

[93] V.J. Kapoor, R.A. Turi, “Charge storage and distribution in the nitride layer of the metal-nitride-oxide semiconductor structures,” *Journal of Applied Physics*, vol. 52, pp. 311-319, 1981

[94] V.J. Kapoor, J.P. Delatore, “Effects of oxide thickness on charge trapping in metal-nitride-oxide-semiconductor structures,” *Journal of Applied Physics*, vol. 53, pp. 5079-5085, 1982

[95] J. Robertson, M. J. Powell, “Gap states in silicon nitride,” *Applied Physics Letters*, vol. 44, issue 4, pp. 415, 1984

[96] J. Robertson, "Electronic structure of silicon nitride," *Philosophical Magazine B*, vol. 63, issue 1, pp. 47-77, 1991

[97] J. Robertson, “Defects and hydrogen in amorphous silicon nitride,” *Philosophical Magazine B*, vol. 69, issue 2, pp. 307-326, 1994

[98] S. Yokoyama, M. Hirose, Y. Osaka, “Electron Spin Resonance in Discharge-Produced Silicon Nitride,” *Japanese Journal of Applied Physics*, vol. 20, issue 1, pp. L35–L37, 1981

[99] D.T. Krick, P.M. Lenahan, J. Kanicki, “Stable photoinduced paramagnetic defects in hydrogenated amorphous silicon nitride,” *Applied Physics Letters*, vol. 51, pp. 608-610, 1987

[100] D.T. Krick, P.M. Lenahan, J. Kanicki, “Electrically active point defects in amorphous silicon nitride: An illumination and charge injection study,” *Journal of Applied Physics*, vol. 64, no. 7, pp. 3558, 1988

[101] D.T. Krick, P.M. Lenahan, J. Kanicki, “Nature of the dominant deep trap in amorphous silicon nitride,” *Physical Review B*, vol. 38, pp. 8226–8229, 1988

[102] D. Jousse, J. Kanicki, D.T. Krick, P.M. Lenahan, “Electron-spin-resonance study of defects in plasma-enhanced chemical vapor deposited silicon nitride,” *Applied Physics Letters*, vol. 52, no. 6, pp. 445, 1988

[103] D. Jousse, J. Kanicki, "Investigation of the light-induced effects in nitrogen-rich silicon nitride films," *Applied Physics Letters*, vol. 55, no. 11, pp. 1112-1114, 1989

[104] J. Kanicki, D. Jousse, A. Gelatos, M.S. Crowder, "Light-induced effects in hydrogenated amorphous nitrogen-rich silicon nitride films," *Journal of Non-Crystalline Solids*, vol. 114, pp. 612-614, 1989

[105] J. Kanicki, M. Sankaran, A. Gelatos, M.S. Crowder, E.D. Tober, "Stretched exponential illumination time dependence of positive charge and spin generation in amorphous silicon nitride,” *Applied Physics Letters*, vol. 57, issue 7, pp. 698-700, 1990

[106] M.S. Crowder, E.D. Tober, J. Kanicki, "Photobleaching of light-induced paramagnetic defects in amorphous silicon nitride films," *Applied Physics Letters*, vol. 57, issue 19, pp. 1995-1997, 1990

[107] C.H. Seager, J. Kanicki, "Photodarkening and bleaching in amorphous silicon nitride," *Applied Physics Letters*, vol. 57, issue 14, pp. 1378-1380, 1990

[108] J. Kanicki, W.L. Warren, C.H. Seager, M.S. Crowder, P.M. Lenahan, "Microscopic origin of the light-induced defects in hydrogenated nitrogen-rich amorphous silicon nitride films," *Journal of non-crystalline solids*, vol. 137, pp. 291-294, 1991

[109] C.H. Seager, J. Kanicki, "Near-ir absorption in chemically vapor deposited a:SiN$_x$:H films,” *Physical Review B*, vol. 46, issue 23, pp. 15163, 1992

[110] W.L. Warren, J. Robertson, J. Kanicki, "Si and N dangling bond creation in silicon nitride thin films," *Applied Physics Letters*, vol. 63, issue 19, pp. 2685-2687, 1993

[111] P.M. Lenahan, S.E. Curry, “First observation of the 29Si hyperfine spectra of silicon dangling bond centers in silicon nitride,” *Applied Physics Letters*, vol. 56, issue 2, pp. 157, 1990

[112] P.M. Lenahan, D.T. Krick, J. Kanicki, “The nature of the dominant deep trap in amorphous silicon nitride films: Evidence for a negative correlation energy,” *Applied Surface Science*, vol. 39, pp. 392–405, 1989

[113] D. Jousse, J. Kanicki, “Investigation of the light-induced effects in nitrogen-rich silicon nitride films,” *Applied Physics Letters*, vol. 55, issue 11, pp. 1112, 1989

[114] D. Jousse, J. Kanicki, J.H. Stathis, “Observation of multiple silicon dangling bond configurations in silicon nitride,” *Applied Physics Letters*, vol. 54, issue 11, pp. 1043, 1989

[115] J. Kanicki, D. Jousse, “Spatial charge distribution in as-deposited and UV-illuminated gate-quality nitrogen-rich silicon nitride,” *IEEE Electron Device Letters*, vol. 10, issue 6, pp. 277–279, 1989

[116] W.S. Lau, S.J. Fonash, J. Kanicki, “Stability of electrical properties of nitrogen-rich, silicon-rich, and stoichiometric silicon nitride films,” *Journal of Applied Physics*, vol. 66, issue 6, pp. 2765, 1989

[117] D. Jousse, J. Kanicki, J.H. Stathis, "Electron spin resonance study of metal-nitride-silicon structures: Observation of Si dangling bonds with different configurations and trapping properties in silicon nitride," *Applied Surface Science*, vol. 39, issue 1, pp. 412-419, 1989

[118] W. Warren, P. Lenahan, “Electron-nuclear double-resonance and electron-spin-resonance study of silicon dangling-bond centers in silicon nitride,” *Physical Review B*, vol. 42, issue 3, pp. 1773–1780, 1990

[119] W.L. Warren, F.C. Rong, E.H. Poindexter, G.J. Gerardi, J. Kanicki, "Structural identification of the silicon and nitrogen dangling-bond centers in amorphous silicon nitride," *Journal of applied physics*, vol. 70, pp. 346-354, 1991

[120] J. Kanicki, W.L. Warren, "Defects in amorphous hydrogenated silicon nitride films," *Journal of non-crystalline solids*, vol. 164, pp. 1055-1060, 1993

[121] S.E. Curry, P.M. Lenahan, D.T. Krick, J. Kanicki, C.T. Kirk, “Evidence for a negative electron-electron correlation energy in the dominant deep trapping center in silicon nitride films,” *Applied Physics Letters*, vol. 56, issue 14, pp. 1359, 1990

[122] W. Warren, P. Lenahan, S. Curry, “First observation of paramagnetic nitrogen dangling-bond centers in silicon nitride,” *Physical Review Letters*, vol. 65, issue 2, pp. 207–210, 1990

[123] E.D. Tober, J. Kanicki, M.S. Crowder, “Thermal annealing of light–induced metastable defects in hydrogenated amorphous silicon nitride,” *Applied Physics Letters*, vol. 59, issue 14, pp. 1723, 1991

[124] W. L. Warren, J. Kanicki, F.C. Rong, E.H. Poindexter, “Paramagnetic Point Defects in Amorphous Silicon Dioxide and Amorphous Silicon Nitride Thin Films II,” *Journal of The Electrochemical Society*, vol. 139, pp. 880-889, 1992

[125] W.L. Warren, J. Kanicki, F.C. Rong, E.H. Poindexter, P.J. McWhorter, “Charge trapping centers in N-rich silicon nitride thin films,” *Applied Physics Letters*, vol. 61, issue 2, pp. 216, 1992

[126] W.L. Warren, J. Kanicki, J. Robertson, E.H. Poindexter, P.J. McWhorter, "Electron paramagnetic resonance investigation of charge trapping centers in amorphous silicon nitride films," *Journal of applied physics*, vol. 74, pp. 4034-4046, 1993

[127] E.H. Poindexter, W.L. Warren, "Paramagnetic Point Defects in Amorphous Thin Films of SiO_2 and Si_3N_4: Updates and Additions," *Journal of The Electrochemical Society*, vol. 142, issue 7, pp. 2508-2516, 1995

[128] W.L. Warren, J. Kanicki, E.H. Poindexter, "Paramagnetic point defects in silicon nitride and silicon oxynitride thin films on silicon," *Colloids and Surfaces A: Physicochemical and Engineering Aspects*, vol. 115, pp. 311-317, 1996

[129] R. Hezel, R. Schörner, "Plasma Si nitride—A promising dielectric to achieve high-quality silicon MIS/IL solar cells," *Journal of Applied Physics*, vol. 52, issue 4, pp. 3076-3079, 1981

[130] R. Schörner, R. Hezel, "High efficiency inversion layer solar cells on polycrystalline silicon by the application of silicon nitride," *IEEE Transactions on Electron Devices*, vol. 28, issue 12, pp. 1466-1469, 1981

[131] R. Hezel, "Silicon nitride for the improvement of silicon inversion layer solar cells," *Solid-State Electronics*, vol. 24, issue 9, pp. 863-868, 1981

[132] R. Hezel, K. Blumenstock, R. Schörner, "Interface states and fixed charges in MNOS structures with APCVD and plasma silicon nitride," *Journal of the Electrochemical Society*, vol. 131, issue 7, pp. 1679-1683, 1984

[133] J.R. Elmiger, M. Kunst, "Investigation of charge carrier injection in silicon nitride/silicon junctions," *Applied Physics Letters*, vol. 69, issue 4, pp. 517-519, 1996

[134] S. Dauwe, "Low-temperature surface passivation of crystalline silicon and its application to the rear side of solar cells," Ph.D. dissertation, Univ. Hannover, Germany, 2004

[135] S. Dauwe, J. Schmidt, A. Metz, R. Hezel, "Fixed charge density in silicon nitride films on crystalline silicon surfaces under illumination," in *29th IEEE Photovoltaic Specialists Conference (PVSC)*, 2002, pp. 162-165

[136] H. Mäckel, R. Lüdemann, "Detailed study of the composition of hydrogenated SiN_x layers for high-quality silicon surface passivation," *Journal of Applied Physics*, vol. 92, pp. 2602-2608, 2002

[137] A.J.M. Van Erven, R.C.M. Bosch, M.D. Bijker, "Textured silicon surface passivation by high-rate expanding thermal plasma deposited SiN and thermal SiO_2/SiN stacks for crystalline silicon solar cells," *Progress in Photovoltaics: Research and Applications*, vol. 16, issue 7, pp. 615-627, 2008

[138] S. De Wolf, G. Agostinelli, G. Beaucarne, P. Vitanov, "Influence of stoichiometry of direct plasma-enhanced chemical vapor deposited SiN_x films and silicon substrate surface roughness on surface passivation," *Journal of Applied Physics*, vol. 97, issue 6, pp. 063303, 2005

[139] Y. Ren, N.M. Nursam, D. Wang, K.J. Weber, "Charge stability in LPCVD silicon nitride for surface passivation of silicon solar cells," in *35th IEEE Photovoltaic Specialists Conference (PVSC)*, Honolulu, HI, USA, 2010, pp. 000897-000901

[140] Y. Ren, K.J. Weber, N.M. Nursam, D. Wang, "Effect of deposition conditions and thermal annealing on the charge trapping properties of SiN_x films," *Applied Physics Letters*, vol. 97, issue 20, pp. 202907-202907, 2010

[141] Y. Ren, K.J. Weber, N.M. Nursam, "Modeling the charge decay mechanism in nitrogen-rich silicon nitride films," *Applied Physics Letters*, vol. 98, issue 12, pp. 122909-122909, 2011

[142] Y. Ren, K. Weber, F. Karouta, K. Vora, W. Liang, "Charge trapping and storage in SiN_x thin films deposited with Oxford PlasmaLab 100 system" in *38th IEEE Photovoltaic Specialists Conference (PVSC)*, Austin, TX, USA, 2012, pp. 001094-001097

[143] ASTM standard F1153-88, "Standard Test Method for Characterization of Metal-Oxide-Semiconductor (MOS) Structures by Capacitance-Voltage Measurements," American Society for Testing and Materials, 1988

[144] E.H. Nicollian, J.R. Brews, *MOS Physics and Technology*, Wiley, New York, 1982

[145] M. Brustolon, E. Giamello, *Electron Paramagnetic Resonance - A Practitioner's toolkit*, John Wiley and Sons Inc, New Jersey, USA, 2009, ISBN 978 0 470-25882-8

[146] R. Williams, "Photoemission of Electrons from Silicon into Silicon Dioxide," *Physical Review*, vol. 140, pp. A569 - A575, 1965

[147] A.M. Goodman, "Photoemission of Holes from Silicon into Silicon Dioxide," *Physical Review*, vol. 152, pp. 780-784, 1966

[148] ASTM standard G173-03 (2012), "Standard Tables for Reference Solar Spectral Irradiances: Direct Normal and Hemispherical on 37° Tilted Surface, " American Society for Testing and Materials, 2012

[149] Product datasheet, Solarphire™ PV high transmissive glass, PPG Industries, USA, May 2013

[150] W. Kaiser, P. Hi Keck, C.F. Lange, "Infrared absorption and oxygen content in silicon and germanium," *Physical Review*, vol. 101, issue 4, pp. 1264-1268, 1956

[151] K. Bothe, R. Hezel, J. Schmidt, "Understanding and reducing the boron-oxygen-related performance degradation in Czochralski silicon solar cells," *Solid State Phenomena*, vol. 95, pp. 223-228, 2003

[152] J. Schmidt, K. Bothe, "Structure and transformation of the metastable boron-and oxygen-related defect center in crystalline silicon," *Physical Review B*, vol. 69, issue 2, pp. 024107, 2004

[153] D. Macdonald, F. Rougieux, A. Cuevas, B. Lim, J. Schmidt, M. Di Sabatino, L.J. Geerligs, "Light-induced boron-oxygen defect generation in compensated p-type Czochralski silicon," *Journal of Applied Physics*, vol. 105, issue 9, pp. 093704-093704-7, 2009

[154] US Energy Information Administration, “Electric Power Annual 2009,” US Department of Energy, Washington DC, Apr. 2011

[155] Arizona State University news, [Online], “Sun devils soak up solar power,” Available: http://asunews.asu.edu/20110906_ASU10MWSolar, Sept. 2011, [Apr. 2012]

[156] Arizona State University, “Carbon Neutrality Action Plan,” Available: http://carbonzero.asu.edu/

[157] S. Rahman, B.D. Kroposki, “Photovolatics and demand side management performance analysis at a university building,” *IEEE Transactions on Energy Conversion*, vol. 8, issue 3, pp. 491-498, 1993

[158] P. Denholm, R.M. Margolis, “Evaluating the limits of solar photovoltaics (PV) in traditional electric power systems,” *Energy Policy*, vol. 35, issue 5, pp. 2852-2861, 2007

[159] M.S. El-Shobokshy, F.M. Hussein, “Degradation of photovoltaic cell performance due to dust deposition on to its surface,” *Renewable Energy*, vol. 3, issue 6-7, pp. 585-590, 1993

[160] M.S. El-Shobokshy, F.M. Hussein, “Effect of dust with different physical properties on the performance of photovoltaic cells,” *Solar Energy*, vol. 51, issue 6, pp. 505-511, 1993

[161] J. Zorrilla-Casanova, M. Piliougine, J. Carretero, P. Bernaola, P. Carpena, L. Mora-López, M. Sidrach-de-Cardona, “Analysis of dust losses in photovoltaic modules,” presented at *World Renewable Energy Congress*, Sweden, May 2011

[162] R. Hammond, D. Srinivasan, A. Harris, K. Whitfield, J. Wohlgemuth, “Effects of soiling on PV module and radiometer performance,” presented at *26th IEEE Photovoltaic Specialists Conference*, pp. 1121-1124, 1997

[163] M. Mani, R. Pillai, “Impact of dust on solar photovoltaic (PV) performance: Research status, challenges and recommendations,” *Renewable and sustainable energy reviews*, vol. 14, issue 9, pp. 3124-3131, 2010

[164] W.G. Nickling, A.J. Brazel, “Temporal and spatial characteristics of Arizona dust storms (1965-1980),” *Journal of Climatology*, vol. 4, issue 6, pp. 645-660, 1984

[165] S. Rothschild, C. Quiroz, M. Salhotra, A. Diem, “The Value of eGRID and eGRIDweb to GHG Inventories,” US Environmental Protection Agency, Washington, DC, USA, Dec. 2009

[166] R. Tidball, J. Bluestein, N. Rodriguez, S. Knoke, “Cost and Performance Assumptions for Modeling Electricity Generation Technologies,” National Renewable Energy Laboratory, US Department of Energy, CO, USA, Nov. 2010